

**HOT-WIRE CHEMICAL VAPOR  
DEPOSITION OF SILICON-NITRIDE THIN  
FILMS**

**Abdulghaaliq Adams**

A thesis submitted in fulfillment of the requirements for the degree of Magister  
Scientiae in the Faculty of Science, University of the Western Cape.



Supervisor: Prof. C Arendse, University of the Western Cape

Co-supervisor(s): Dr. T. Muller, University of the Western Cape

Dr. G. F. Malgas, CSIR

August 2013



*To My parents, Faiza and Nasief*

# ACKNOWLEDGEMENTS

---

To my Creator and Sustainer, all mighty Allah, for providing me with insight and understanding and without whom all this would not have been possible.

*I am grateful to the following people without whose assistance, advice and guidance the completion of this work would be greatly hindered:*

Prof. Christopher Arendse of the Department of Physics at the University of the Western Cape (UWC), for his supervision, friendship and guidance throughout this work;

Dr. Theo Muller of the Department of physics UWC who acted as co-supervisor and assisted with UV-vis;

Dr. Gerald Malgas of the CSIR who acted as co-supervisor;

Dr. Clive Oliphant, of NMISA for his valuable discussions, assistance and input into this work;

Dr. Mandla Msimanga, of the MRD at iThemba labs Gauteng for assistance with Heavy Ion ERD measurements and analysis;

Mr. Phillip Sechokela, of the MRD Cape Town for assistance with ERDA measurements;

Mr. Tim Lesch for assistance with FTIR measurements;

Dr. Remmy Bucher, of the MRD at iThemba labs for assistance with XRD measurements;

My mother Faiza and father Nasief Adams for the continued support and encouragement throughout my studies;

My loving wife Razia Adams for sticking by my side through all the late night study sessions spent at campus and at home;

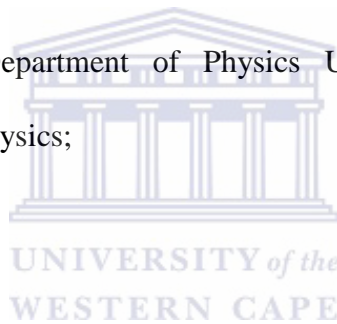
My brothers Gabeeburaghmaan and Rafeeq Adams for always supporting me;

My sister Rashieda Adam and mother Mariam Adam for all the support ;

My campus mother Angela Adams for always assisting me administratively and being there when we needed her;

My colleagues and fellow MANUS/MATSCI students at UWC, Nazley Towfie, Natasha Petersen, Razia Adam, Valentino van de Heyde and Sulaiman Jacobs for their friendship and support.

Prof. Delia Marshal, of the Department of Physics UWC for the help, support and encouragement during first year physics;

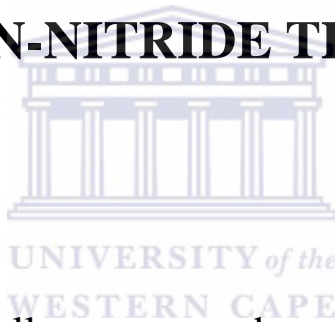


# DECLARATION

---

I declare that

**“HOT-WIRE CHEMICAL VAPOR DEPOSITION  
OF SILICON-NITRIDE THIN FILMS”**



Is my own work and that all sources used or quoted have been indicated  
and acknowledge by means of complete references.

  
Abdulghaaliq Adams

August 2013

# KEYWORDS

---

## HOT-WIRE CHEMICAL VAPOR DEPOSITION OF SILICON-NITRIDE THIN FILMS

**Abdulghaaliq Adams**



Hot-wire chemical vapour deposition (HWCVD)

Hydrogenated amorphous silicon nitride (a-SiN:H)

Total Flow rate

Hydrogen content

Nitrogen content

Band Gap

Growth process

Deposition rate

Process parameters

# ABSTRACT

---

**“Hot-wire chemical vapor deposition of silicon-nitride thin films”**

**Abdulghaaliq Adams**

**M. Sc thesis, Department of Physics, University of the Western Cape**

Amorphous silicon nitride (a-SiN:H) thin films has a multitude of applications, stemming from the tunability of the material properties. Plasma enhanced chemical vapour deposition (PECVD) is the industrial workhorse for production of device quality a-SiN:H. However, this technique has drawbacks in terms of film quality, rooting from ion bombardment, which then results in undesirable oxidation.

Hot wire chemical vapour deposition (HWCVD) has shown to be a viable competitor to its more costly counterpart, PECVD. A thin film produced by HWCVD lacks ion bombardment due to the deposition taking place in the absence of plasma. This study will focus on optimising the MV-systems® HWCVD chamber at The University of the Western Cape, for production of device quality a-SiN:H thin films at low processing parameters. The effect of these parameters on the structural, optical and morphological properties was investigated, for reduction of production costs. The films were probed by heavy ion elastic recoil detection, energy dispersive spectroscopy, Fourier transform infrared spectroscopy, atomic force microscopy, X-ray diffraction, and ultraviolet visible spectroscopy. It was shown that silicon rich, device quality a-SiN:H thin films could be produced by HWCVD at wire temperatures as low as 1400 °C and the films showed considerable resistance to oxidation in the bulk.

**August 2013**

# CONTENTS

---

Title Page .....	i
Acknowledgements .....	iii
Declaration .....	v
Keywords .....	vi
Abstract .....	vii

## Chapter 1 – Introduction

1.1 Historical Background .....	1
1.2 Significance and application in solar cell .....	3
1.3 Properties of a-SiN:H .....	7
1.3.1 Structural properties .....	7
1.3.2 Electronic Properties .....	10
1.3.3 Optical Properties .....	13
1.4 Preparation Techniques .....	16
1.5 Aims and Outline .....	20
1.6 References .....	22

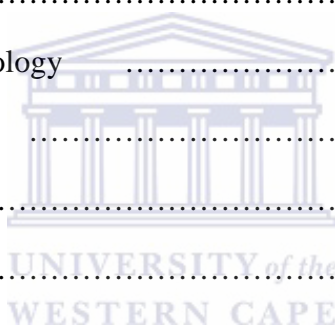
## Chapter 2 – Experimental Methods

2.1 The Hot-wire CVD System .....	27
2.2 Sample Preparation .....	29
2.3 Analytical Techniques .....	30
2.3.1 Introduction .....	30
2.3.2 Reflectance .....	30

2.3.3	Fourier Transform Infrared Spectroscopy	38
2.3.4	Energy Dispersive Spectroscopy	41
2.3.5	Atomic Force Microscopy	44
2.3.6	Elastic Recoil Detection Analysis	47
2.3.7	X-Ray Diffraction	53
2.4	References	60

### **Chapter 3: Results and Discussion**

3.1	Introduction	63
3.2	Experimental details	64
3.3	Deposition rate and Morphology	66
3.4	Compositional Properties	81
3.5	Structural Properties	106
3.6	Optical Properties	107
3.7	Conclusion	110
3.8	References	112
	<b>Summary</b>	<b>118</b>

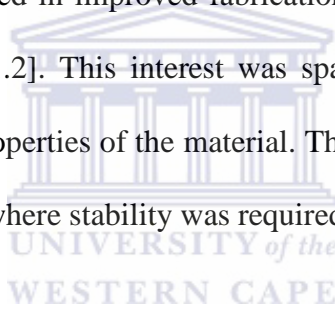


# CHAPTER 1

## INTRODUCTION

### 1.1. HISTORICAL BACKGROUND

Reports on silicon nitride date back prior to 1879, where Schrützenberger et al [1.1] reported the first silicon tetranitride ( $\text{Si}_3\text{N}_4$ ) formation. This compound was produced in a blast furnace by heating silicon with brusque (a carbon rich paste). At this stage silicon nitride was merely a chemical curiosity and did not take strongly to researchers up until the mid-twentieth century, where engineering advances resulted in improved fabrication techniques and thus led to a new found interest in silicon nitride [1.2]. This interest was sparked by the excellent mechanical, thermal and diffusive resistivity properties of the material. These properties made it attractive for application in gas turbine engines where stability was required at 1200 °C.



In 1958 silicon nitride was produced by heating silicon to around 1350 -1450 °C in a nitrogen (N) or ammonia ( $\text{NH}_3$ ) gas ambient, later termed reaction bonded silicon nitride (RBSN). This caused nitridation to occur within the silicon and resulted in crystalline silicon nitride formation with a trigonal symmetry ( $\alpha$ -silicon nitride) and hexagonal symmetry ( $\beta$ -silicon nitride) [1.3]. This method was used by Parr et al [1.4] to investigate silicon nitride as a stator blade material in a diesel gas turbine engine, as an electrical insulator and as refractory supports in industrial processes.

RBSN had drawbacks in terms of material porosity, which lead to limitations in mechanical strength. This drawback lead to the development of hot pressed silicon nitride (HPSN) during the

1960's [1.4 – 1.5], which involved hot pressing of silicon nitride powders, with sintering additives, into commercially used materials with an increased density. Despite an increased density, HPSN had a limitation in that it could only form simple shapes such as cutting tools.

Nihara *et al* presented among the earliest work on chemical vapour deposition CVD silicon nitride in 1976 [1.6]; where high growth rates and dense films were obtained. The films were prepared by reacting  $H_2$ ,  $NH_3$  and  $SiCl_4$  gas mixtures to investigate the effect of varying deposition temperatures and pressures. This work was in line with that developed for gas turbine engines and various other industrial applications of silicon nitride.

In CVD, precursor gases are fed into a chamber and decomposed by various means (heating, microwaves and plasma) in order to produce a film on a particular substrate. In the deposition of silicon nitride the film produced is highly dependent on the deposition parameters such as substrate temperature, chamber pressure and gas flow rate among others. CVD provided a cheaper alternative to sintering as a result of the high deposition rates attainable.

In the late 1970s amorphous silicon nitride (a-SiN:H) grasped the attention of material researchers for its application as an encapsulate against moisture penetration for silicon integrated circuits [1.7]. Amorphous silicon nitride has since found uses in thin film transistors [1.8] and as antireflective coatings in photovoltaic devices [1.9]. The high density and inert nature of silicon nitride films prepared by CVD resulted in it being ideal as a passivation layer in photovoltaic devices. Previously  $SiO_2$  and  $TiO_2$  were the preferred materials for passivation coatings. However, silicon nitride has a dual purpose in acting as an antireflective coating (due to

its high refractive index) as well as a defect pacifier [1.10]. This multipurpose material results in drastic cost reduction in manufacturing of photovoltaic devices, which is the underlying motivation for accelerated interest in a-SiN:H thin films. In recent years commercially manufactured silicon solar cells have been making use of silicon nitride layers for antireflective coatings and passivation of dangling bonds [1.11]. Apart from cost reduction the silicon nitride layer results in drastic increases in cell efficiency due to this multifunctional role.

## **1.2. SIGNIFICANCE AND APPLICATION IN SOLAR CELLS**

The dependence of the human race on “dirty” fossil fuels and nuclear power has come under scrutiny in recent years as a result of its environmental impact and dangers involving nuclear accidents, such as that observed in Fukushima in 2011. The increased demand for electrical power has placed an increased dependence on dirty energy. A report released by the U.S energy information agency in 2011 [1.12] projected that the demand will continue to rise as shown in figure 1.1, where a noticeable increase in coal and nuclear energy usage is observed.

The elevated dependence on fossil fuels has been the driving force behind scientific research in the direction of a viable renewable alternative. A promising alternative to the dirty fossil fuels came in the form of the solar cell, which is based on the photovoltaic effect discovered by Edmund Becquerel in 1839 [1.13]. The consistent decrease in price has added to the driving force behind research into photovoltaic devices [1.13]. The solar cell converts abundant solar energy, of wavelengths ranging from 200 - 3000 nm, into electrical energy.

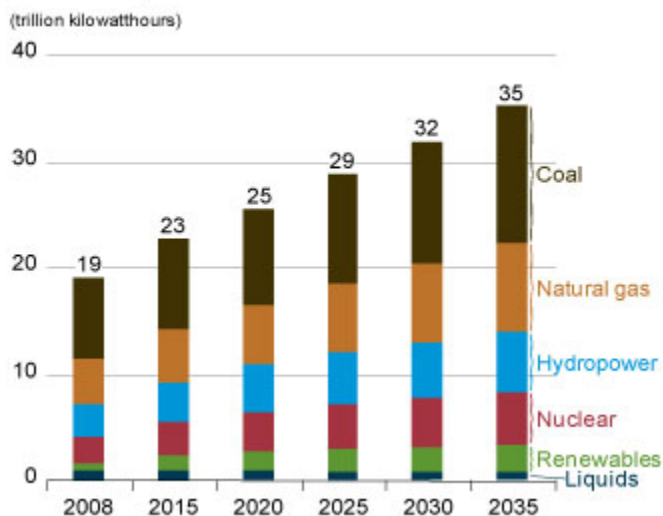


**Figure 1.1:** World energy consumption projection categorized by type [1.12].

In order to consider the effect of incorporation of a-SiN:H thin films in silicon solar cells it is important to consider the principle of operation of the solar cell. In the event of light of varying frequency being incident on a semiconductor, it results in the production of electron-hole pairs (excitons) only if the energy of the incident photon is greater than or equal to the band gap ( $E_g$ ) of the material. This indicates that a lower band gap will theoretically result in a better conversion efficiency of the electromagnetic (EM) spectrum as a broader range of frequencies may now be absorbed by the material. The creation of excitons is essentially the excitation of an electron from the valence band to the conduction band and, by this excitation, the electron leaves behind a positively charged hole. Crystalline silicon has a band gap of around 1.1 eV, which theoretically allows for 50% absorption efficiency. This value however is not practical as there are numerous means of energy loss; namely radiative recombination and Auger recombination, which limits the efficiency to 29% [1.14].

Typically a solar cell device consists of a p-type and n-type semiconductor layer stack, which result in the formation of a p-n junction as illustrated in figure 1.2. The function of creating a doped semiconductor such as a p-type or n-type is to introduce holes and electrons in the semiconductor device. This p-n junction allows for the sustained separation of electrons and holes by an induced electric field and result in the flow of current, with electrons and holes flowing in opposite directions. This flow of current is then transferred to a load by means of electrical contacts deposited on the device.

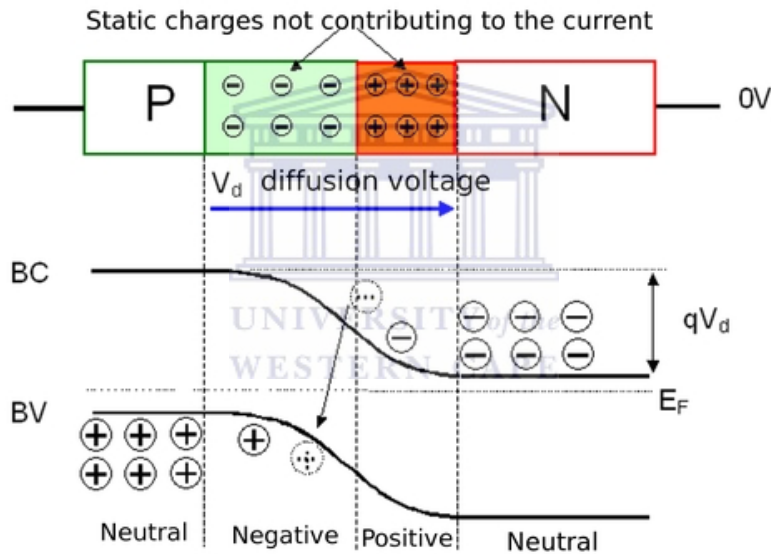


**Figure 1.2:** p-n junction structure in solar cell device [1.15].

A schematic of a crystalline silicon solar cell illustrating the incorporation of silicon nitride as anti-reflective surface coating (ARC) can be observed in figure 1.3.

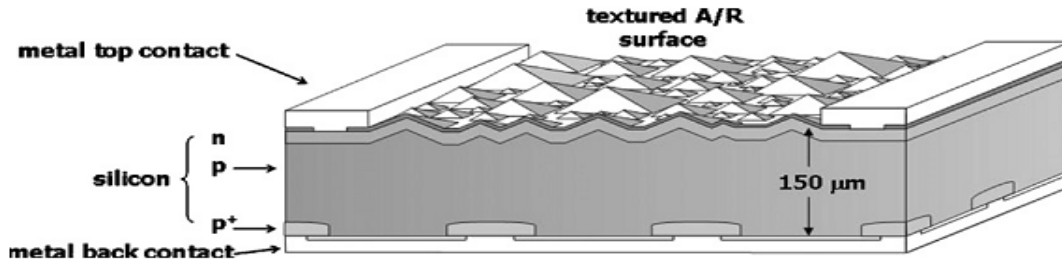


**Figure 1.3:** Solar cell schematic with Si-N as A/R surface [1.16].

The broad wavelength operating conditions of the solar cell makes it imperative to utilize a wide band gap material for anti-reflective coating (ARC) in order to maximise the photo current and minimise photon loss at the surface of the solar cell. The silicon wafer used in the solar cell typically reflects around 30% of incident photons and this has serious effects on the solar cell efficiency. The incorporation of the a-SiN:H thin films as antireflective layers with good surface passivation properties has been shown to reduce incident photon losses to below 3% in the region 300 – 1000 nm for plasma enhanced chemical vapour deposition (PECVD) a-SiN:H [1.17].

The a-SiN:H layers can be incorporated as single and double layers, where single layers allows for a broad transmission range and double layer incorporation allows for increases in the transmission even further due to the variation in refractive index between the two top layers. The incorporation of single layer a-SiN:H layers has been shown to reduce fractional reflectance to around 0.104, however double layer incorporation of a-SiN:H with SiO<sub>2</sub> has been shown to reduce the fractional reflectance further to around 0.044 [1.18]. Double layer a-SiN:H thin film incorporation as ARC has also been documented to elevate cell efficiency [1.19]. The optimum thickness ( $d$ ) of the a-SiN:H layer is dependent on the refractive index ( $n$ ) and wavelength ( $\lambda$ ) and can be determined according to equation 1.1 to be around 80 nm with a refractive index around 2 [1.20].

$$d = \frac{\lambda}{4n} \quad (1.1)$$

### 1.3. PROPERTIES OF AMORPHOUS SILICON NITRIDE

#### 1.3.1. STRUCTURAL PROPERTIES

The structural properties of a-SiN:H are highly dependent on the bonding arrangement and chemical stoichiometry within the amorphous matrix. This is not the case in crystalline silicon nitride (c-SiN), as the silicon (Si) and nitrogen (N) are optimally arranged in a tetrahedral manner as illustrated in figure 1.4 where the bond lengths are also illustrated. Nitrogen is incorporated in a chemically ordered fashion in the production of crystalline SiN (c-SiN).

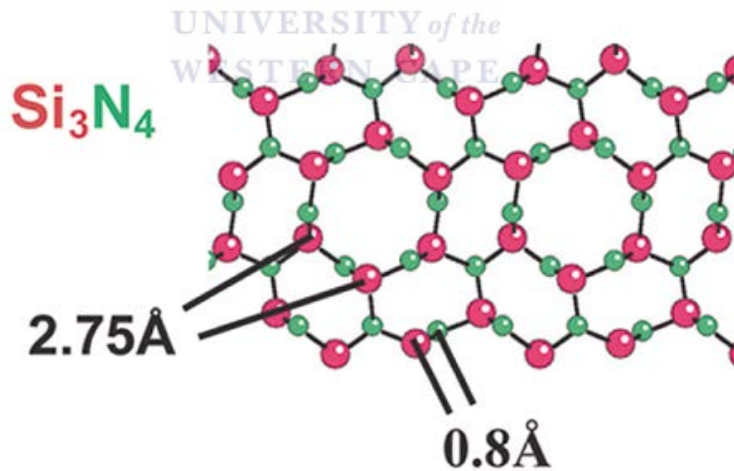


**Figure 1.4:** Crystal structure of SiN [1.21].

In the consideration of the chemical structure of a-SiN:H, the arrangements of the atoms can vary considerably. The multivalent nature of the covalent, N and Si bonds results in highly complex

arrangements within the amorphous matrix and various models have been employed to describe these arrangements [1.22– 1.23]. Stoichiometric a-SiN:H is tetrahedrally arranged, whereas non-stoichiometric a-SiN:H can be found in various configurations, depending on the N incorporation, as shown by Hasegawa *et al* [1.24]. The structure of a-SiN:H is illustrated in figure 1.5. If the Si/N ratio is above 0.6, the bonding geometry is similar to that of beta phase planar atoms in crystalline silicon nitride [1.25]. The manner in which N is incorporated into the a-SiN:H matrix is highly dependent on the amount of N present, as the N atom is surrounded by 3 Si atoms in silicon rich films and the presence of Si decreases as the N incorporation increases [1.26].

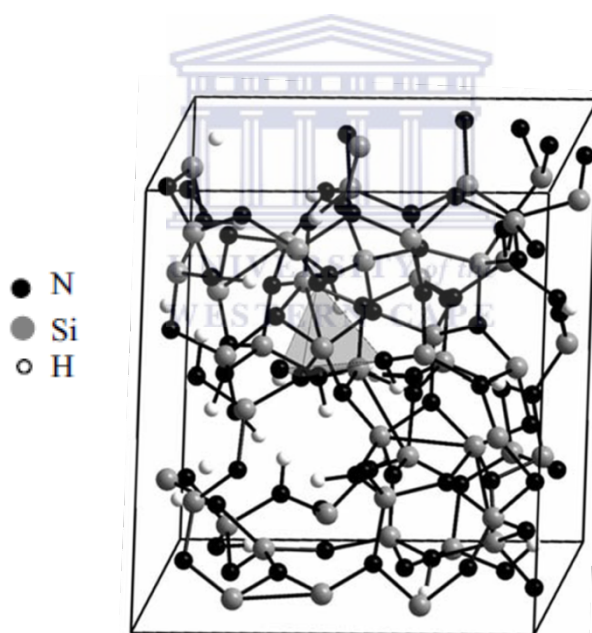


**Figure 1.5:** Structure of a-SiN:H [1.27].

There are various bonds present in a-SiN:H; namely Si-N, Si-H, Si-Si and N-H bonding units, where N-N bonds are not thermodynamically favoured and are thus not prominent. These bonds are arranged in various configurations depending on the composition of the film and have a certain dependence on the bond angle within the matrix. The bond length in an a-SiN:H matrix is

highly depended on the bonding unit present, which is again dependent on the nitrogen incorporation. Nitrogen has a greater electronegativity than Si, which results in bond angle deviations in the a-SiN:H matrix when excess N is present [1.28].

The bond angle within a-SiN:H thin films plays a pivotal role in the measuring the stress characteristics of the film and is an important consideration for applications in solar cell technologies. In a-SiN:H thin films the bond angle deviation increases with increased nitrogen incorporation. The nitrogen has been shown to cause deviations in bond angle ranging from 6.6 – 16.1°, which provides an indication of changes in local order within the film [1.29]. The coordination of the atoms are responsible for stress as the presence of 3 and 4 – fold coordinated atoms cause coordination mismatching and results in strain, which then introduces stress [1.29 – 1.30]. The stress also goes from compressive to tensile depending on the N and H incorporation in the film [1.31]. The degree of roughness is also affected by the stress of the film.

Understanding the surface roughness of thin films is important in order to gain insight into the growth mechanism and the ability to grow uniform layer stacks. The roughness also provides great insight into the interfacial trap density as a rougher surface tends to have an elevated interfacial trap density [1.32]. The surface roughness of a-SiN:H thin films tend to be low and are dependent on the deposition parameters and growth mechanism [1.33]. A rougher surface is associated with an increased amount of disorder and thus increased stress. Hydrogen incorporation into the amorphous matrix results in relaxation of stress due to the low coordination of hydrogen [1.26]. The hydrogen diffusion also results in passivation of dangling bonds in silicon solar cells, also reducing voids and stress [1.34].

The mass density of a-SiN:H thin films tend to be highly dependent on the deposition parameter and N incorporation in the films. The mass density of a-SiN:H thin films has been shown to have an inverse relation to the level of H present in the film [1.35], which shows that high H incorporation results in the production of voids and makes the film susceptible to oxidation. Mass density is highly dependent on the nitrogen incorporation and can range from 1.8 g/cm<sup>3</sup>, for low nitrogen content, to 3.1 g/cm<sup>3</sup> for stoichiometric films; it then decreases significantly for higher nitrogen incorporation. The high mass density and inert nature of the film makes this material ideally suited as a diffusion barrier for impurities such as oxygen [1.30, 1.33]. The hardness of these films makes it ideal for scratch resistant coatings also, for nearly stoichiometric films it has been shown to have a tensile strength as high as 15 GPa [1.28].

The properties of a-SiN:H have been shown to be thermally stable up to 400 °C [1.30] and the films remain amorphous at temperatures as high as 1100 °C [1.36]. The above mentioned composition dependence of the structural properties is also extended to optical and electronic properties of the a-SiN:H thin film, as will be discussed in the next sections.

### **1.3.2. ELECTRONIC PROPERTIES**

In order to better understand the optical properties of a-SiN:H such as the band gap it is imperative to consider the electronic properties of the material. In perfectly crystalline semiconductors the band gap is well defined and there is a complete absence of states in the band gap as shown in figure 1.6. At absolute zero all occupied states are below the Fermi level in the Valence Band (VB), which indicates that electrical conduction is impossible since there are no

conduction electrons. The band gap tends to become more complex for amorphous semiconductors.

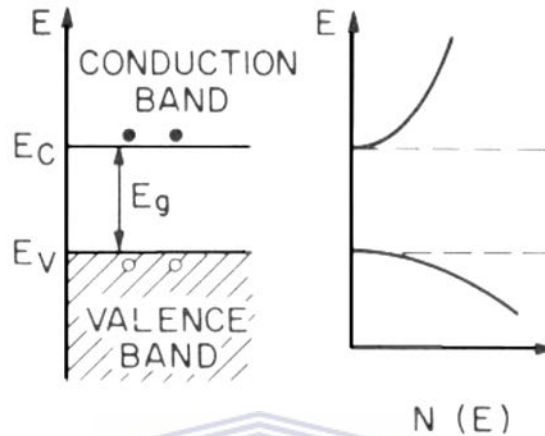


**Figure 1.6:** Perfectly crystalline semiconductor band gap [1.37].

To better understand the band gap of a-SiN:H it is important to consider the origin and role of dangling bonds and defect centres in the a-SiN:H matrix. The presence of dangling bonds arise as a result of distortions and coordination mismatching in the a-SiN:H network, which are as a result of the N preferential bonding to three Si atoms [1.38]. During the deposition of a-SiN:H thin films by CVD, Si and N dangling bonds are present in the resulting films and are dependent on the level of N present in the deposited film [1.39]. The Si and N dangling bonds result in tailing of the density of states (DOS) into the band gap, which results in a suppression of the band gap ( $E_g$ ) by the trap states. A DOS state below the top of the valence band is observed to originate from the N dangling bonds around -1.8 eV and a DOS in the centre of the band is seen to originate from Si dangling bonds according to Lin et al [1.40]. A similar result is obtained by Robertson [1.41]. However a DOS is shown to be in the region 4.2 eV stemming from Si

dangling bonds for stoichiometric a-SiN:H thin films and is illustrated in figure 1.7, which results in a band gap of 4.2 eV.

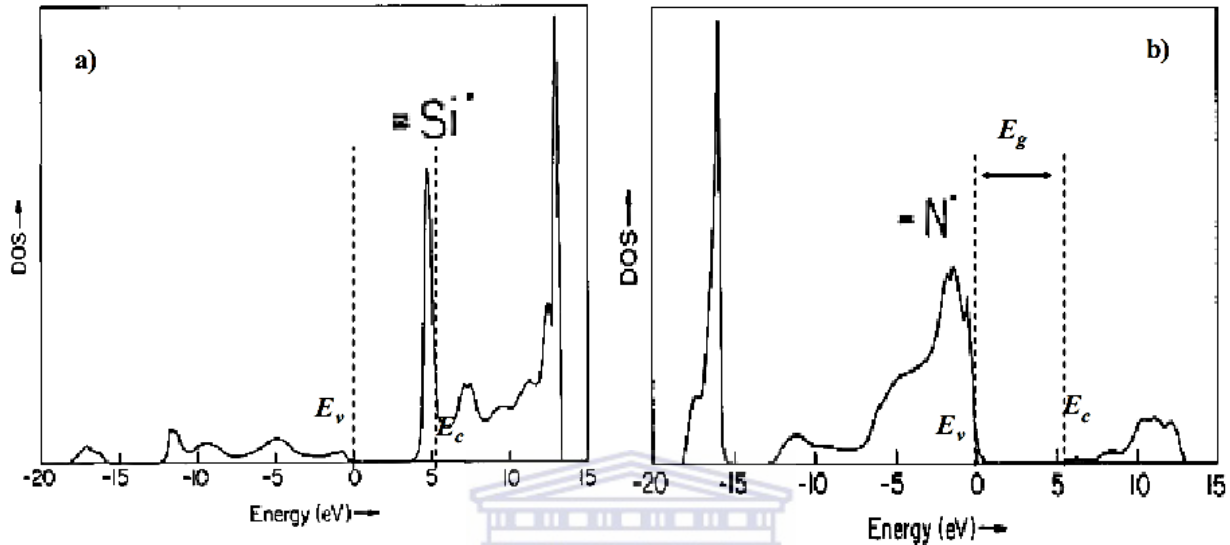


**Figure 1.7:** Illustration of the density of states resulting from a) Si dangling bonds and b) N dangling bonds [1.41].

The introduction of H into the matrix has also been shown to reduce the tailing of the DOS into the band gap due to the monovalent nature of the H atom, which passivates the uncoordinated atoms as shown by Karazanov et al [1.42] in figure 1.8. The figure shows that non-stoichiometric hydrogenated silicon nitride has a similar density of states to that of stoichiometric unhydrogenated amorphous silicon nitride (a-SiN) (the dashed line). The figure also shows the crystalline band structure to be less complex and more defined than the a-SiN:H band structure. The figure clearly shows the deviation from the fundamental band gap of 5.4 eV for stoichiometric a-SiN as a result of the dangling bonds tailing into the band gap.

The dependence of the electronic properties on the N incorporation provides fundamental insight as to the practical applicability of a-SiN:H thin films in photovoltaic devices.

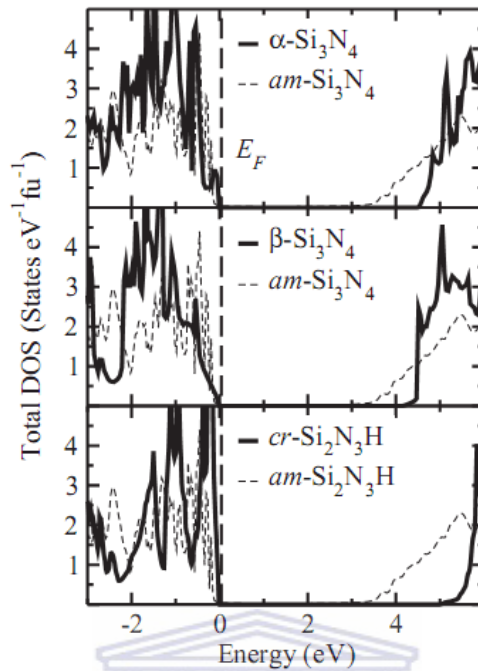
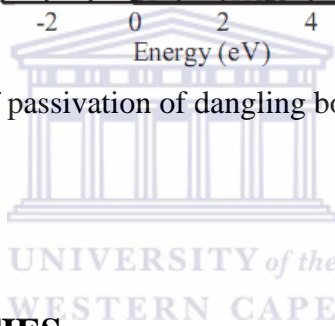


**Figure 1.8:** Illustration of effect of passivation of dangling bonds by incorporation of H into the matrix. [1.42]



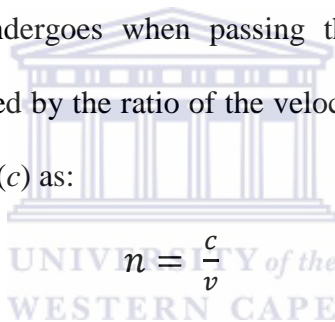
### 1.3.3. OPTICAL PROPERTIES

The prospects of a-SiN:H thin films for the application in photovoltaic devices warrants investigation into the optical behaviour of the material. The optical properties, such as the band gap and refractive index, are key factors in the industrial applicability of the material; as the band gap distinguishes the amount of photons that passes through the material without being absorbed and a coating with a refractive index that differs from the active layer allows for reduction in the optical reflectivity. Commercially 90% of ARC consist of a-SiN:H as top layer due to the tunability of the band gap and refractive index based on the material properties [1.43]. The

optical properties may be obtained from Ultraviolet visible (UV-vis) spectroscopy in either transmission or reflection geometry.

Three fundamental processes are used to describe a material optically; namely electronic transitions, lattice vibrations and free carrier effects. The dominance of a particular process within an optical material is dependent on the spectral region of measurement and the material under study [1.45].

The refractive index is one of the properties under study in this work as it is a measure of the distortions the speed of light undergoes when passing through a particular medium. The refractive index ( $n$ ) can be described by the ratio of the velocity of light through the medium ( $v$ ) and the speed of light in a vacuum ( $c$ ) as:



$$n = \frac{c}{v} \quad (1.2)$$

The N content dependence of the properties of a-SiN:H thin films extends to the optical properties also. The refractive index of the a-SiN:H can be tuned by varying the deposition parameters and N/Si ratio. The refractive index of a-SiN:H thin films have an inverse proportionality to the N/Si ratio as shown by Verlaan *et al* in figure 1.9 [1.46]. The refractive index can be varied from around 3 for silicon rich a-SiN:H thin films to ~1.7 for nitrogen rich thin films.

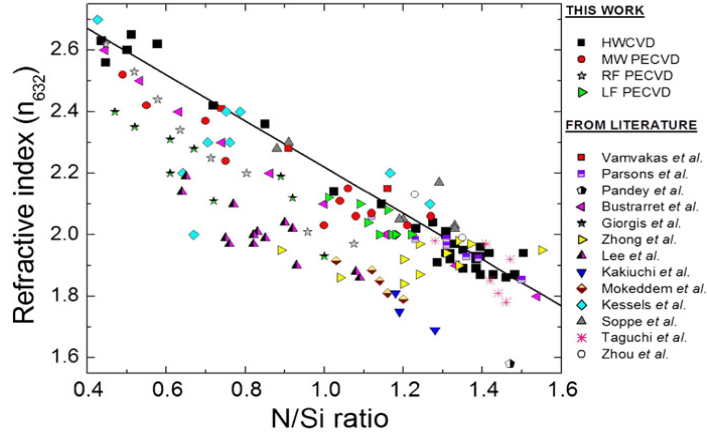


**Figure 1.9:** Refractive index as a function of N content [1.46].

The compositional dependence of the refractive index can be understood using the *Lorenz-Lorenz* equation which relates the polarizability ( $\alpha$ ) of a medium to its refractive index as:

$$\frac{n^2-1}{n^2+2} = \frac{4\pi}{3} \sum_k M_k \alpha_k \quad (1.3)$$

This equation indicates that films containing similar N content will have a depressed refractive index that is attributed to a variation in mass density; where M is the atomic density of atom  $k$  [1.46].

The band gap ( $E_g$ ) of a-SiN:H thin films is an important parameter to consider for application, as an ARC with maximum transparency being required. The band gap of a-SiN:H thin films can vary considerable depending on the stoichiometric concentration of the thin film, where low N content films are observed to have low band gaps approaching the band gap of a-Si and high N content films have elevated band gaps. The  $E_g$  values of a-SiN:H thin films have been seen to vary from around 2.7 eV for silicon rich films to around 5 eV for stoichiometric films [1.47]. The

variation of the band gap can be attributed to varying levels of defect states introduced into the band gap by Si and N dangling bonds as shown in figure 1.10. It can be seen from figure 1.10 that the band gap saturates at a stoichiometric N/Si ratio of 1.33. The effect of the N dangling bond defect state can be seen to be more prevalent at elevated N content where the band gap is wider. The films used in the construction of figure 1.10 were a-SiN thin films without H in the matrix. The defect states introduced by the dangling N and Si bonds can be reduced by the introduction of H into the matrix, however this comes at the expense of density of the films.

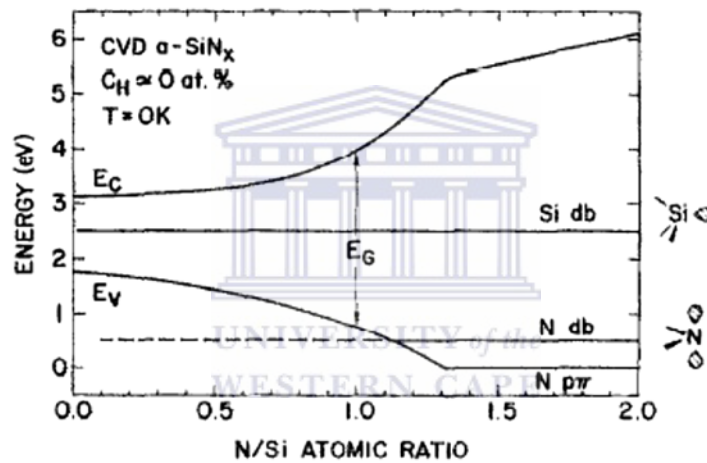


**Figure 1.10:** Band diagram with varying N content [1.48], where E<sub>g</sub>, E<sub>c</sub> and E<sub>v</sub> is the band gap, conduction band and valence band, respectively.

## 1.4. PREPARATION TECHNIQUES

The versatility of silicon nitride has been a catalyst for investigating a-SiN:H thin films by a multitude of techniques including; thermal CVD [1.49], photo assisted CVD [1.50], electron cyclotron resonance [1.51], hot wire CVD [1.52] and plasma enhanced CVD [1.53]. Production

of a-SiN:H thin films by these techniques usually involve SiH<sub>4</sub> and NH<sub>3</sub> as precursor species. The current industrial workhorse for production of a-SiN:H thin films is PECVD, due to the reproducibility and low temperature deposition [1.53]. However, HWCVD has gained increased interest due to ease of upscale for large area deposition and superior film quality being attainable. The PECVD and HWCVD techniques will now be considered in more detail.

The deposition of thin films by PECVD is possible when an electrical voltage is supplied to a gas in a low pressure ambient, typically in the region of 13.3 – 13332.24 μbar. The process results in the production of a plasma consisting of electrons and ions. The electrons in the plasma result in the activation of source gas molecules into film forming radicals [1.54]. A schematic of the activation process can be viewed in figure 1.11.

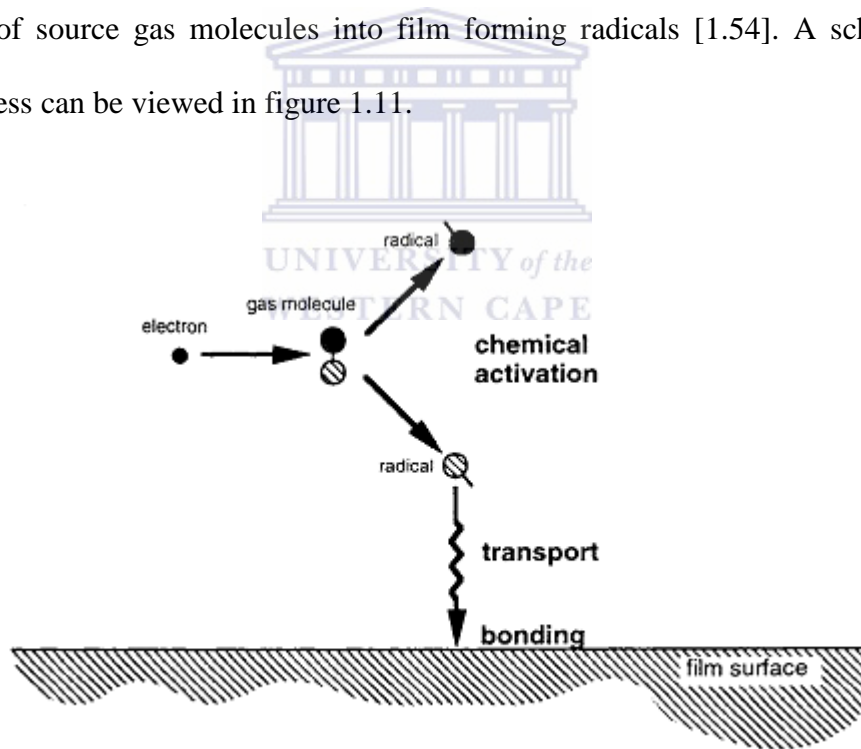


**Figure 1.11:** Schematic of activation process in PECVD [1.54].

The process described in figure 1.11 takes place in the presence of a potential difference, where the substrate is part of the grounded electrode. The potential difference results in acceleration of the plasma produced ions into the film, which causes degradation in film quality due to ion

bombardment of the film and substrate and results in films with high H content and defects. The plasma process has a low gas decomposition efficiency which results in low deposition rates.

HWCVD provides a means of eliminating the shortcomings of PECVD due to the mechanism of deposition eradicating the production of film bombarding ions and superior deposition rates being attainable due to elevated decomposition efficiencies [1.55 – 1.56]. The first patent for HWCVD was granted to Weismann *et al* [1.57] in 1979 where tungsten and graphfoil was resistively heated to about 1600 °C while SiH<sub>4</sub> was directed at the heated foil. A substrate was placed in the vicinity of the foil where the reacted species were collected to form a-Si thin films in order to study the photoconductivity of the deposited thin films. The technique was dubbed Catalytic-CVD (Cat-CVD) in 1986 by Matsumura *et al* [1.58] due the fact that the heated filament plays the role of a catalyser in the decomposition of the source gasses, Cat-CVD and HWCVD are used interchangeably. A HWCVD reactor can be viewed in figure 1.12, where the simplicity of the HWCVD method can be seen. The method leads to ease of up scaling, since a larger filament area and gas supply system is the only requirement. Since the substrate does not form part of the deposition process, it can easily be moved and handled.

During deposition by HWCVD the source gasses are decomposed over the heated tungsten filament and results in the production of film forming radicals in a process similar to that shown in figure 1.11. However, the radicals are not produced by ionized electrons in HWCVD. Since there are no ions produced in HWCVD, the ion damage is eliminated, which implies dense, low H content films produced by HWCVD.

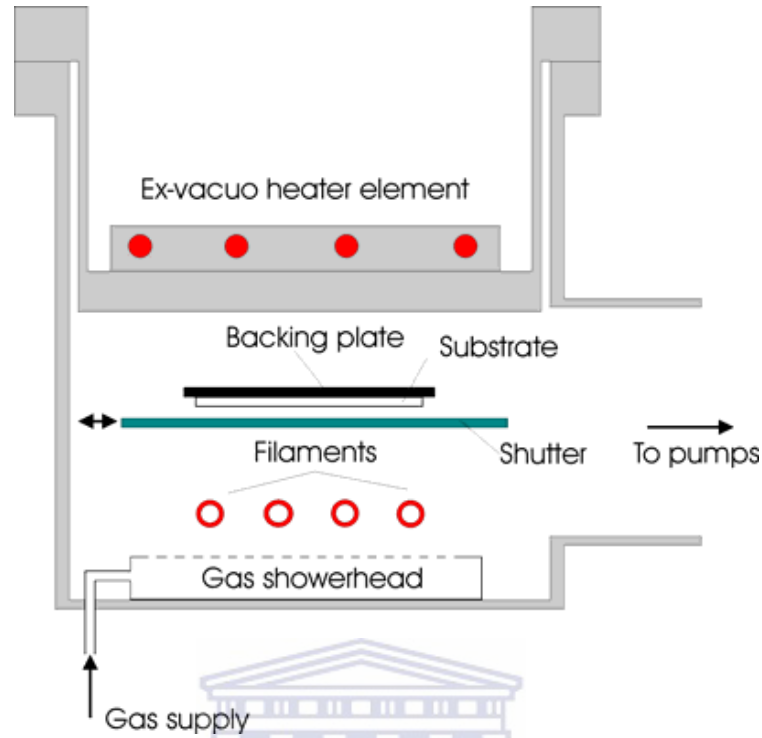


**Figure 1.12:** HWCVD reactor illustrating all the components [1.59].

Matsumura *et al* [1.59] deposited among the earliest a-SiN:H thin films by HWCVD in 1989, where  $N_2H_4$ ,  $N_2$  and  $SiH_4$  were used as source gasses at a wire temperature of  $\sim 1300$  °C and substrate temperature of around 300 °C. It was shown in this work that device quality a-SiN:H thin films with good step coverage can be produced by HWCVD [1.59].

Another promising factor that HWCVD brings to the deposition of a-SiN:H is the decomposition efficiency. This parameter is prevalent since the main purpose of the a-SiN:H thin films production is to increase sustainability. The gas decomposition efficiency in HWCVD is shown to be superior to PECVD with the addition of  $H_2$  to the  $NH_3$  and  $SiH_4$  gas mixture [1.60]. In the absence of  $H_2$ , the decomposition efficiency of  $NH_3$  has been shown to decrease considerably as a result of poisoning of the filament [1.61].

The technique of HWCVD is highly versatile and has since been shown to be useful in the deposition of nano-structured materials such as nano-crystalline diamond films for dental applications [1.62] and silicon nanowires for implementation in electronic and photovoltaic materials [1.63].

### 1.5. AIMS AND OUTLINE

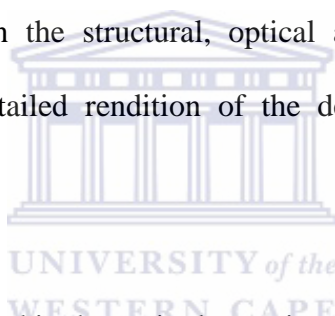
Presently PECVD is used industrially as a means for deposition of a-SiN:H thin films for device applications. However, the HWCVD technique has gained increased interest from researchers worldwide, as a result of high deposition rates, ease of upscale and low cost deposition of device quality a-SiN:H thin films. The deposition parameters play a pivotal role in the quality and versatility of the a-SiN:H thin films produced by HWCVD. This makes it desirable to understand and optimise the a-SiN:H deposition process. The MV-systems® HWCVD chamber at the University of the Western Cape will be optimised for deposition of a-SiN:H thin films under low processing parameters, in order to investigate the possibility of low cost deposition of device quality a-SiN:H thin films. This will be achieved by depositing a series of a-SiN:H thin films under varying deposition parameters such as pressure, NH<sub>3</sub>, H<sub>2</sub> and total flow rate. The effect of these parameters will be investigated on the structural, optical and morphological properties of the a-SiN:H thin films. This will also provide insight into the deposition mechanism of a-SiN:H thin films by HWCVD.

Chapter 1 will discuss some historical aspects, structural, electronic and optical properties of a-SiN:H thin films prepared in literature. The deposition technique of choice, HWCVD will also be

discussed and the advantages will be highlighted as compared to the currently used industrial technique, PECVD.

The experimental techniques such as UV-vis, FTIR, XRD, HIERD, ERDA, EDS and AFM will be discussed in some detail in chapter 2. The method of measurement, calibration and the deposition conditions will be divulged in chapter 2. The practicality of the technique of choice will also be illustrated.

The results and discussion will be shown in chapter 3, where the effect of the pressure,  $\text{NH}_3$ ,  $\text{H}_2$ , total flow rate and N/Si ratio on the structural, optical and morphological properties will be discussed and investigated. A detailed rendition of the deposition mechanism will also be discussed.



A summary of all the results obtained is shown in the section following chapter 3.

## 1.6. REFERENCES

- [1.1] P. Schützenberger, *Compt. Rend.* **2**, p 644 (1879)
- [1.2] C. Wang, X. Pan, M. Rühle, F. L. Riley and M. Mitomo, *J. Mat. Sci.*, **31**, p 5281 (1996)
- [1.3] S. N. Ruddlesden and P. Popper, *Acta Cryst.*, **11**, p 465 (1957)
- [1.4] N. L. Parr, G. F. Martin and R. May, “study and application of silicon nitride as a high temperature material”, *A.M.L Report No. A/75(s)* (1959)
- [1.5] S. Hampshire, *J. Achievements in materials science and engineering* **24**, p 43 (2007)
- [1.6] K. Niihara and T. Hirai, *J. Mat Sci.* **11**, p 593 (1976)
- [1.7] W. A. Lanford and M. J. Rand, *J. Appl. Phys.*, **49**, p 2473 (1978)
- [1.8] B. Stannowski, J. K. Rath and R. E. I. Schropp, *Thin Solid Films*, **430**, p 220 (2003)
- [1.9] F. L. Riley, *Journal of America Ceramic Society*, **83**, p 245 (2000)
- [1.10] S. Jung, D. Gong and J. Yi, *Solar Energy Materials & Solar Cells*, **95**, p 546 (2011)
- [1.11] V. Verlaan, C. H. M. van der Werf, Z. S. Houweling, Y. Mai, R. Bakker, I. G. Romijn, A. W. Weeber, H. D. Goldbach and R. E. I. Schropp, *Rapidly deposited hot-wire cvd silicon nitride as passivating antireflection coating on solar cells* Unpublished.
- [1.12] [Online] “*International energy outlook 2011*”, report DOE/EIA-0484 (2011) accessed 31/05/13
- [1.13] A. Shah, P. Torres, R. Tscharnner, N. Wyrsh, and H. Keppner, *Science* **285**, p 692 (1999)

- [1.14] J. Werner, R. Bergmann, and R. Brendel, *Festkor A*, **34**, p 115 (1995)
- [1.15] N. Servagent, Ecole des Mines de Nantes, [Online], [http://www.optique-ingenieur.org/en/courses/OPI\\_ang\\_M05\\_C02/co/Contenu\\_05.html](http://www.optique-ingenieur.org/en/courses/OPI_ang_M05_C02/co/Contenu_05.html) accessed 2013-07-29
- [1.16] D. M. Bagnall and M. Boreland, *Energy Policy*, **36**, p 4390 (2008)
- [1.17] S. Duttgupta, F. Ma, B. Hoex, T. Mueller and A. G. Aberle, *Energy Procedia*, **15**, p 78 (2012)
- [1.18] D.N. Wright, E.S. Marstein and A. Holt, *Proceedings of the 22nd European Photovoltaic Solar Energy Conference, Milano, Italy*, p 1651-1655 (2007)
- [1.19] B. Liua, S. Qiub, N. Chena, G. Dua and J. Sunc, *Materials Science in Semiconductor Processing*, **16**, p 1014, (2013)
- [1.20] A. El amrania, I. Menousa, L. Mahioua, R. Tadjineb, A. Touatia, A. Lefgouma, *Renewable Energy*, **33**, p 2289 (2008)
- [1.21] A. Ziegler, C. Kisielowski, R.O. Ritchie, *Acta Materialia*, **50**, p 565 (2002)
- [1.22] H.R. Phillip *Journal of non-crystalline solids* **8**, p 627 (1972)
- [1.23] R.T. Sanderson *Chemical bonds and bond energy*, 2<sup>nd</sup> Edition Academic press New York p77 (1976)
- [1.24] S. Hasegawa, L. He, Y. Amano and T. Inokuma, *Phys. Rev. B*, **48**, p 5315 (1993)
- [1.25] E. Bustarret, M. Bensouda, M. C. Habrard, J. Bruyere, S. Poulin, and S. Gujrathi *Phys. Rev. B* **38**, p 8171 (1998)
- [1.26] S. Hasegawa, M. Matsuda and Y. Karuta, *Appl. Phys. Lett.*, p 2211 (1990)

- [1.27] S. Zh. Karazhanov, P. Kroll, A. Holt, A. Bentzen, and A. Ulyashin, *J. Appl. Phys.*, **106**, 053717 (2009)
- [1.28] Q. Wang, S. Ward, L. Gedvilas, B. Keyes, E. Sanchez and S. Wang, *Applied Physics Letters*, **84**, p 338 (2004)
- [1.29] B. P. Swain, B. S. Swain and N. M. Hwang *Applied Surface Science*, **255**, p 2557 (2008)
- [1.30] F. Giorgis, C. F. Pirri and E. Tresso, *Thin Solid Films*, **307**, p 296 (1997)
- [1.31] S. Hasegawa, T. Inokuma *Thin Solid Films*, **187**, p 278 (1995)
- [1.32] L. Lai, E.A. Irene, *J. Appl. Phys.*, **86**, p 1729 (1999)
- [1.33] W. Xu, B. Li, T. Fojimoto, I. Kojima, *Surface and coatings Technology* **135**, p 274 (2001)
- [1.34] A. Kshirsagar, P. Nyaupane, D. Bodas, S. P. Duttagupta and S. A. Gangal *Applied Surface Science*, **257**, p 5052 (2011)
- [1.35] R.E.I. Schropp, S. Nishizaki , Z.S. Houweling , V. Verlaan , C.H.M. van der Werf , H. Matsumura, *Solid-State Electronics*, **52**, p 427 (2008)
- [1.36] M. Diserens, J. Patscheider and F. Levy, *Surf. Coat. Technol.*, **108–109**, p 241 (1998)
- [1.37] S.M. Sze, in *Semiconductor Devices*, John Wiley & Sons, New York (1985)
- [1.38] P. Kroll, *Mat. Res. Soc. Symp. Proc.*, **715**, p 1011 (2002)
- [1.39] C.T. Kirk, *J. Appl. Phys.*, **50**, p 4190 (1979)
- [1.40] Shu-Ya Lin, *Journal optoelectronics and advanced materials*, **4**, p 543 (2002)

- [1.41] J. Robertson, *J. Appl. Phys.*, **54**, p 4490 (1993)
- [1.42] S. Zh. Karazhanov, P. Kroll, A. Holt, A. Bentzen, and A. Ulyashin, *J. Appl. Phys.*, **106**, 053717 (2009)
- [1.43] F. Duerinckx and J. Szlufcik, *Sol. Energy Material Sol. Cells*, **72**, p 231 (2002)
- [1.44] K.-C. Lin and S.-C. Lee, *J. Appl. Phys.*, **72**, p 5474 (1992)
- [1.45] Chapter 2 - Refractive Index, In: Edward D. Palik, Editor(s), *Handbook of Optical Constants of Solids*, Academic Press, Burlington, 1997, Pages 5-114, ISBN 9780125444156, 10.1016/B978-012544415
- [1.46] V. Verlaan, A.D. Verkerk, W.M. Arnoldbik, C.H.M. van der Werf, R. Bakker, Z.S. Houweling, I.G. Romijn, D.M. Borsa, A.W. Weeber, S.L. Luxembourg, M. Zeman, H.F.W. Dekkers, R.E.I. Schropp, *Thin Solid Films*, **517**, p 3499 (2009)
- [1.47] W. C. Tan, S. Kobayashi, T. Aoki, R. E. Johanson and S. O. Kasap, *J. Mater Sci*, **20**, p S15 (2009)
- [1.48] W.L. Warren, J. Kanicki, P.M. Lenahan, *Appl. Phys. Lett.*, **59**, p 1699 (1991)
- [1.49] R. S. Bailey and V. J. Kapoor, *Vac. Sic. Technol.*, **20**, p 484 (1982)
- [1.50] B. D. Beach and J. M. Jasinski, *J. Phys. Chem.*, **94**, p 3019 (1990)
- [1.51] L. Wang, H. S. Reehal, F. L. Martinez, E. San Andrés and A. del Prado, *Semicon. Sci. Technol.*, **18**, p 633 (2003)
- [1.52] Y. Uchiyama, A. Masuda and H. Matsumura, *Thin Solid Films*, **395**, p 275 (2001)
- [1.53] W. Soppe, H. Rieffe, and A. Weeber, *Prog. Photovolt: Res. Appl.*, **13**, p 551 (2005)
- [1.54] Frank Jansen, Chapter 5.5 - Plasma-Enhanced Chemical Vapor Deposition, In: Dorothy M. Hoffman, Bawa Singh, John H. Thomas III and John H. Thomas III, Editor(s),

- Handbook of Vacuum Science and Technology, Academic Press, San Diego, 1998, Pages 711-730, ISBN 9780123520654, 10.1016/B978-012352065-4/50075-4
- [1.55] R.E.I. Schropp, C.H.M. van der Werf, V. Verlaan, J.K. Rath, H. Li, *Thin Solid Films*, **517**, p 3039 (2009)
- [1.56] F. Liu, S. Ward, L. Gedvilas, B. Keyes and B. To et al, *J. Appl. Phys.*, **96**, p 2973 (2004)
- [1.57] H. Wiesmann, A. K. Gosh, T. McMahon and M. Strongin, *J. Appl. Phys.*, **50**, 3752 (1979)
- [1.58] H. Matsumura, *Jpn. J. Appl. Phys.* **25**, p L949 (1986)
- [1.59] R.E.I. Schropp, *ECS Transactions*, **25**, p 3 (2009)
- [1.60] S.G. Ansari, H. Umemoto, T. Morimoto, K. Yoneyama, A. Izumi, A. Masuda and H. Matsumura, *Thin solid films*, **501**, p 31 (2006)
- [1.61] H. Umemoto, T. Morimoto, M. Yamawaki, Y. Masuda, A. Masuda and H. Matsumura, *Thin Solid Films*, **430**, p 24 (2003)
- [1.62] E. Hamzah and T.M. Yong, M.A. Mat Yajid, *Journal of Crystal Growth*, **372**, p 109 (2013)
- [1.63] Nagsen Meshram, Alka Kumbhar and R.O. Dusane, *Materials Research Bulletin*, **48**, p 2254, (2013)

## CHAPTER 2

### EXPERIMENTAL METHODS

#### 2.1 THE HOT-WIRE CVD SYSTEM

A single chamber ultra-high vacuum hot wire chemical vapour deposition (HWCVD) system manufactured by MV-Systems was used for the deposition of the a-SiN:H thin films in this study. The system is capable of achieving vacuum in the order of  $10^{-9}$  mbar. A comprehensive description of the system can be found in work done by Arendse *et al* [2.1]. The reaction chamber is constructed from welded 304-stainless steel, with CF flanges and copper gaskets to connect the pumps, heater well, gate valve, gas supply and exhaust, view ports and instrumentation. The system has a 1250 W substrate heater, mounted in a well on the top flange of the chamber. A panel-mounted controller with a type K thermocouple attached to the bottom of the heater well controls the temperature of the substrate heater. A stainless steel backing plate, placed against the back of the substrate holder, is used to ensure a homogeneous substrate temperature.

The principle of operation of the system is based on catalytically decomposing precursor gases over the Tungsten filament. The Tungsten filament breaks down the inlet gases and produces film forming precursors. These precursors then adhere to the substrate surface and result in the growth of the required film by HWCVD, also known as Cat-CVD. There are various parameters that can be controlled during the deposition in order to tune the material properties to the required application. These parameters include, but are not limited to, chamber pressure, gas

## EXPERIMENTAL METHODS

flow rate, substrate heater temperature, wire temperature and distance to the filament. These parameters will have varied effects on the outcomes of the thin films deposited and it is of utmost importance to optimize them for deposition of the required thin films. A schematic of the deposition process can be viewed in figure 2.1, adapted from Arendse *et al* [2.2].

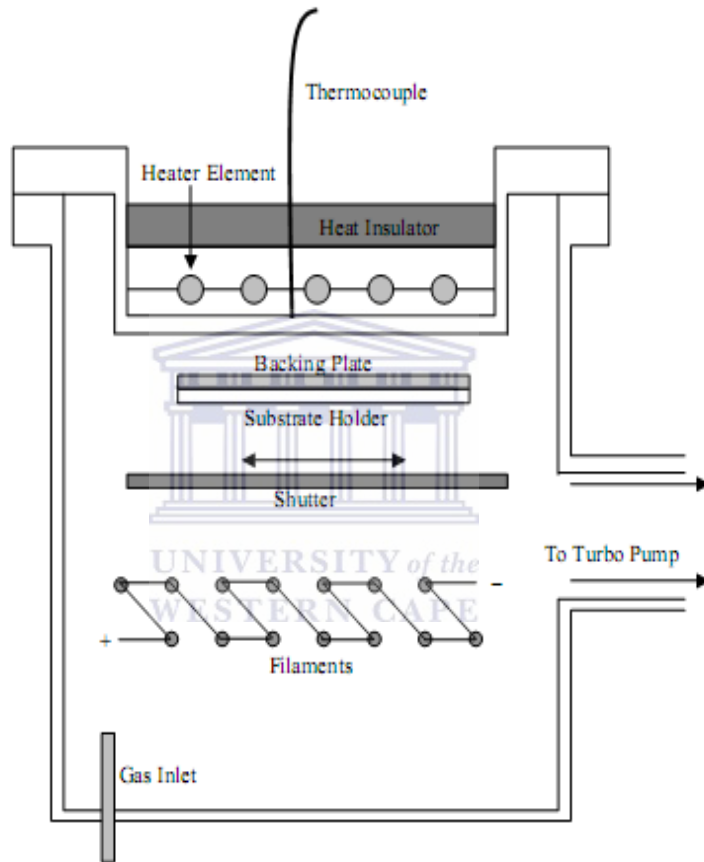


**Figure 2.1:** Schematic of HWCVD chamber used [2.2].

## **2.2 SAMPLE PREPARATION**

The samples prepared were deposited on corning 7059 glass and <100> crystalline silicon substrates cut in 2.5 cm × 2.5 cm squares. The substrates were ultrasonically cleaned in acetone for 5 min followed by a sonication in ethanol for an additional 5 min. The silicon substrates were dipped in a 1% HF solution for 1 min in order to eradicate the native oxide layer.

Films were only deposited once a background pressure of  $10^{-7}$  mbar was attained in the deposition chamber. The wire configuration consisted of 7 parallel Ta wires connected to an AC power supply. The filament was treated with H<sub>2</sub>, to etch the contaminated Ta wire surface for a period of around 3 min. the distance between the substrates and the Ta filament was 18 mm.

Once the samples were loaded the chamber was pumped down and the substrates were covered with a shutter. The precursor gases were allowed into the chamber and the chamber was allowed to equilibrate before the shutter was opened and the deposition could start. The duration of each deposition was 30 min. A total of four sample series were deposited namely; pressure variation, NH<sub>3</sub> gas flow rate variation, H<sub>2</sub> flow rate variation and total flow rate variation. The details of the deposition parameters will be shown in detail in chapter 3.2.

## **2.3 ANALYTICAL TECHNIQUES**

### **2.3.1 INTRODUCTION**

The effective characterization of a-SiN:H requires an array of sensitive techniques to investigate the behavioural characteristics of the deposited films. The table below displays the techniques used in this study and the information attained from the analysis.

**Table 2.1:** Analysis techniques used.

<b>Technique</b>	<b>Information</b>
Reflectance	<ul style="list-style-type: none"> <li>• Thickness</li> <li>• Band Gap</li> <li>• Refractive index</li> </ul>
FTIR	<ul style="list-style-type: none"> <li>• SiN bonds</li> <li>• Total bonded H</li> </ul>
EDS	<ul style="list-style-type: none"> <li>• N/Si ratio</li> </ul>
AFM	<ul style="list-style-type: none"> <li>• Surface morphology</li> <li>• Roughness</li> </ul>
ERDA	<ul style="list-style-type: none"> <li>• H depth profiling</li> </ul>
TOF-HIERD	<ul style="list-style-type: none"> <li>• N depth profiling</li> <li>• N/Si ratio</li> </ul>
XRD	<ul style="list-style-type: none"> <li>• Phase</li> </ul>

### **2.3.2 REFLECTANCE**

The efficient deposition of a-SiN:H by HWCVD is of utmost importance in the production of cost effective thin film solar cells. The use of the a-SiN:H thin film as anti-reflective coating (ARC) warrants investigation into the reflection of the deposited a-SiN:H thin films. Reflection measurements are essential in the event that films are deposited on thick absorbing substrates like <100> silicon, as in this study. This application makes it important to understand certain

optical properties of the material such as the refractive index and band gap. These values are strongly dependent on the material properties and deposition parameters and hence the investigation into the effect of N incorporation on the band gap and refractive index.

## **THEORY**

The optical reflection spectra of a thin film illuminated at normal angle of incidence by monochromatic radiation can be described by standard optics. In the presence of a film with thickness  $d_f$  throughout, it can be characterized by the complex refractive index:

$$N_1 = n_1 - ik_1 \quad (2.1)$$

And the substrate can be described by (with substrate thickness  $\gg d_f$ ):

$$N_2 = n_2 - ik_2 \quad (2.2)$$

Where  $n_1, n_2$  is the real parts of the refractive index and  $k_1, k_2$  is the imaginary part, also known as the extinction coefficient. The reflectance, according to Müllerová *et al* [2.3], can be described as follows:

$$R(\lambda) = \frac{A + Bx + Cx^2}{D + Ex + Fx^2} \quad (2.3)$$

Where absorbance is given by  $x = \exp(-ad_f)$ , and absorption coefficient is given by

$$a = (4\pi n_1 d_f) / \lambda,$$

$$A = [(1 - n_1)^2 + k_1^2][(n_1 + n_2)^2 + (k_1 + k_2)^2]$$

$$B = 2[A' \cos \phi + B' \sin \phi]$$

$$C = [(1 + n_1)^2 + k_1^2][(n_1 - n_2)^2 + (k_1 - k_2)^2]$$

$$\begin{aligned}
 D &= [(1 + n_1)^2 + k_1^2][(n_1 + n_2)^2 + (k_1 + k_2)^2] \\
 E &= 2[C' \cos \phi + D' \sin \phi] \\
 F &= [(1 - n_1)^2 + k_1^2][(n_1 - n_2)^2 + (k_1 - k_2)^2] \\
 A' &= (1 - n_1^2 - k_1^2)(n_1^2 - n_2^2 + k_1^2 - k_2^2) + 4k_1(n_1k_2 - n_2k_1) \\
 B' &= 2(1 - n_1^2 - k_1^2)(n_1k_2 - n_2k_1) - 2k_1(n_1^2 - n_2^2 + k_1^2 - k_2^2) \\
 C' &= (1 - n_1^2 - k_1^2)(n_1^2 - n_2^2 + k_1^2 - k_2^2) - 4k_1(n_1k_2 - n_2k_1) \\
 D' &= 2(1 - n_1^2 - k_1^2)(n_1k_2 - n_2k_1) + 2k_1(n_1^2 - n_2^2 + k_1^2 - k_2^2) \quad (2.4)
 \end{aligned}$$

A fitting procedure is required to determine the refractive index from the equation below:

$$R(\lambda_i, n_1, k_1, d) - R_{exp} = 0 \quad (2.5)$$

Where  $R(\lambda_i, n_1, k_1, d)$  is the calculated spectrum and  $R_{exp}$  is the experimental reflectance spectra.

When consideration is given to the optical band gap determination it is important to consider the photo conductivity and density of states and the role they play in the optical behaviour of the amorphous material at hand. The thin film photoconductivity is given by R. Zallen [2.5]:

$$\sigma(\omega) = \frac{2\pi e^2 \hbar^3 \Omega}{m^2 \hbar \omega} \int \{f(E) - f(E + \hbar\omega)\} N(E) |P(\omega)|^2 N(E + \hbar\omega) dE \quad (2.6)$$

$N(E)$  and  $N(E + \hbar\omega)$  are the conduction and valence band density of states respectively, in the event of interband transitions.  $\Omega$  is the size of the volume element containing one electron while  $f(E)$  is the Fermi-Dirac distribution.  $P(\omega)$  is the constant momentum matrix element for absorption. This equation reduces for the approximation when  $T = 0$  for the Fermi-Dirac distribution, which is a good approximation for the interband transitions.

$$\sigma(\omega) = \frac{2\pi e^2 \hbar^3 \Omega}{m^2 \hbar \omega} \int N(E) |P(\omega)|^2 N(E + \hbar\omega) dE \quad (2.7)$$

The absorption coefficient as a function of photoconductivity is given by:

$$\alpha(\omega) = \frac{\sigma(\omega)}{\varepsilon_0 n(\omega) c} \quad (2.8)$$

This allows for the expression of equation 2.8 in terms of the absorption coefficient as below:

$$\sigma(\omega) = \frac{2\pi e^2 \hbar^3 \Omega}{m^2 \hbar \omega \varepsilon_0 n(\omega) c} \int N(E) |P(\omega)|^2 N(E + \hbar\omega) dE \quad (2.9)$$

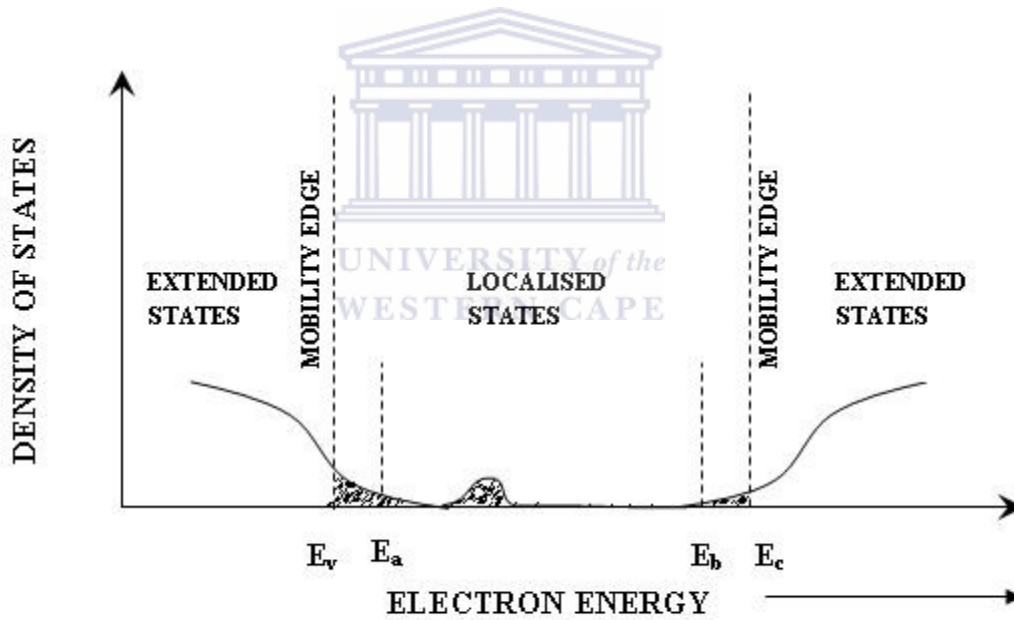


**Figure 2.2:** Density of states of an amorphous material [2.5].

The density of states can be determined by:

$$N(E) = N_v \left( \frac{E_a - E}{E_a - E_v} \right)^P \quad \text{for } E \leq E_a \quad (2.10)$$

$$N(E) = N_v \left( \frac{E_a - E}{E_a - E_v} \right)^P \quad \text{for } E \geq E_b \quad (2.11)$$

$E_a$  and  $E_b$  can be observed in figure 2.2. Substitution of the density of states into equation 2.9 and integrating over all possible transitions produces the following equation, where  $\Gamma$  is the gamma function and the angular brackets are an average over E:

$$\sigma(\omega) = \frac{2\pi e^2 \hbar^3 \Omega}{m^2 \hbar \omega \epsilon_0 n(\omega) c} \frac{\Gamma(p+1)\Gamma(q+1)}{\Gamma(p+q+2)} \times \frac{N_v N_c}{(E_a - E_v)^p (E_c - E_b)^q} \langle |P(\omega)|^2 \rangle (\hbar\omega - E_g)^{1+p+q} \quad (2.12)$$

For the assumption that  $P(\omega)$  is independent of  $\omega$  then equation 2.13 arises:

$$[\alpha(\omega)n(\omega)\hbar\omega]^{\frac{1}{1+p+q}} = B_g (\hbar\omega - E_g) \quad (2.13)$$

Where  $B_g$  and  $E_g$  is a constant and optical band gap respectively. If the DOS is assumed to be parabolic in the conduction and valance band then the Tauc band gap is attained [2.7], which was used as the band gap in this study:

$$[\alpha(\omega)n(\omega)\hbar\omega]^{\frac{1}{2}} = (\hbar\omega - E_{g(Tauc)}) \quad (2.14)$$

## EXPERIMENTAL SET-UP

The optical measurements were performed with a Semiconsoft inc [2.6], MProbe Thin-film measurement system with a resolution of 1 nm and in the range from 200 nm – 1000 nm. The set-up is displayed in figure 2.3.

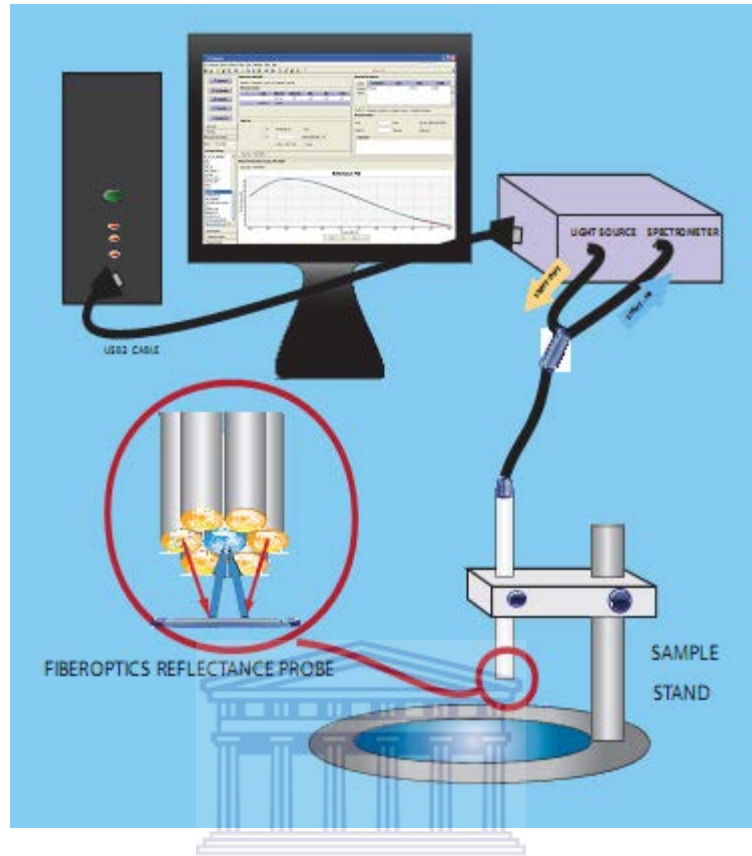


**Figure 2.3:** Schematic of set-up [2.4].

The optical reflectance spectra were modelled using Scout® software, which implemented a model for a theoretical amorphous semiconductor, developed by O’Leary *et al* (OJL) [2.8]. A typical modelled reflectance spectrum of the HWCVD a-SiN:H thin film is displayed in figure 2.4. The red line is the experimental spectrum and the blue is the calculated spectrum using the OJL model.

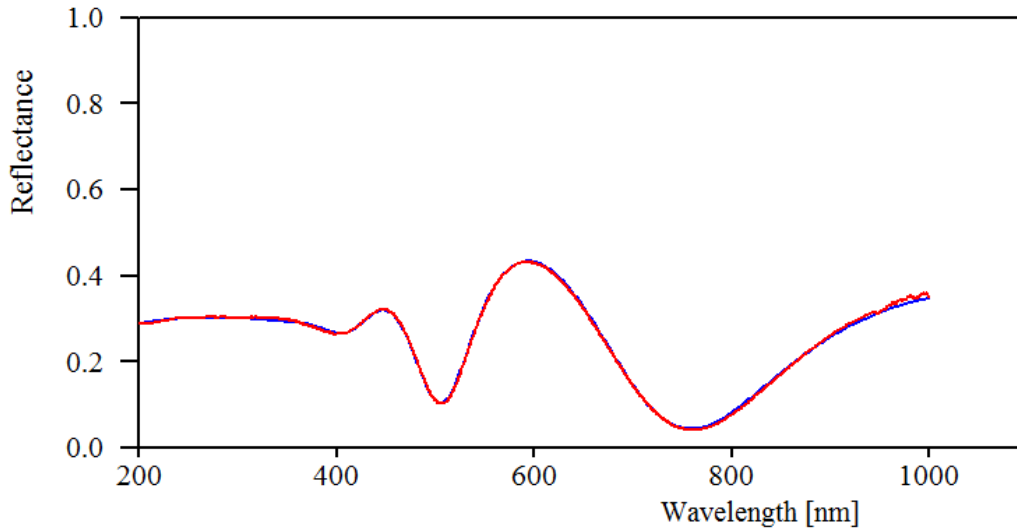


**Figure 2.4:** Typical reflectance spectrum after applying the OJL fit.

Once the fitting process was completed the data was extracted and the static refractive index and Tauc band gap was determined from the dispersion plots displayed below. Figure 2.5 illustrates a plot of  $1/n^2-1$  vs.  $h\nu^2$  where  $n$  is the static refractive index and is determined from the fit indicated on figure 2.5. The plot in figure 2.6 illustrates the Tauc plot and the fit shown in this plot is used for determination of the optical band gap.

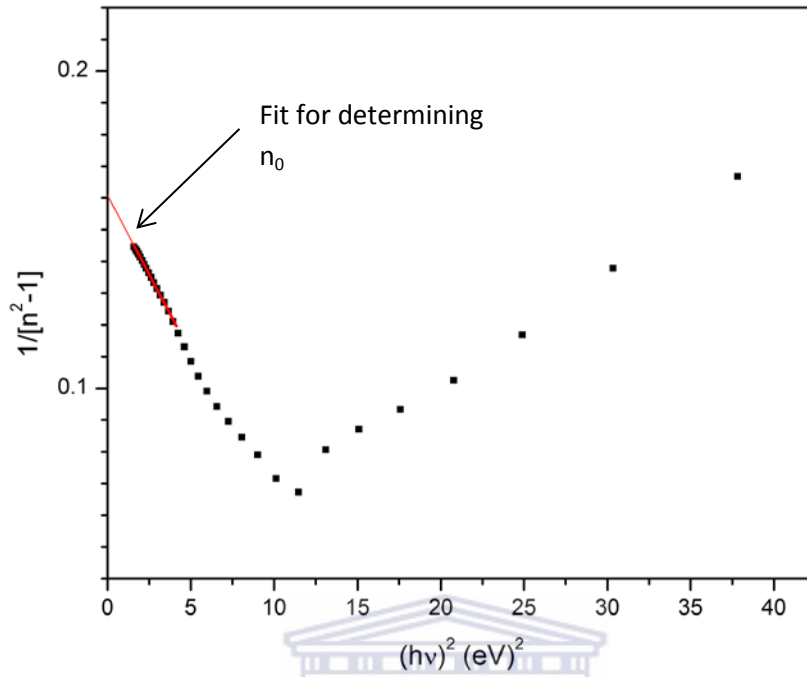


Figure 2.5: Plot for determining static refractive index.

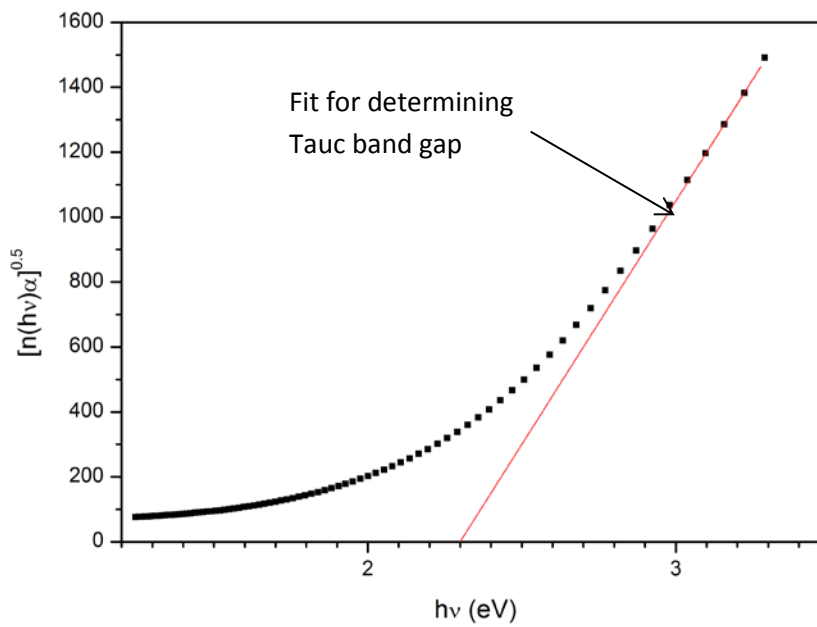


Figure 2.6: Tauc plot for band gap determination.

### 2.3.3 FOURIER TRANSFORM INFRARED SPECTROSCOPY

Fourier Transform Infrared FTIR spectroscopy is a commonly used technique for bond quantification in a-SiN:H. This comes as a result of the ease and non-destructive nature of measurements that can be performed by FTIR. The spectra also allows for the determination of the bond orientation in the a-SiN:H thin film matrix. The a-SiN:H thin films were deposited on c-Si substrates for FTIR measurements as a result of the transparency of c-Si to IR radiation. The FTIR spectra were fitted and corrected using an IDL program called “*FIT Version 4.05.2*” by C.T.A.M. de Laat.

#### THEORY

FTIR was performed using a Perkin Elmer Spectrum 100 spectrophotometer from 400 – 4000  $\text{cm}^{-1}$  with a resolution of 4  $\text{cm}^{-1}$  and the spectrometer was set to transmission mode. Prior to each measurement a background measurement was obtained from a clean c-Si substrate in order to account for the substrate. In the event of infrared radiation being incident on a molecule with a dipole moment, the molecule will vibrate at a frequency unique to that bonding orientation. If a dipole moment is not present the molecule will not vibrate and it will not be detected by FTIR, hence the inability of FTIR to detect molecular hydrogen present in a-SiN:H thin films.

The absorption coefficient  $\alpha(\omega)$  as a function of transmission  $T(\omega)$  spectrum is given by:

$$\alpha(\omega) = -\frac{\ln[T(\omega)]}{d} \quad (2.15)$$

The a-SiN:H thin film thickness is given by  $d$ .

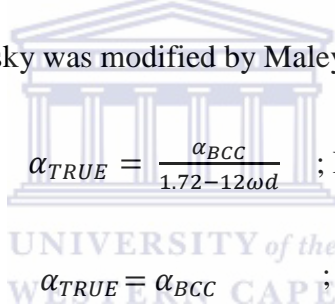
Reflections which occur within the c-Si substrate (incoherent reflections) have to be corrected for as they result in interference fringes in the FTIR spectrum. A correction procedure for incoherent reflections was introduced by Brodsky *et al* [2.9]. This method is based on the assumption that the a-SiN:H thin film and the substrate has equal refractive indices. The corrected absorption coefficient  $\alpha_{BCC}$  and measured transmission spectrum can be related by:

$$T(\omega) = \frac{4T_0 e^{-\alpha_{BCC}d}}{[(1+T_0)^2 - (1-T_0)^2 e^{-\alpha_{BCC}d}]} \quad (2.16)$$

Where  $T_0$  is the baseline transmission when  $\alpha(\omega) = 0$  and  $T_0 = 0$  for c-Si.

A procedure to account the effects of coherent reflections was introduced by Maley *et al* [2.10].

The procedure introduced by Brodsky was modified by Maley as follows:



$$\alpha_{TRUE} = \frac{\alpha_{BCC}}{1.72 - 12\omega d} \quad ; \text{ For } \omega d \leq 0.06$$

$$\alpha_{TRUE} = \alpha_{BCC} \quad ; \text{ For } \omega d \geq 0.06 \quad (2.17)$$

A typical a-SiN:H transmission spectrum before correction is shown in figure 2.7 and the corresponding spectrum after correction for incoherent and coherent reflection is displayed in figure 2.8.

**Table 2.2:** Peak assignments

Region (cm-1)	Assignment
~ 640	SiH wagging
~ 840	SiN stretching
~ 1100	Si-O-Si stretching
~ 1200	NH bending
~ 2100	SiH stretching
~3340	NH stretching

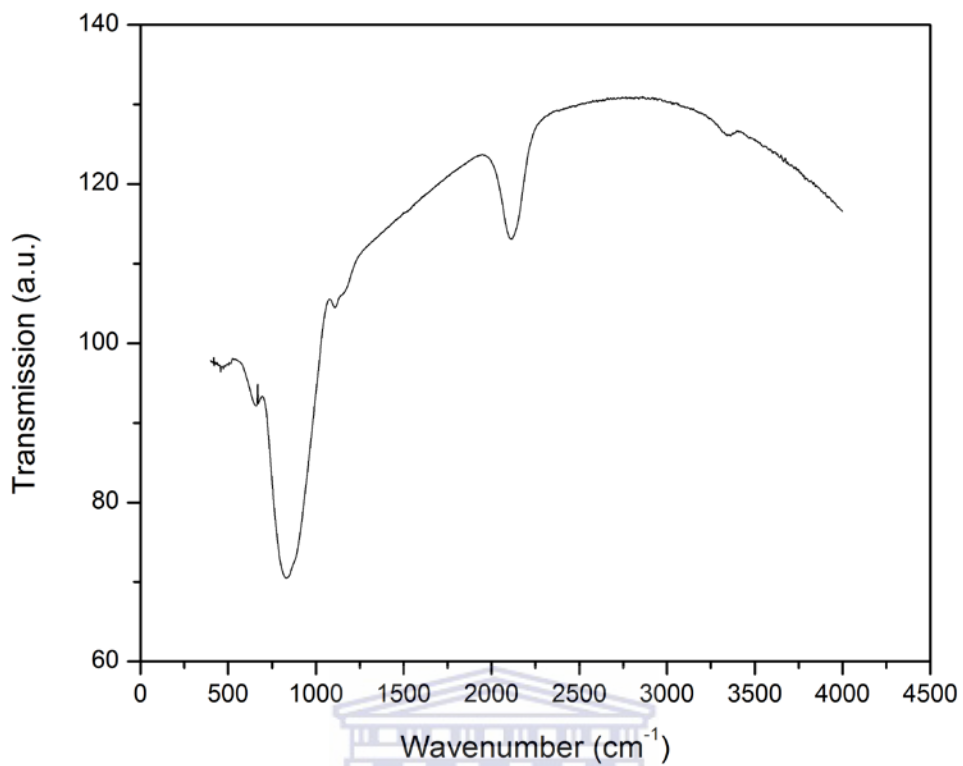


Figure 2.7: Raw FTIR spectrum after measurement from spectrometer.

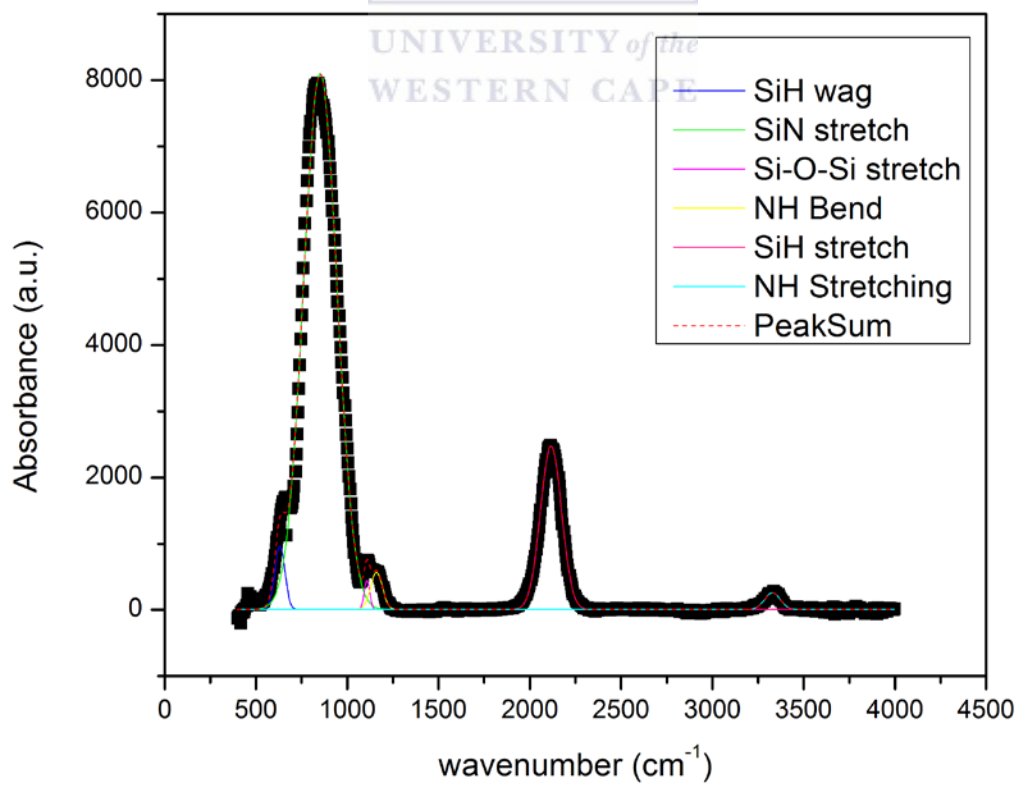


Figure 2.8: Corrected and fitted FTIR spectrum.

On completion of the correction, the FTIR spectra are deconvoluted by means of Gaussian fits and the integrated absorption is determined for bond quantification. The integrated absorption  $I_\omega$  is given by:

$$I_\omega = \int_{-\infty}^{+\infty} \frac{\alpha(\omega)}{\omega} d\omega \quad (2.18)$$

The integrated absorption allows for bond quantification by means of the proportionality factors from the following equation:

$$[X] = AI_\omega \quad (2.19)$$

Where  $[X]$  is the bond concentration and  $A$  is the proportionality factor associated to that specific bonding arrangement. There is considerable controversy surrounding the proportionality constants as they depend highly on the composition of the film and thus all bond quantities in this study will be displayed as the integrated absorption.

### **2.3.4 ENERGY DISPERSIVE SPECTROSCOPY**

Microcharacterization analysis has been revolutionized by the developments made in Energy Dispersive Spectroscopy (EDS). Since the measurements performed for this study were done using a Scanning Electron Microscope (SEM), only the EDS detector orientation in the SEM will be illustrated and discussed.

The interaction of the electron beam in the SEM with the specimen results in the emission of electrons from the sample in various ways and with differing energy. These electrons include Auger, backscattered and secondary electrons, which can be viewed in figure 2.9.

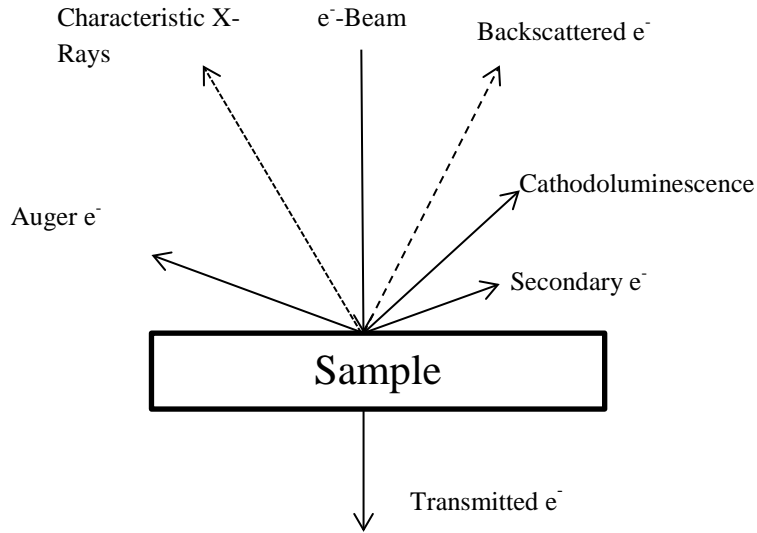


**Figure 2.9:** Electron beam interaction with specimen.

When an electron is ejected from an atom, the atom is left in an excited state, which is undesirable and to restore equilibrium an electron from the outer shells will fill the hole left by the ejected electron. Since the process results in de-excitation of the atom, energy is given off in the form of electromagnetic radiation. If this process occurs in the innermost electrons of the atom then an X-ray, characteristic of the specimen will be emitted. A schematic of the process is described in figure 2.10.

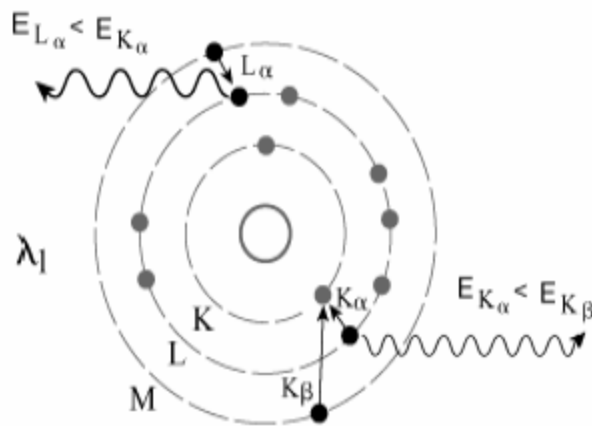


**Figure 2.10:** Atomic de-excitation resulting emission of characteristic X-rays [2.11].

The inner most electron orbitals are labelled K, L and M as shown in the diagram, in the event of a de-excitation from the L level to the K level then a  $K_{\alpha}$  characteristic X-ray is emitted and if the de-excitation takes place from the M level to the K level then the characteristic X-Ray is deemed  $K_{\beta}$ .

The X-rays described above are detected by means of a semiconducting material such as silicon and germanium. The semiconducting material is oriented in such a manner as to maximize the emitted X-ray interaction. It is possible to place the detector 20 mm from the sample in SEM in order to maximize detector-X-ray interactions. The orientation of the detector in the SEM can be viewed in figure 2.11. The incoming X-rays result in the excitation of the semiconducting detector in the form of electron-hole pairs. The energy of the incoming beam is proportional to the number of electron-hole pairs created in the semiconductor. The electron-hole pairs are perceived as short pulses by the detector and these pulses are then amplified and passed through the Multi-Channel Analyser (MCA) for sorting, which produces a histogram. The Histogram is then converted, through computer processing, to the spectra shown in figure 2.12 for a-SiN:H.

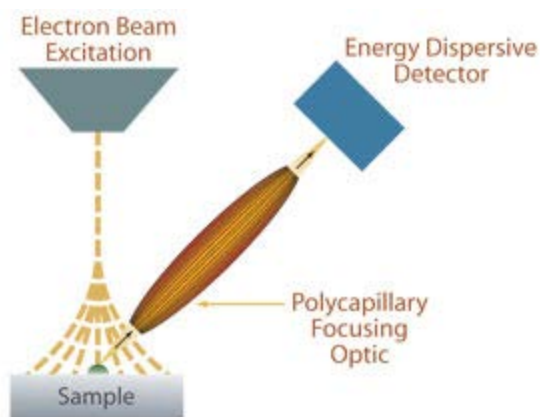


**Figure 2.11:** Detector set-up for SEM [2.12].

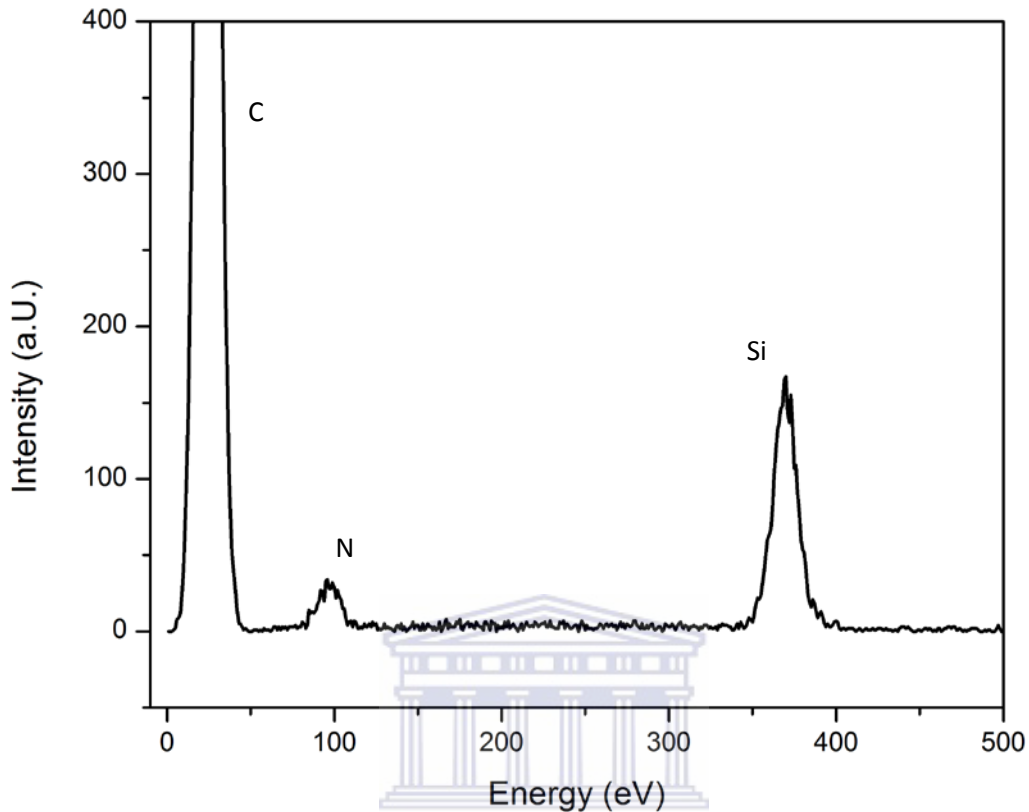


**Figure 2.12:** Illustration of EDS spectra for sample containing elevated levels of N.

### 2.3.5 ATOMIC FORCE MICROSCOPY

The a-SiN:H thin films deposited on c-Si substrates were studied by Atomic Force Microscopy (AFM) in order to gain insight into the surface morphology of the thin films prepared for this study. The investigation of the a-SiN:H thin films by AFM is warranted by the continued downscaling of semiconductor devices. In the investigation of thin films the surface morphology becomes important as rough surface results in elevated interfacial trap density and makes subsequent depositions non-uniform [2.13 – 2.15].

AFM images are a measure of the interaction forces between the tip and the sample surface. This allows for atomic resolution images to be attainable. The images are attained by "feeling" rather than looking at the sample under study. There are three regimes for tip surface interactions namely; contact, intermittent contact and non-contact. These regimes can be viewed in figure 2.13.

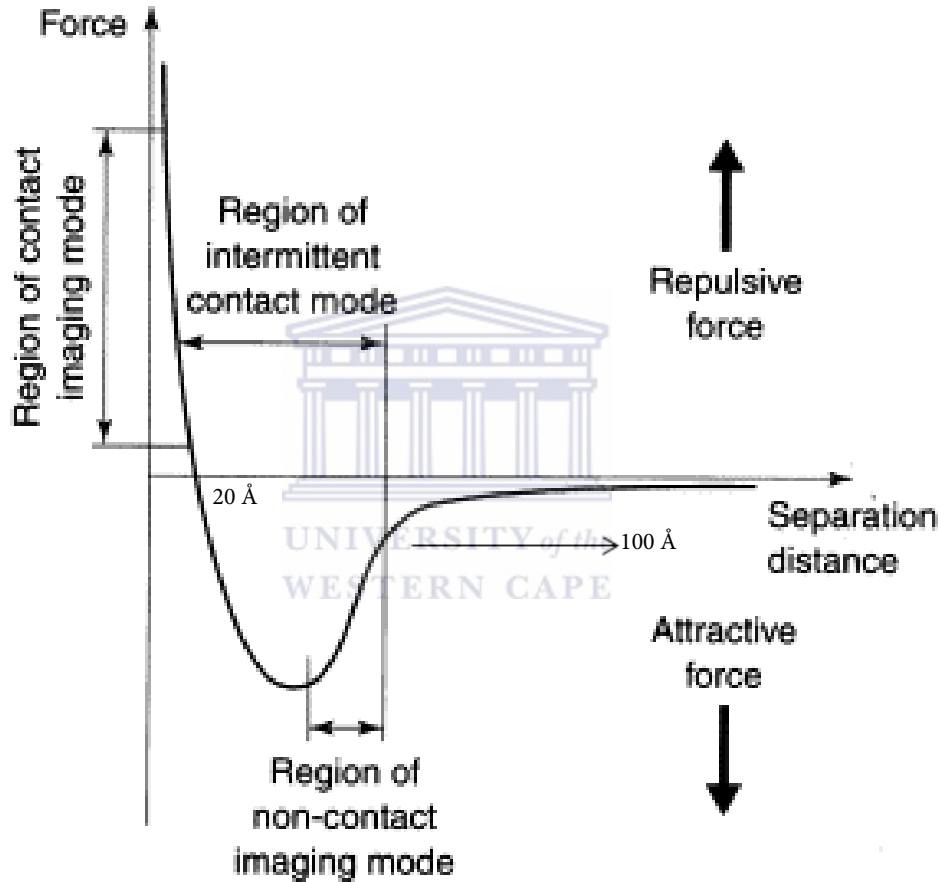


**Figure 2.13:** contact modes for obtaining AFM images [2.16].

When operation occurs in the non-contact region van de Waals forces are dominant and the separation distance is in the region 10 – 100 Å. Intermittent contact is in the region 5 – 20 Å and contact distance is less than 5 Å where repulsive forces are dominant.

## EXPERIMENTAL METHODS

The current study was performed in constant force tapping mode, which was in the non-contact region. This is the most common operating mode and in this system the tip intermittently taps the sample surface at the cantilever resonance frequency. The Force is described by the equation below:

$$F = k\Delta z \quad (2.20)$$

Where  $F$  is the force,  $k$  is the cantilever spring constant and  $\Delta z$  is the tip displacement. During the constant force tapping mode  $\Delta z$  is adjusted in order to maintain a constant  $F$  throughout the measurement.

A schematic of the experimental set-up can be viewed in figure 2.14. The tip mounted on the cantilever probes the sample surface. The laser beam is directed toward a reflective surface on the back of the cantilever during the lateral movements of the cantilever. The reflected laser beam is then received by the photodiode detector. The detector is in a feedback loop with the piezoelectric scanner and relays signals to the piezoelectric scanner regarding the movement of the tip. The tip is moved using a piezoelectric movement system and these movements constitute the image produced during AFM measurements.

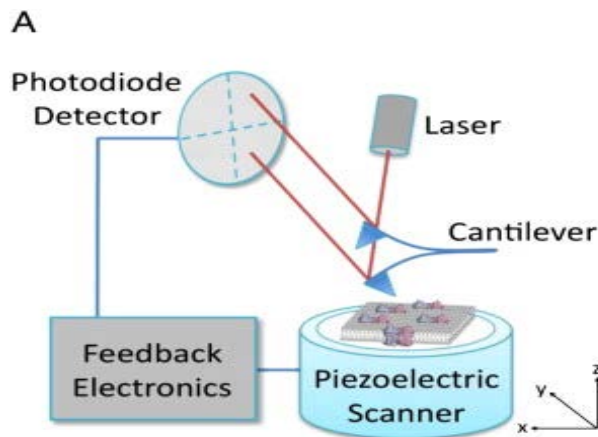


**Figure 2.14:** Schematic of experimental set-up for AFM measurements [2.17].

### 2.3.6 ELASTIC RECOIL DETECTION ANALYSIS

#### INTRODUCTION

Elastic Recoil Detection Analysis (ERDA) is a technique widely used for elemental analysis within the thin films industry. This comes as a result of the absolute nature of the technique. The detection system and projectile may vary depending on the type of element being analysis, but the underlying principle remains the same. In the current study normal ERDA was performed using alpha particles and a semiconductor detector for H quantification and Time of Flight Heavy Ion ERDA (TOF-HIERD) was performed in order to quantify Si and N in the a-SiN:H thin films.



#### THEORY

It can be seen from figure 2.14 that a collimated beam of charged projectile atoms are incident on the target/sample. As a result of the incident projectile ( $M_1$ ), with energy  $E_0$ , having a greater mass than sample atom ( $M_2$ ), the target atom is recoiled with energy  $E_2$ .

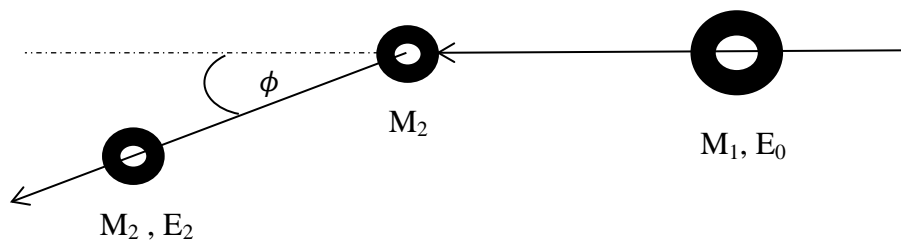


**Figure 2.15:** Schematic of the kinematics on the lab scale.

The yield of detected atoms can be described by equation 2.21.

$$Y = Q\Omega N_s \int_0^{E_0} \frac{d\sigma}{d\Omega}(E, \phi) \left(\frac{dE}{dx}\right)^{-1} dE \quad (2.21)$$

**ERDA**

H content was determined using a 3 MeV mono-energetic and collimated beam of  ${}^4\text{He}^+$  ions accelerated by a van de Graaff accelerator, where the recoiled H atoms were detected at an angle of  $30^\circ$  with respect to the incident ion beam. The H depth-profile was simulated using the SIMNRA simulation software for hydrogen quantification.

An aluminium range foil (surge foil) was used to stop any forward scattered alpha particles from inflating the recoil signals to the detector. The range foil had thickness  $7\ \mu\text{m}$  and was sufficient to allow H atoms to the detector. The particles were detected by a solid state detector mounted in the plane of the beam. A schematic of the experimental set-up can be viewed in figure 2.16.

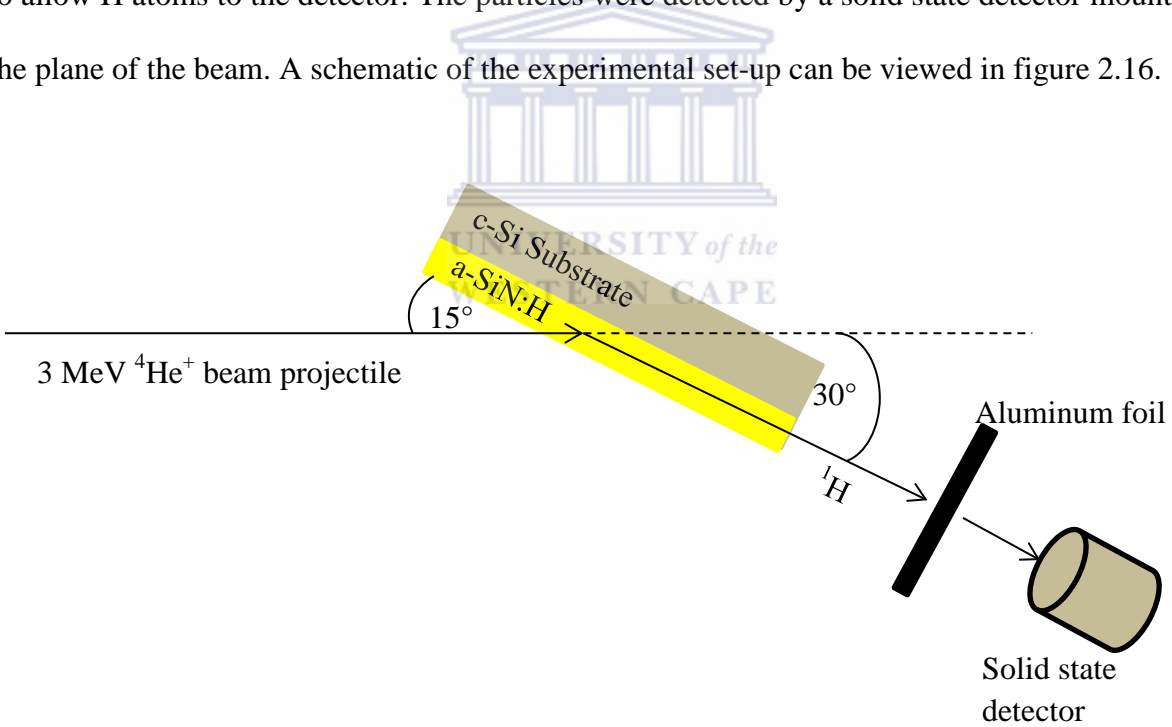


**Figure 2.16:** Schematic of ERDA set-up performed on samples

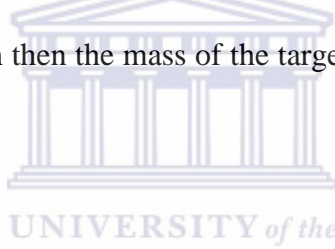
The projectile energy and the recoiled atom energy can be related by the kinematic factor as follows [2.18 – 2.19].

$$E_2 = KE_0 \quad (2.22)$$

Where;

$$K = \frac{4M_1M_2}{(M_1+M_2)^2} \cos^2\phi \quad (2.23)$$

The variables  $M_1$ ,  $M_2$ , and  $\phi$  in equation 2.23 are the mass of projectile, mass of target and scattering angle respectively. The energy of the projectile, kinematic factor and energy of forward scattered atom is given by  $E_0$ ,  $K$  and  $E_2$  respectively. If the kinematic factor, projectile mass and scattering angle is known then the mass of the target atoms can be determined and thus the identity of the target atom.



The Rutherford differential cross section is another important parameter in ERDA as this allows determination of the probability of the projectile recoiling a target atom in the direction of the solid state detector. The Rutherford differential cross section can be determined by [2.18-2.19]:

$$\frac{d\sigma}{d\Omega} = \left( \frac{Z_1 Z_2 e^2 (1 + \frac{M_1}{M_2})}{2E_0} \right)^2 \frac{1}{\cos^3\phi} \quad (2.24)$$

Where  $\Omega$  is the detector solid angle and  $e$  is the electron charge.

After passing through the aluminium foil the recoil atoms from the sample hit and dissipate their energy in the solid-state detector. This results in a series of electronic signals being generated, which are then interpreted and amplified by the electronics of the detection system. The signals

are then sorted by means of a multi-channel analyser according to their energy and the resulting spectrum is displayed in figure 2.17.

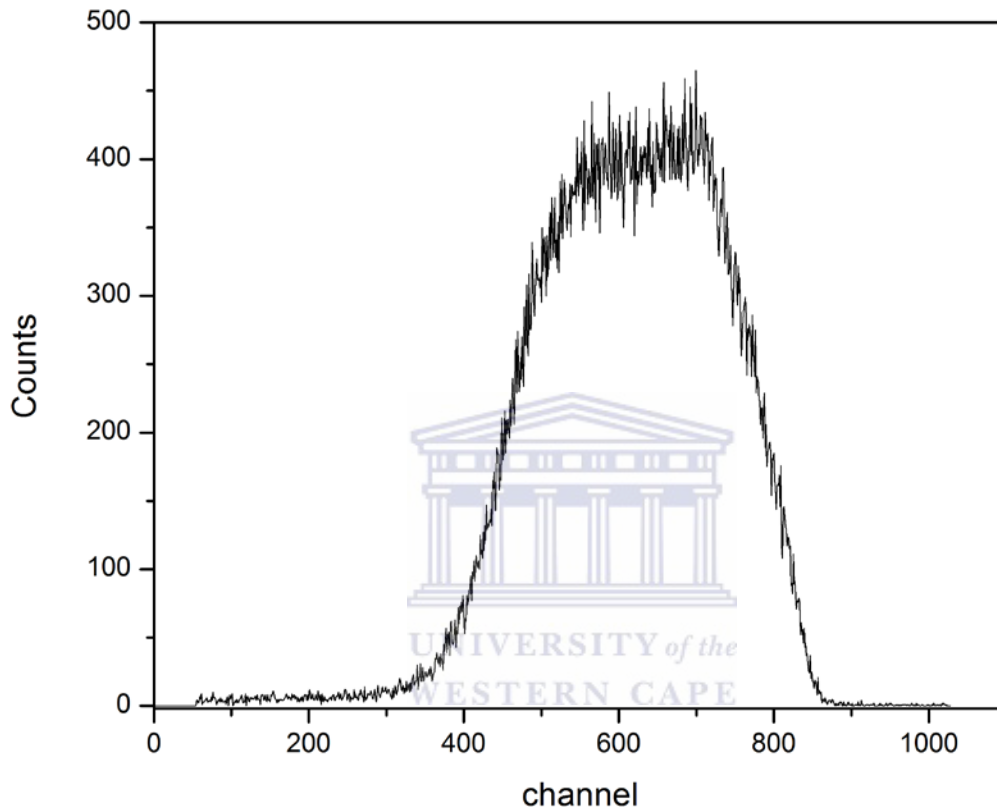


*Figure 2.17:* ERDA spectrum of a-SiN:H sample containing ~9 at.% H.

### **ToF – HIERD**

The underlying principles for ToF-HIERD are similar to that described for normal ERDA, however the detector system varies. The kinematics is still described by the schematic shown for figure 2.15. Thus in order to shed light on the technique the method of detection will be discussed. The projectile used for determining the N and Si content was  $^{73}\text{Cu}^{7+}$  at 26.3 MeV with

a 10 nA current. The projectiles were produced in a 6 MV tandem accelerator at iThemba labs Gauteng. A schematic of the detector system is shown in figure 2.18.

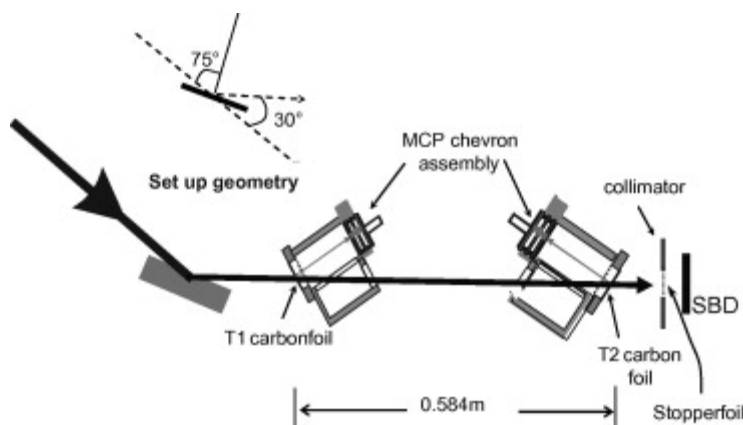


**Figure 2.18:** Schematic of ToF detector system used in present study [2.20].

The detector consists of two timing detectors labelled T1 and T2 as shown in figure 2.18. In the current study the flight distance was 0.6 m and at the point SBD there was a PIPS detector located behind T2. The timing detectors consist of a  $9.0 \mu\text{cm}^{-2}$  carbon foil positioned 5 cm from a micro channel plate (MCP) in Chevron configuration. The recoil atoms pass through the carbon foils and at each passing results in the ejection of electrons from the foil. The electrons are then accelerated from the foil to the MCP by means of an applied electric field, where the signal is amplified to allow rapid timing signal [2.20-2.21].

The time of flight is measured by the timing detectors which allows for determination of velocity and from this information the mass of the species can be obtained from the kinetic energy as in equation 2.25.

$$m_i = 2E_i \left( \frac{\Delta t}{l} \right)^2 \quad (2.25)$$

The variables  $m_i$ ,  $E_i$ ,  $\Delta t$  and  $l$  are the mass, energy, time of flight and distance travelled of the recoiled atoms respectively. The depth profile of the sample can be obtained from the effective energy loss per unit depth as in equation 2.26.

$$[S]_{eff} = \frac{dE_f}{dx} \quad (2.26)$$

The data acquisition software was MIDAS and a typical spectrum of ToF-HIERD for a-SiN:H is shown in figure 2.19.

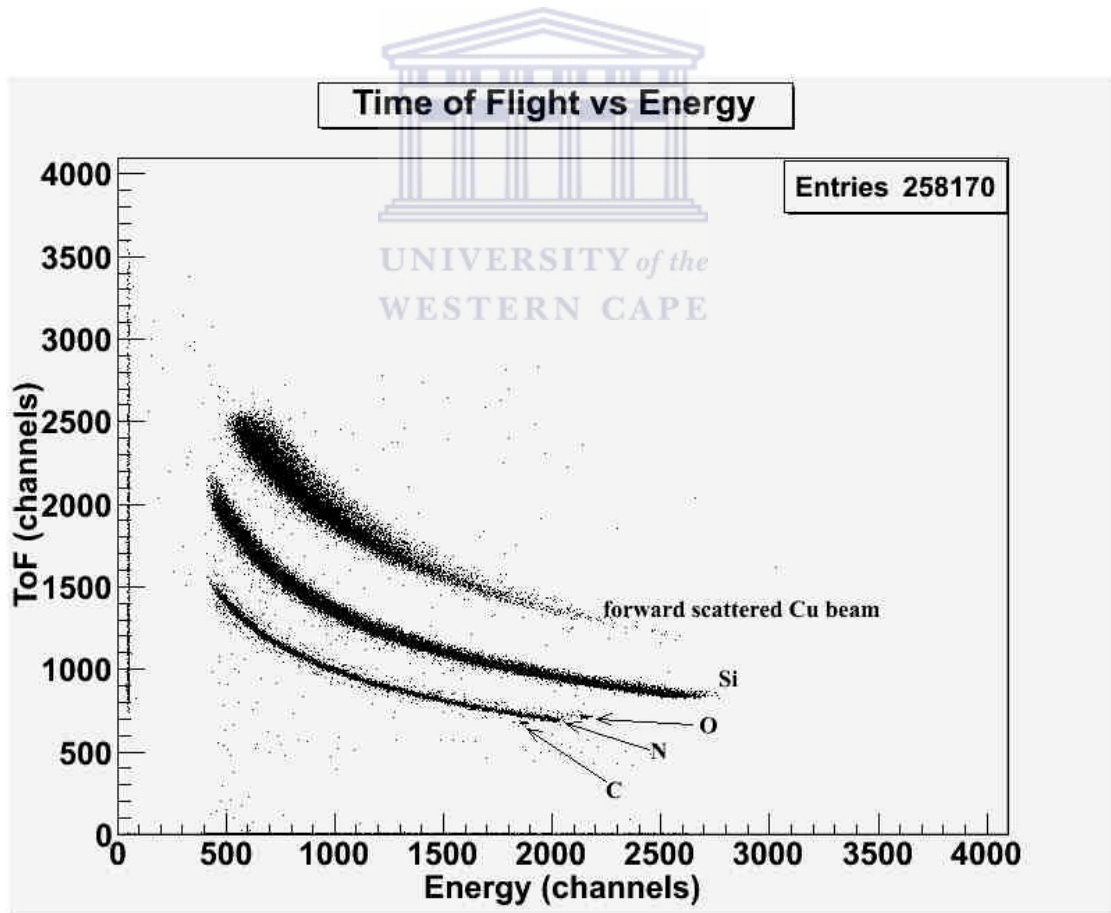


**Figure 2.19:** Raw spectrum obtained from MIDAS software for film containing N/Si = 0.17.

### **2.3.7 X-RAY DIFFRACTION**

X-Ray Diffraction (XRD) is a technique widely used in the materials research society. This comes as a result of the invaluable information attained about long range order within the material structure and elemental identification [2.22]. The use of this technique however would not be possible if not for the X-Ray diffracting property of crystals discovered by von Laue in 1912. For the purpose of this study XRD was performed on a-SiN:H thin films deposited on corning 7059 glass to confirm the amorphous nature of the films.

#### **THEORY**

A crystal is a solid state material that has long range order in the atomic arrangements that compose the material. When X-Rays are incident on them they will diffract the X-Rays in a manner unique to that specific material and orientation. The principles of XRD can be understood by considering the following concepts; Point lattice, unit cell, Bravais lattice, Miller indices and Bragg's law.

#### **CRYSTALLOGRAPHY**

The point lattice shown in figure 2.20 is a simple representation of the actual material, where each point on the lattice represents an atom or molecule from the real material lattice. The point lattice is used as a coordination system when an origin is defined. A specific vector, plane and point in the lattice can be described by the convention  $[u\ v\ w]$ . The coordinate convention can be better understood by considering a unit cell.

The unit cell (illustrated in figure 2.21) consists of one segment of the point lattice and when repeated infinitely will form the point lattice. The unit cell can be described by the three vectors shown as **a**, **b** and **c** extended from the origin. These vectors form the crystallographic axis of the crystal and are described by their magnitude *a*, *b* and *c*; and direction/ angle  $\alpha$ ,  $\beta$  and  $\gamma$  respectively. The scalar quantities described here are known as the lattice constants for the unit cell and are instrumental in the identification of the orientation and make-up of a specific crystalline material. The position vector **r** can be described using the position vectors shown in figure 2.21 by [2.23]:

$$\mathbf{r} = u\mathbf{a} + v\mathbf{b} + w\mathbf{c} \quad (2.27)$$

Where *u*, *v* and *w* are integers and allow for the simple description of the direction vector as [*u v w*]. The system shown in figure 2.21 is known as triclinic and there exist other systems (as shown in table 2.3) that vary depending on the orientation and position of the points in the lattice system. When symmetry operations are performed on a lattice point in these systems and the lattice remains invariant, this gives rise to the Bravais lattices as shown in table 2.3.

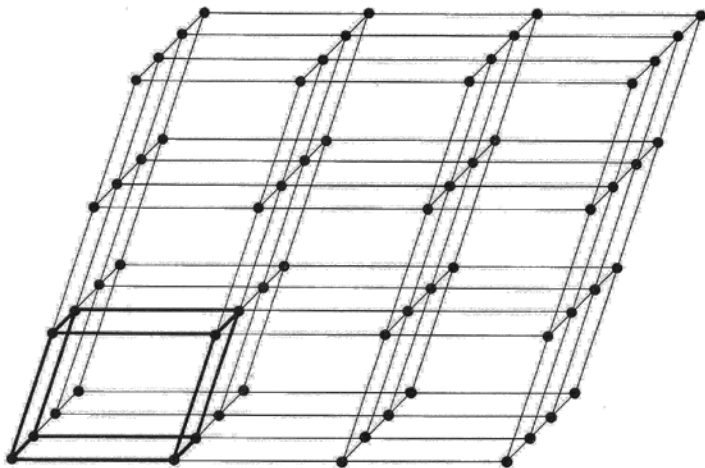


**Figure 2.20:** simple unit cell of an arbitrary material [2.22].

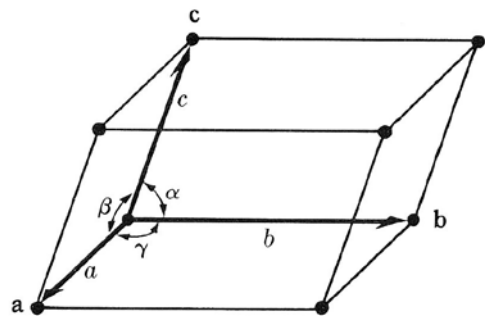


**Figure 2.21:** unit cell [2.22].

**Table 2.3 :** Various Bravais lattices.

System	Axial lengths and angles	Bravais lattice	Lattice symbol
Cubic	Three equal axes at right angles $a = b = c, \alpha = \beta = \gamma = 90^\circ$	Simple Body-centered Face-centered	P I F
Tetragonal	Three axes at right angles, two equal $a = b \neq c, \alpha = \beta = \gamma = 90^\circ$	Simple Body-centered	P I
Orthorhombic	Three unequal axes at right angles $a \neq b \neq c, \alpha = \beta = \gamma = 90^\circ$	Simple Body-centered Base-centered Face-centered	P I C F
Rhombohedral	Three equal axes, equally inclined $a = b = c, \alpha = \beta = \gamma \neq 90^\circ$	Simple	R
Hexagonal	Two equal coplanar axes at $120^\circ$ , third axis at right angles $a = b \neq c, \alpha = \beta = 90^\circ, \gamma = 120^\circ$	Simple	P
Monoclinic	Three unequal axes, one pair not at right angles $a \neq b \neq c, \alpha = \gamma = 90^\circ \neq \beta$	Simple Base-centered	P C
Triclinic	Three unequal axes, unequally inclined and none at right angles $a \neq b \neq c, \alpha \neq \beta \neq \gamma \neq 90^\circ$	Simple	P

Planar orientations within a lattice can be represented according to the miller indices  $h, k$  and  $l$  as  $(h\ k\ l)$ . The sketch in figure 2.22 shows the vector  $\mathbf{n} = \mathbf{a}_1/h + \mathbf{a}_2/k + \mathbf{a}_3/l$  to be normal to the  $(h\ k\ l)$  plane and intercepting the unit cell at  $\mathbf{a}_1/h, \mathbf{a}_2/k$  and  $\mathbf{a}_3/l$  where  $\mathbf{a}_1, \mathbf{a}_2$  and  $\mathbf{a}_3$  are the crystallographic axis. Planes of similar form are denoted by  $\{h\ k\ l\}$ .

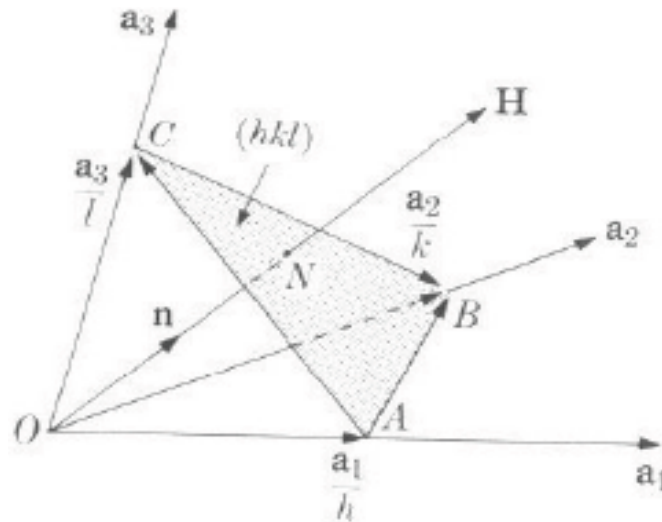


Figure 2.22: Reciprocal lattice vector and crystal plane.

### BRAGG'S LAW

Bragg's law describes the parallel planes that allow x-rays to undergo specular reflection. Consider figure 2.23 where two waves that are in-phase are incident on a crystal lattice. The angle of incidence is given by  $\theta_B$  and the planes are separated by a distance  $d$ . The path difference,  $CB + BD$  for constructive interference to occur, must be an integer multiple of the wavelength  $\lambda$ . The Bragg's law equation allows for the determination of the interplanar spacing if the angle of incidence and wavelength is known by:

$$2d\sin\theta_B = n\lambda \quad (2.28)$$

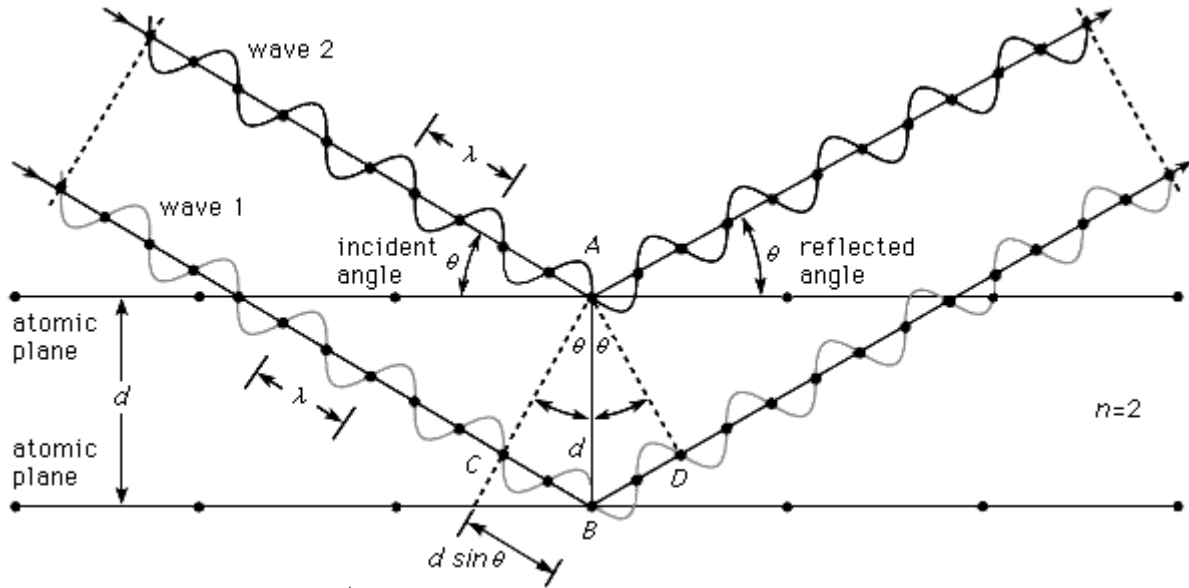


Figure 2.22: Illustration of Bragg's law [2.23]

The notion of reciprocal lattice stems from the inverse relation between incident angle and interplanar spacing illustrated in equation 2.28. The reciprocal lattice describes each plane of the real lattice as point in the reciprocal lattice as illustrated in figure 2.22. The reciprocal lattice vector  $\mathbf{g}^*$  extended from the origin of the reciprocal lattice is given by equation 2.29:

$$\mathbf{g}^* = h\mathbf{a}^* + k\mathbf{b}^* + l\mathbf{c}^*$$

Where  $|\mathbf{a}^*| = \frac{1}{a}$

$$|\mathbf{b}^*| = \frac{1}{b}$$

$$|\mathbf{c}^*| = \frac{1}{c}$$

(2.29)

The concept of the reciprocal lattice is important in the consideration of the structure factor. This is the sum of all the scattered radiation from all atoms in the unit cell. The structure factor can be related to intensity by:

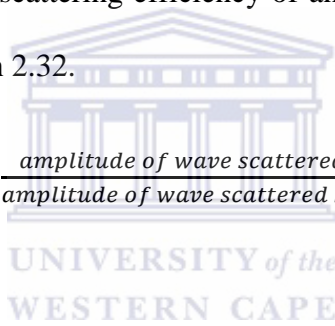
$$I = |F_{hkl}|^2 \quad (2.30)$$

Where:

$$F_{hkl} = \sum_1^N f_n \exp 2\pi i(hu_n + kv_n + lw_n) \quad (2.31)$$

The summation of equation 2.31 spans all atoms in the unit cell N and  $f_n$  form factor. The form factor is used as a measure of the scattering efficiency of any given crystallographic atom. The form factor is described in equation 2.32.

$$f_n = \frac{\text{amplitude of wave scattered by an atom}}{\text{amplitude of wave scattered by an electron}} \quad (2.32)$$



### **EXPERIMENTAL SET-UP**

A schematic of a typical XRD set-up is illustrated in figure 2.24. The diffractometer consists of an X-ray source at point S in the sketch, which incidents monochromatic x-rays toward the sample mounted at point C. The specimen mount H can rotate the specimen and throughout rotation a constant  $2\theta$  proportionality angle is maintained between H and E. A and B are beam collimator slits that define and collimate the beam after leaving the sample and before entering the detector.

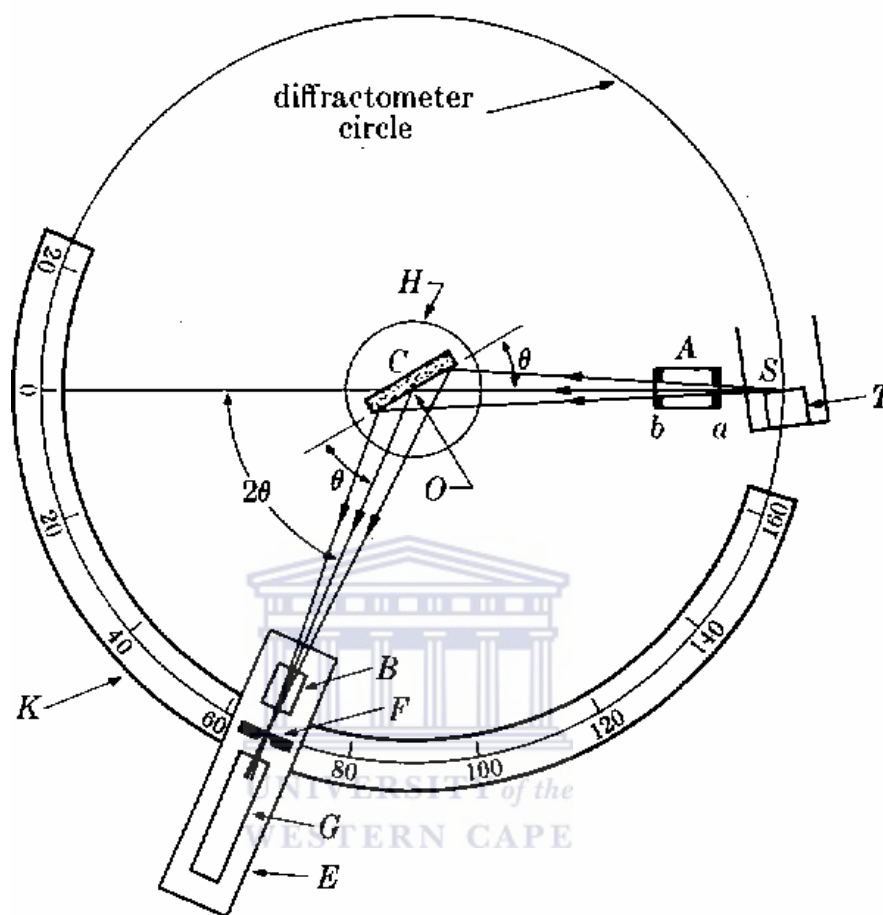


Figure 2.24: schematic of diffractometer [2.22]

## 2.4 REFERENCES

- [2.1] C. J. Arendse, MSc. Thesis, University of the Western Cape, Bellville, Cape Town
- [2.2] C. J. Arendse, Phd. Thesis, University of the Western Cape, Bellville, Cape Town
- [2.3] J. Müllerová and J. Mudroň, *Acta Phys. Slov.*, **50**, p 477 (2000)
- [2.4] N. F. Mott and E. A. Davis, *Electronic processes in Non-Crystalline Materials*, Clarendon Press, Oxford, UK (1971)
- [2.5] R. Zallen, *The physics of amorphous Solids*, John Willeu (1983)
- [2.6] Semiconsoft inc., *Mprobe brochure*,  
[Online] [http://www.semiconsoft.com/html/download/brochure/MProbe\\_brochure2012.pdf](http://www.semiconsoft.com/html/download/brochure/MProbe_brochure2012.pdf), accessed 2013/05/21
- [2.7] J. Tauc, *Optical Properties of Solids*, F. Abeles, North-Holland Publ., Amsterdam (1972)
- [2.8] S. K. O’Leary, P. K. Johnson and P. K. Lim., *J. App. Phys.*, **82**, p 3334 (1997)
- [2.9] M. H. Brodsky, M. Cardona and J. J. Cuomo *Phys. Rev. B*, **30**, p 3556 (1977)
- [2.10] Maley N *Phys. Rev. B*, **46**, p 2078 (1992)
- [2.11] P. J. Goodhew and F. J. Humphreys, *Electron Microscopy and Analysis*, 2nd Edition, Taylor & Francis, London (1988)
- [2.12] [Online] <http://www.xos.com/techniques/spectroscopy/eds-spectroscopy>, accessed 2013-05-22

- [2.13] J. Stettner, L. Schwalowsky and O.H. Seeck , *Phys. Rev. B*, **53**, p 1398 (1996)
- [2.14] O.P. Karpenko, S.M. Yalisove and D.J. Eaglesham, *J. Appl. Phys.*, **82**, p1157 (1997)
- [2.15] A. Munkholm, S. Brennan and E.C. Carr, *J. Appl. Phys.*, **82**, p 2944 (1997)
- [2.16] W. R. Bowen, N. Hilal, R. W. Lovitt and C. J. Wright, *Encyclopedia of Food Microbiology*, P 1418 (1999)
- [2.17] A. M. Whited and P. S. Park, “Atomic force microscopy: A multifaceted tool to study membrane proteins and their interactions with ligands”, *Biochimica et Biophysica Acta (BBA) – Biomembran* (2013)
- [2.18] L.C. Feldman and J. C. Mayer, *Fundamentals of surface and thin film analysis*, North-Holland Publ., Amsterdam (1986)
- [2.19] J. R. Tesmer, M. Nastasi, J. C. Barbour, C. J. Maggiore and J. W. Mayer, *Handbook of modern ion beam materials analysis*, Pittsburgh, Pennsylvania (1995)
- [2.20] M. Msimangaa, C.M. Comrie, C.A. Pineda-Vargasa, S. Murraya, R. Barka and G. Dollinger, *Nuclear Instruments and Methods in Physics Research Section B: Beam Interactions with Materials and Atoms*, **267**, p 2671 (2009)
- [2.21] M. Msimanga, D. Wamwangi, C.M. Comrie, C.A. Pineda-Vargas, M. Nkosi, T. Hlatshwayo, *Nuclear Instruments and Methods in Physics Research B*, **296**, p 54 (2013)
- [2.22] B. D. Cullity, “*Elements of X-Ray diffraction*”, Addison-Wesley Publishing company, Reading , Massachusetts (1978)

[2.23] C. Kittel, "*Introduction to solid state physics*", 8<sup>th</sup> edition, John Wiley and sons, USA  
(2005)

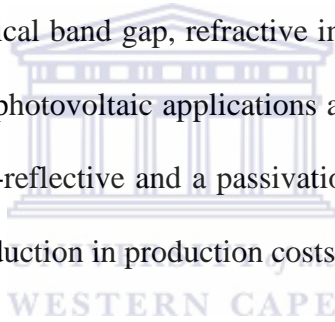


# CHAPTER 3

## RESULTS AND DISCUSSION

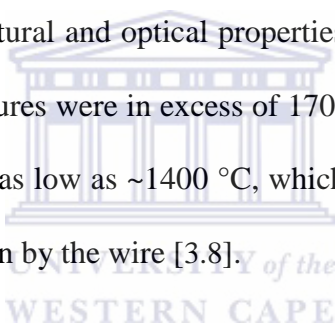
### 3.1 INTRODUCTION

Hot wire chemical vapour deposition (HWCVD) a-SiN:H has a vast amount of applications, including thin film transistors, anti-reflective coatings in thin film solar cells, passivation layers and oxidation barriers [3.1]. The variety of applications is attributed to the tunability of the material properties such as the optical band gap, refractive index and mass density. Thin film a-SiN:H has a distinct advantage in photovoltaic applications as opposed to oxide layers, as it can perform a dual function as an anti-reflective and a passivation layer [3.2]. This material duality provides an excellent means for reduction in production costs.



Plasma enhanced chemical vapour deposition (PECVD) is the industrial technique of choice for the production of device quality a-SiN:H thin films; mainly due to its reproducibility. However, PECVD has its drawbacks in terms of film quality caused by ion bombardment, which results in void formation and undesirable oxidation [3.3]. The production of radicals in the deposition process of HWCVD a-SiN:H results in film damage being lessened and thus better quality films being produced. HWCVD also has the advantage of ease-of-upscale as indicated by Lederman *et al* [3.4]. The absence of plasma in HWCVD also results in the elevation of thin film growth rate, since there is increased gas decomposition efficiency in HWCVD.

The properties of the a-SiN:H thin films produced by HWCVD are highly dependent on the deposition process and conditions. The source gases used in this study are NH<sub>3</sub>, SiH<sub>4</sub> and H<sub>2</sub>; and the film properties have been shown to be highly dependent on the flux of these precursor gases. These parameters have been shown to vary the N/Si content, which in turn leads to variations in the structural and optical properties [3.5]. Thus, in the chapter to follow, the deposition process will be investigated by varying the deposition parameters such as deposition pressure, NH<sub>3</sub> flow rate, Total flow rate and H<sub>2</sub> flow rate. The successful optimization of HWCVD a-SiN:H can lead to it becoming a viable, cheaper alternative to PECVD a-SiN:H thin films for photovoltaic application. This is the motivating factor for studying the effect of low processing parameters on the structural and optical properties of a-SiN:H thin films. In the case of many studies, filament temperatures were in excess of 1700 °C [3.5 - 3.7], where in this study the filament temperature used was as low as ~1400 °C, which allows for significant reduction in the possibility of film contamination by the wire [3.8].



## 3.2 EXPERIMENTAL DETAILS

### 3.2.1 DEPOSITION PARAMETERS

Table 3.1 shows the deposition parameters used for this study. For the preparation of series one and two all parameters were kept constant, such as wire temperature, substrate temperature and pressure and the NH<sub>3</sub> ( $\Phi_{\text{NH}_3}$ ) and SiH<sub>4</sub> ( $\Phi_{\text{SiH}_4}$ ) flow rate were varied, respectively. Similar parameters were used for series 3 and 4; however the deposition pressure and total flow rate was varied with no substrate heating and a wire temperature of 1650°C.

**Table 3.1:** Deposition parameters; N.B. for series 4 the H<sub>2</sub>/NH<sub>3</sub>/SiH<sub>4</sub> ratio was constant

	<b>P (μbar)</b>	<b>Φ<sub>SiH4</sub></b> (SCCM)	<b>Φ<sub>NH3</sub></b> (SCCM)	<b>Φ<sub>H2</sub></b> (SCCM)	<b>Φ<sub>Total</sub></b> (SCCM)	<b>T<sub>wire</sub> (°C)</b>	<b>T<sub>Substrate</sub></b> (°C)
<b>Series 1</b>	100	5	1 – 7	20	NA	1400	259
<b>Series 2</b>	100	2.5	3.5	10 – 30	NA	1400	259
<b>Series 3</b>	20 – 120	2.5	3.5	10	NA	1650	Wire only
<b>Series 4</b>	100	2.5 - 5	3.5 - 7	10 - 20	16 - 32	1650	Wire only

### 3.2.2 CHARACTERIZATION

FTIR was performed using a Perkin Elmer Spectrum 100 spectrophotometer from 400 – 4000 cm<sup>-1</sup> with a resolution of 4 cm<sup>-1</sup>. The spectra were corrected for coherent and incoherent reflections according to Brodsky *et al* [3.9] and Maley *et al* [3.10]. The integrated absorption of SiH and NH was used as an indication of bonded hydrogen and the integrated absorption of SiN stretching mode was used as an indication of bonded N. UV-VIS was performed using a Semiconsoft thin film spectrometer in reflection geometry in the range 200 – 900 nm with a resolution of 1 nm. The optical spectra were modelled using Scout® software, which implemented a model for a theoretical amorphous semiconductor, developed by O’Leary *et al* [3.11] to determine the thin film thickness, band gap and refractive index. AFM was performed with a Veeco Atomic Force Microscope (AFM) in tapping mode to determine the surface roughness.

Elastic recoil detection analysis (ERDA) was conducted using a 3 MeV mono-energetic and collimated beam of <sup>4</sup>He<sup>+</sup> ions, where the recoiled H atoms were detected at an angle of 30° with

respect to the incident ion beam. The H depth-profile was simulated using the SIMNRA simulation software for hydrogen quantification. Time of flight Heavy ion ERD (ToF-HIERD) was performed using a 26 MeV Cu<sup>7+</sup> beam at a scattering angle of 30° using a time of flight detector system. X-ray diffraction (XRD) was performed using a PANalytical Xpert diffractometer at 2θ-values ranging from 5 – 90°, with a step size of 0.02°. Copper Kα<sub>1</sub> radiation with a wavelength of 1.5406 Å was used as the x-ray source. EDS was performed using an Oxford INCA energy system attached to a 1525 Leo FEGSEM. The accelerating voltage was 6 kV, aperture size 30 microns and a working distance of 8 mm.

### **3.3 DEPOSITION RATE AND MORPHOLOGY**

In this section the deposition rate of hot wire chemical vapour deposited (HWCVD) a-SiN:H will be investigated. The deposition rate, defined as the film thickness per unit deposition time, forms a vital role in the industrial applicability of hot wire chemical vapour deposited a-SiN:H. In this thesis, the film thickness was determined optically using UV-vis spectroscopy. It is of utmost importance to consider the deposition process when the deposition rate is under question. The deposition process can be considered as three simultaneous processes; namely (a) decomposition of inlet gases at the filament surface, (b) secondary gas phase chemistry of radicals produced by the decomposition of inlet gases and (c) film growth at the substrate surface, resulting from radicals produced by secondary gas phase reactions. In a system where purely SiH<sub>4</sub> is present in the chamber silicon and atomic hydrogen is produced at the filament according to the following sequential reactions [3.12]:





The hydrogen atoms produced in equation 3.4 react in the gas phase with  $\text{SiH}_4$  molecules, that were not decomposed over the filament, to form  $\text{SiH}_3$  as in equation 3.5 [3.13 – 3.14]. The  $\text{SiH}_3$  produced, results in the production of film forming species in the following manner;

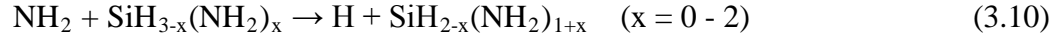


Ammonia was decomposed at a tungsten filament by Umemoto *et al.* [3.15] and the primary radicals formed at the filament were  $\text{NH}_2$  and  $\text{H}$ , which then reacted in the gas phase to produce stable species like  $\text{H}_2$  and  $\text{N}_2$ . The  $\text{H}_2$  species are formed by the reaction;



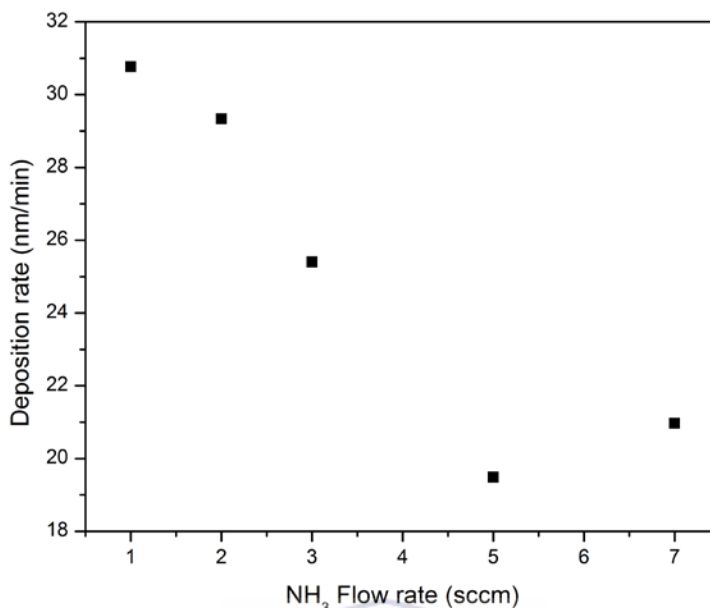
In the presence of  $\text{NH}_3$  and  $\text{SiH}_4$  the reactions in the three phases tend to be complex and dependent on the  $\text{NH}_3/\text{SiH}_4$  ratio in the chamber. The two inlet gases compete for active sites at the filament surface where  $\text{SiH}_4$  is the more dominant species at the tantalum filament and ammonia is scarcely dissociated, as observed by Eustergerling *et al* [3.16]. The dissociation efficiency of  $\text{NH}_3$  is drastically decreased by the addition of  $\text{SiH}_4$  [3.17]. This stands to reason for the high  $\text{NH}_3$  flow rates required for the production of device quality a-SiN:H thin films. The dissociation of  $\text{SiH}_4$  and  $\text{NH}_3$  at the filament surface, brings about the products shown in

equations 3.5 – 3.9, which react in the gas phase to produce triaminosilanes ( $\text{Si}(\text{NH}_2)_3$ ) and tetra-aminosilanes ( $\text{Si}(\text{NH}_2)_4$ ) in the following manner [3.18];



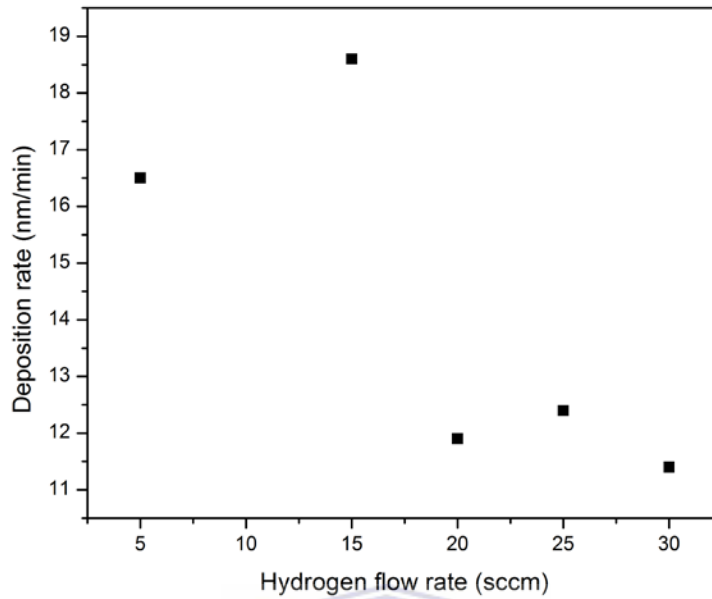
In the presence of low  $\text{NH}_3:\text{SiH}_4$  ratios, the chamber chemistry tends to be dominated by  $\text{Si}_2\text{H}_6$  and the behaviour is similar to cases where pure  $\text{SiH}_4$  is decomposed over the heated filament, as in equation 3.8. This result for low flow ratios was observed by Eustergling *et al.* [3.19], which yields thicker, silicon rich films for a  $\text{NH}_3:\text{SiH}_4$  ratio of 1. In the presence of elevated  $\text{NH}_3:\text{SiH}_4$  ratios (above 49),  $\text{Si}(\text{NH}_2)_4$  radicals are the dominant species produced, resulting in nitrogen rich films and decreased growth rate as a result of the decrease in silicon precursors.

Figure 3.1 represents the deposition rate as a function  $\text{NH}_3$  flow rate and shows a decrease in deposition as  $\text{NH}_3$  flow rate increases. Silicon precursors resulting from the decomposition of  $\text{SiH}_4$  over the tantalum filament are responsible for film growth [3.21]. As the  $\text{NH}_3$  flow rate is increased, silicon containing radicals are consumed to form aminosilanes, such as  $\text{Si}(\text{NH}_2)_3$  and  $\text{Si}(\text{NH}_2)_4$ . The formation of aminosilanes is a-SiN:H film forming precursor and result in the formation of Si-N bonds at the expense of Si-Si. The result obtained in figure 3.1 was also observed by Verlaan *et al* [3.20].



**Figure 3.1:** Deposition rate as function of NH<sub>3</sub> flow rate.

Despite the scarcity of literature, the effect of H<sub>2</sub> on the a-SiN:H thin film is significant. The effect of H<sub>2</sub> on the deposition rate is illustrated in figure 3.2. The increase in H<sub>2</sub> flow rate causes a sudden decrease in the deposition rate of the a-SiN:H thin films. Since NH<sub>3</sub> is dissociated in the gas phase by atomic hydrogen released by the dissociation of SiH<sub>4</sub> [3.22], the presence of H<sub>2</sub> in the chamber results in an increased atomic hydrogen presence, which in turn proliferates the dissociation of NH<sub>3</sub>. The increased dissociation of NH<sub>3</sub> produces elevated amounts of Si(NH<sub>2</sub>)<sub>3</sub> and Si(NH<sub>2</sub>)<sub>4</sub> at the expense of silicon film forming precursors. Ansari *et al* [3.23] observed NH<sub>3</sub> dissociation efficiency to increase from around 50% to 80%, with the addition of H<sub>2</sub>. The presence of H<sub>2</sub> at the filament surface also has an etching effect on the silicide contaminated filament surface, which also has a positive effect on the dissociation of NH<sub>3</sub>. The decrease in deposition rate observed in figure 3.2 was also observed by Liu *et al* [3.24] and was ascribed to the etching effect hydrogen has on the a-SiN:H thin film surface.



**Figure 3.2:** Deposition rate as a function of H<sub>2</sub> flow rate.

The gas phase reaction kinetics is highly dependent on the chamber pressure and thus it becomes a vital parameter in the deposition of a-SiN:H. The effect of pressure on the deposition rate is shown in figure 3.3 and is observed to increase as pressure increases. Since these a-SiN:H thin films have been deposited at low NH<sub>3</sub> flow rates, the reaction mixture is dominated by silicon containing radicals, as in equation 3.8. The increase in pressure results in an increase in the rate of formation of these radicals, and thus, an increase in the growth of the a-SiN:H film at the substrate surface. This results in thick, silicon rich films being produced, and confirms with the work of Stannowski *et al* [3.25].

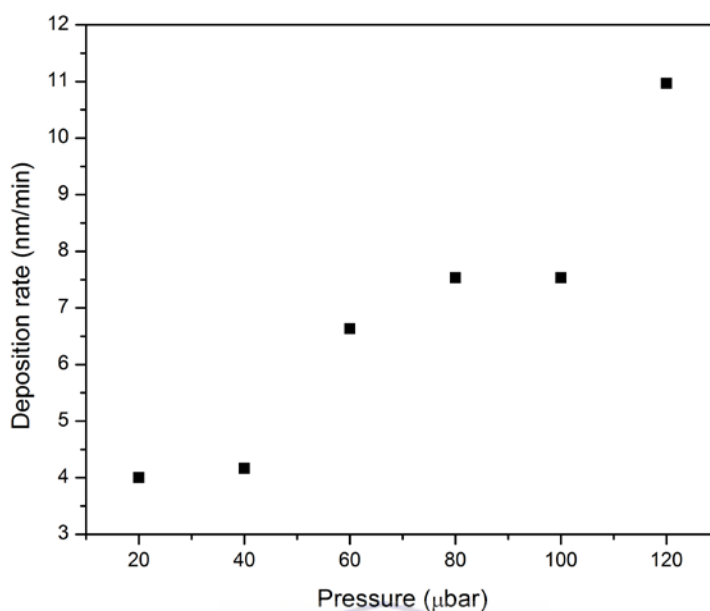


**Figure 3.3:** Deposition rate as a function of pressure.

Figure 3.4 shows the effect of total flow rate on the deposition rate and it is observed to increase as the total flow rate is increased. A common misconception is that if the  $\text{SiH}_4:\text{NH}_3:\text{H}_2$  ratio and pressure is kept constant, the deposition rate will remain constant, as at any given time the amount of molecules in the chamber is constant. This was not the case, as indicated in figure 3.4, as the gas flow rates are increased, all precursor species such as;  $\text{Si}(\text{NH}_2)_3$ ,  $\text{Si}(\text{NH}_2)_4$  and  $\text{Si}_2\text{H}_6$  are also increased due to the more rapid replenishment of inlet gases over the tantalum filament. Since the silicon radicals such as  $\text{Si}_2\text{H}_6$  are responsible for film growth, their increased presence results in an increase in the growth rate of the a-SiN:H films.

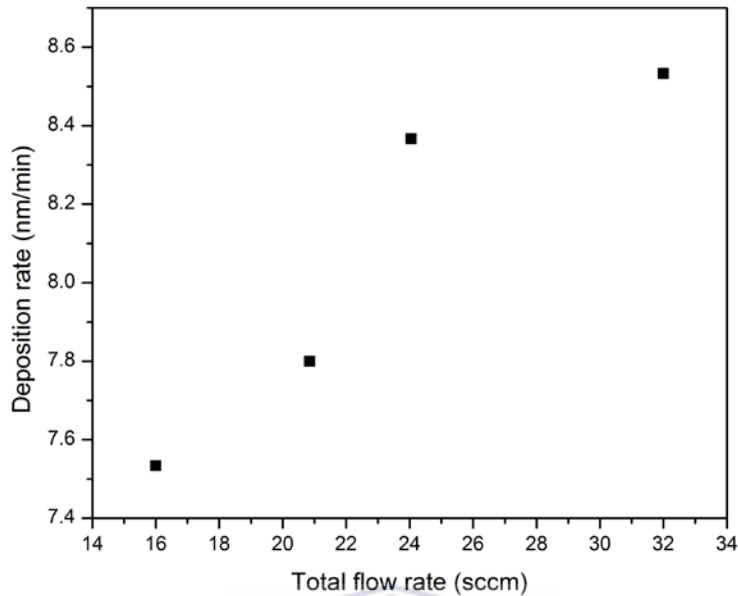


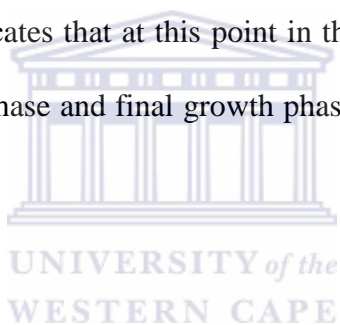
**Figure 3.4:** Deposition rate as a function of total flow rate.

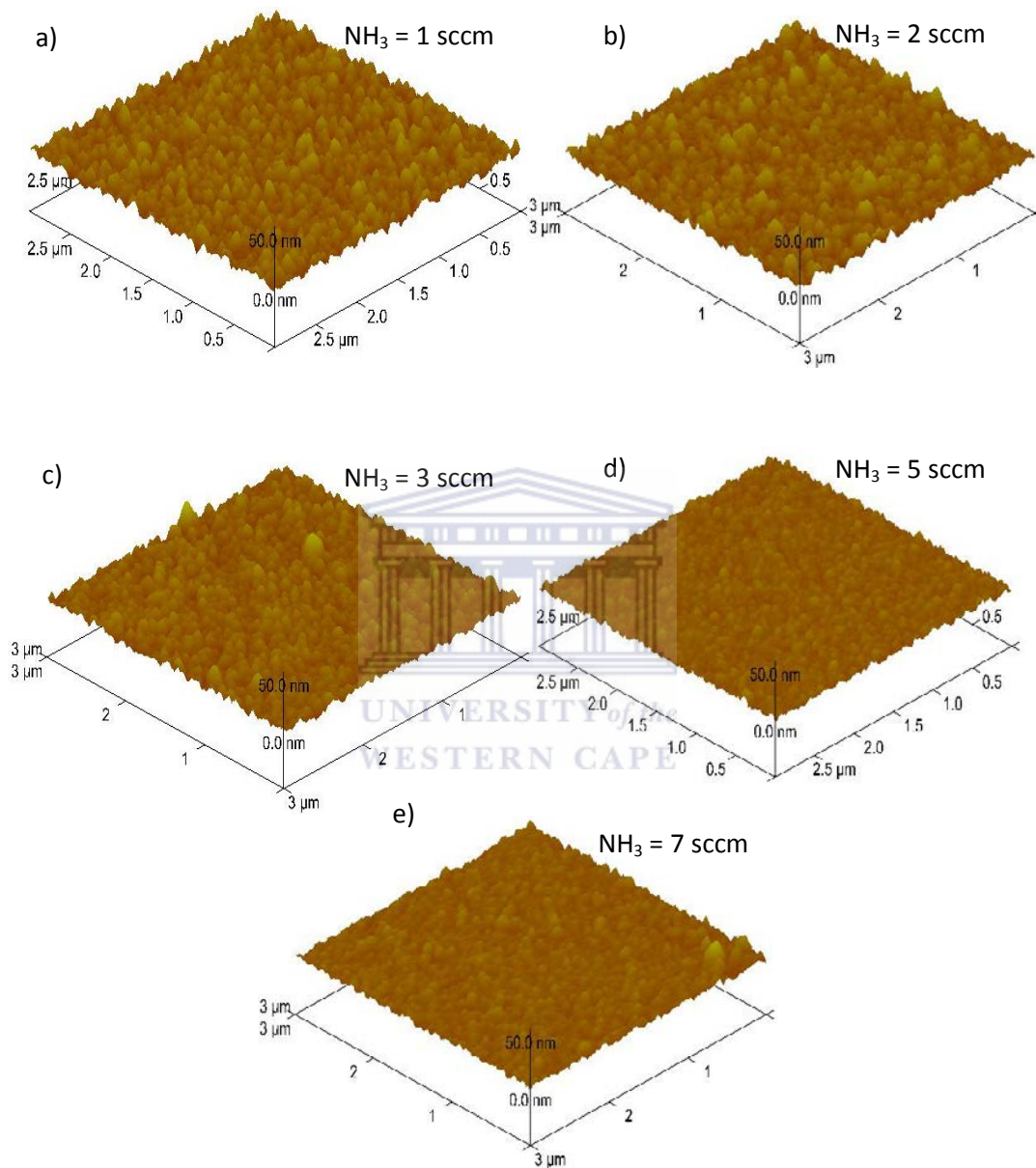
The thin film application of a-SiN:H in silicon Photovoltaic (PV) devices warrants investigation into the morphology of the deposited films, due to the surface roughness of the a-SiN:H layer playing a vital role in light trapping and also its passivation ability. When depositing on a rough surface the resulting layer will be non-uniform [3.27] and AFM studies are required for reproducibility. The AFM three dimensional (3D) images of the films prepared at various deposition parameters are displayed below in figure 3.5 – 3.8.

Figure 3.5 shows the AFM images of the series prepared by increasing the  $\text{NH}_3$  flow rate and it is apparent that as the  $\text{NH}_3$  flow rate is increased the grain sizes tend to decrease and the films appear smoother and less columnar. Since these films are not of comparable thicknesses (as can be seen from the deposition rate in figure 3.1), the increase in grain size and also roughness can be attributed to the variation in film thickness. Yu *et al* [3.27] investigated the effect of

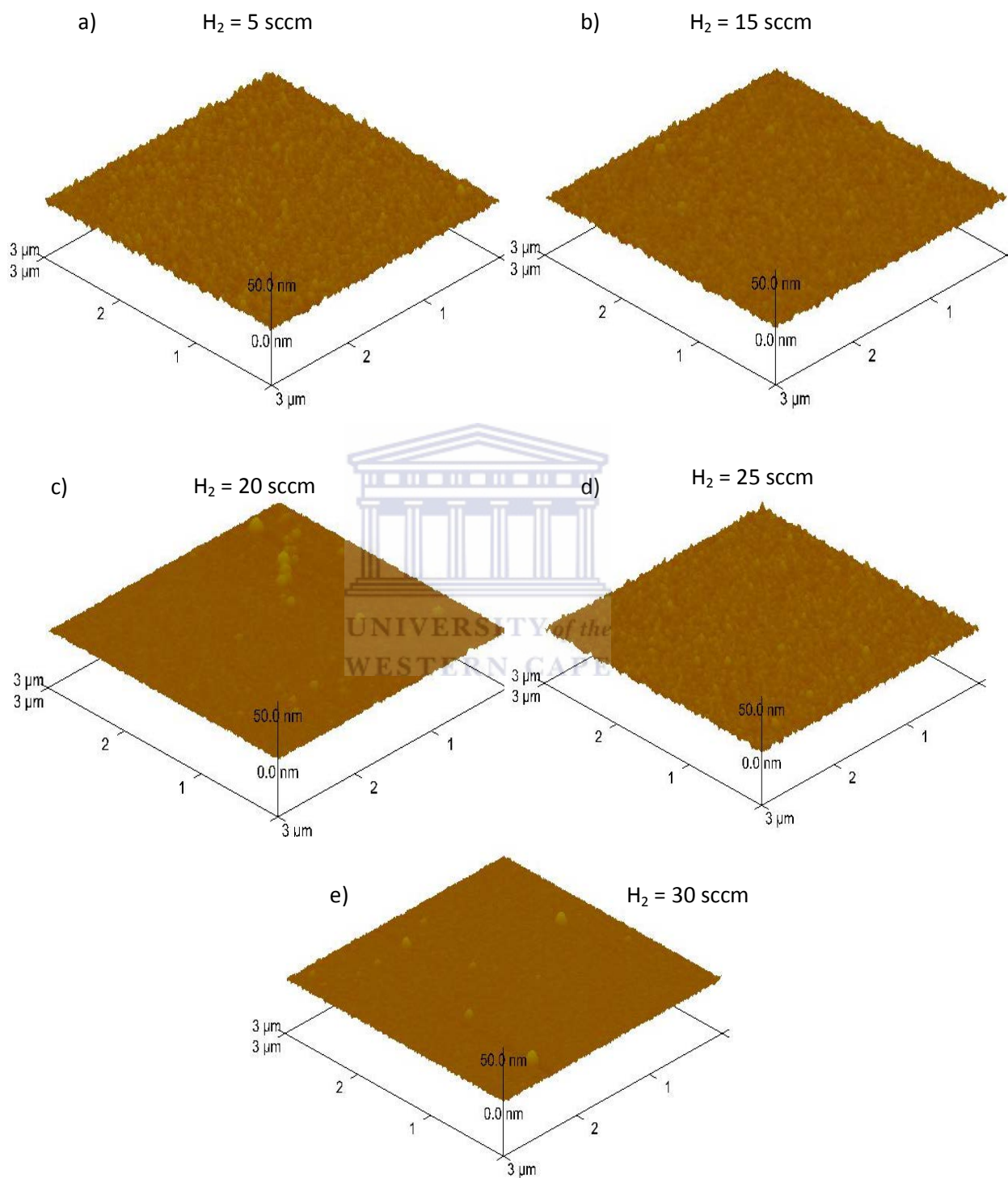
deposition time on the surface roughness and found that as films get thicker they tend to get rougher.

The AFM images showing the effect of increasing the H<sub>2</sub> flow rate is shown in figure 3.6. This shows a similar result to that observed in figure 3.5, as the H<sub>2</sub> flow rate increases the film tends to become smoother and less columnar. Since Figure 3.6 (c), (d) and (e) are of samples of comparable thickness, the apparent increased smoothness can be attributed to the increased H<sub>2</sub> flow rate resulting in increased nitrogen incorporation, which then leads to a decrease in the roughness of the film [3.22, 3.28]. Figure 3.6 (c) and (e) exhibits several columnar structures present on the surface, which indicates that at this point in the growth the film is in a transition phase between the initial growth phase and final growth phase, which will be discussed in detail for figure 3.9.





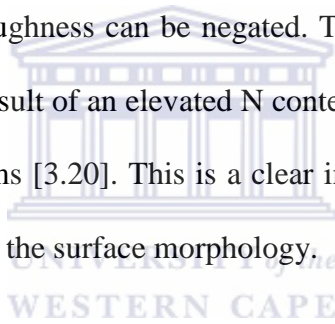
**Figure 3.5:** AFM images for films prepared by increasing NH<sub>3</sub> gas flow in order of increasing NH<sub>3</sub> flow rate.

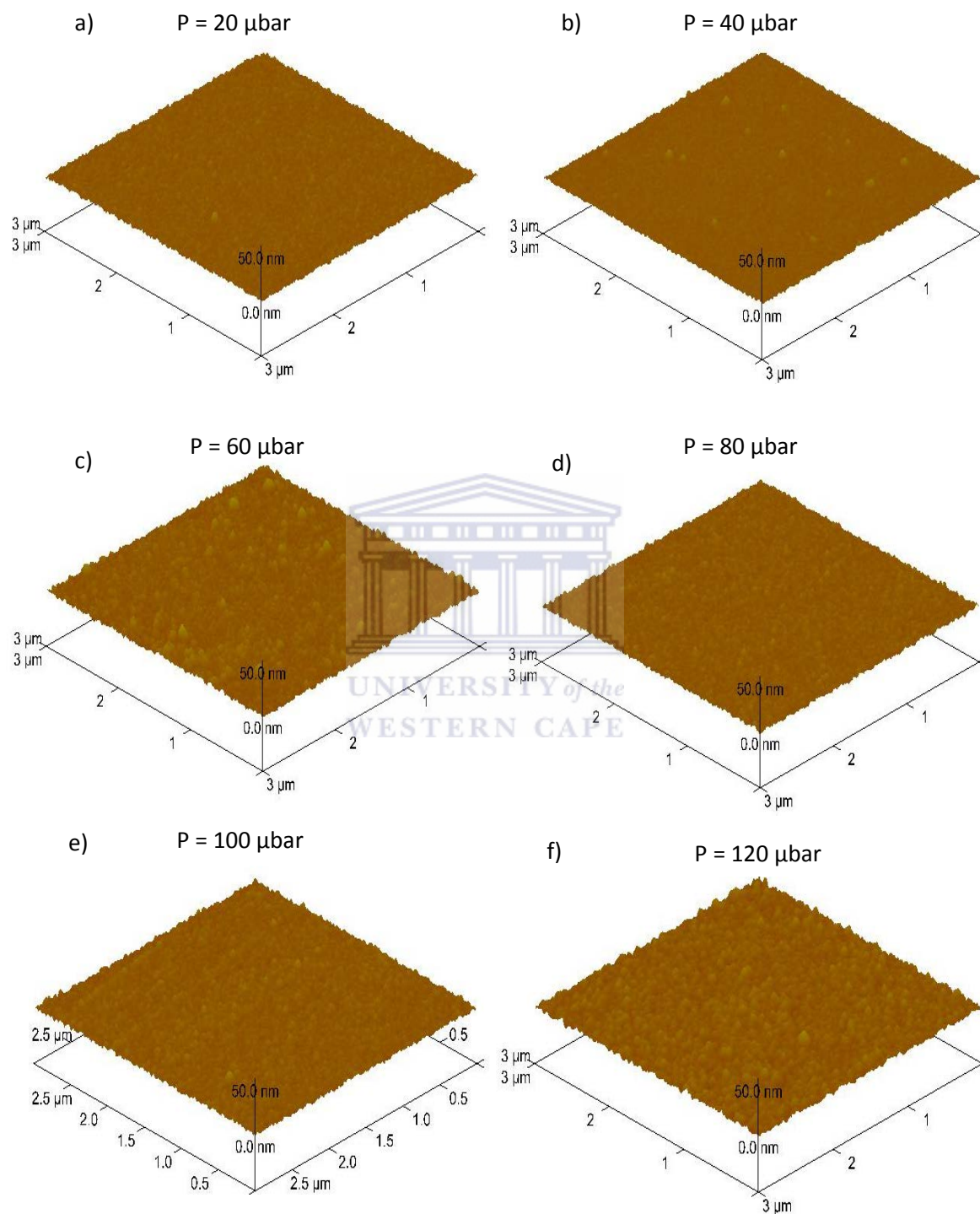


**Figure 3.6:** AFM images for increasing H<sub>2</sub> flow rate in order of increasing H<sub>2</sub> dilution.

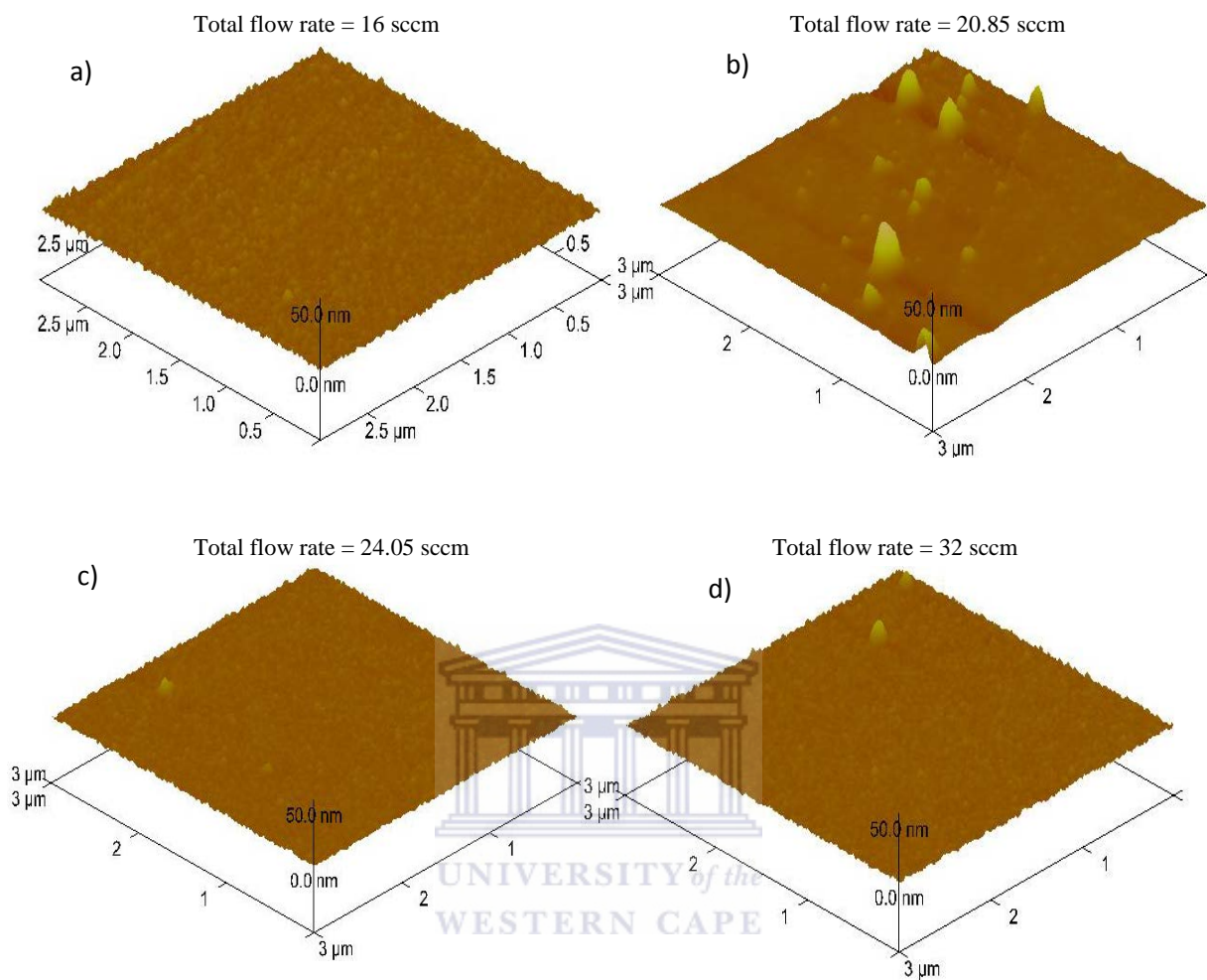
The effect of pressure on the surface morphology can be seen in figure 3.7, where the pressure is increased from 20 - 120  $\mu$ bar. As the pressure is increased the a-SiN:H thin films become thicker, as shown in figure 3.3. Since the thickness of the sample increases considerably with pressure, the elevated roughness can thus be attributed to the increase in thickness. The effect of roughness on thickness will be discussed in some detail for figure 3.9.

Figure 3.8 shows the AFM images of samples prepared by increasing the total flow rate and illustrates that as the total flow rate is increased the film tends to become smoother. Since the variation of the thickness for this series is  $\sim$ 30 nm and thicknesses are well below 300 nm, the effect of thickness variation on roughness can be negated. The increased smoothness with total flow rate is speculated to be as a result of an elevated N content since higher N is associated with denser, smoother a-SiN:H thin films [3.20]. This is a clear indicator that nitrogen incorporation can be the dominating influence on the surface morphology.





**Figure 3.7:** AFM images for pressure series in order of increasing pressure.



**Figure 3.8:** AFM images for total flow rate series in order of increasing total flow rate.

The thickness plays a pivotal role in the surface morphology of the film, and herewith the effect of film thickness on the roughness is displayed in figure 3.9. As shown with the 3D AFM images, the morphology was dominated by both the chamber chemistry and the thickness of the films. The roughness evolution with thickness will now be discussed.

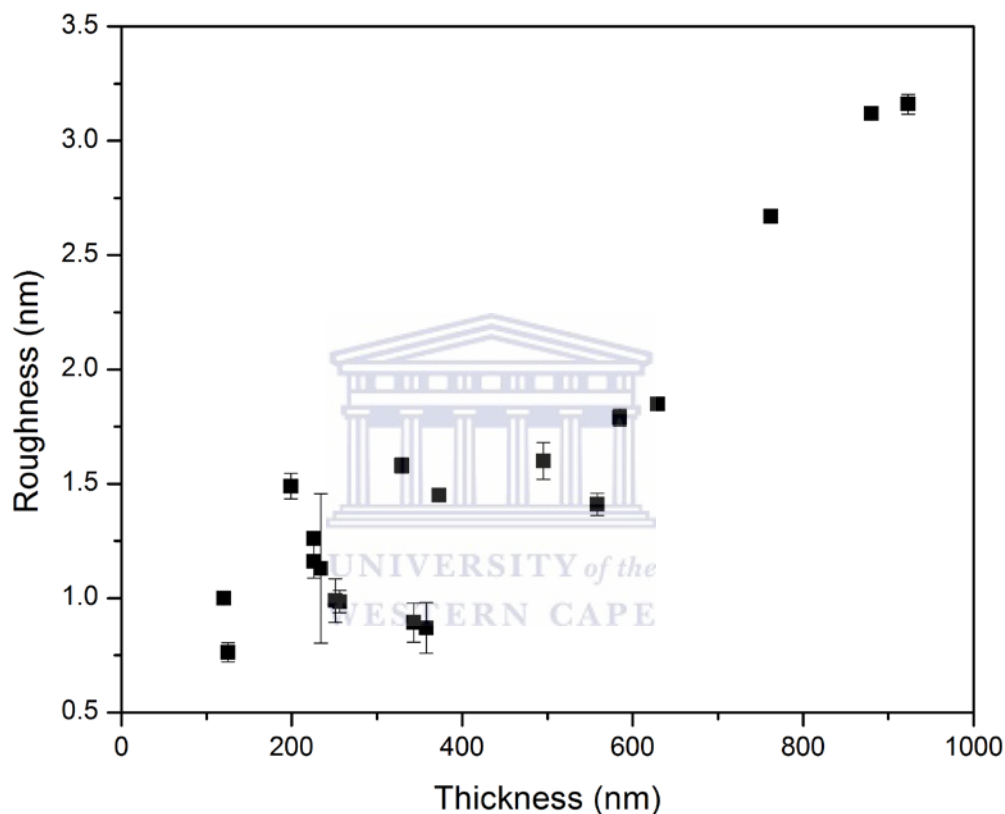


**Figure 3.9:** Roughness evolution with film thickness.

When considering the chamber reaction mechanism and deposition rate; the process can be separated into 3 parts namely; decomposition at the filament, secondary gas phase reactions and adhesion to the substrate surface. The final stage can again be divided into two stages; namely shadowing and surface diffusion [3.30 – 3.32]. When diffusion dominates the deposition process, the film forming species tend to diffuse on the substrate surface and result in smooth, dense films. This surface diffusion is more dominant when species have sufficient kinetic energy

(elevated substrate temperatures) and when less sticky species such as disilene is dominant at the substrate surface. When the growth is dominated by shadowing, the films tend to rapidly become rougher as the film becomes thicker. This process usually dominates under low diffusion conditions and results in columnar structures. The presence of columnar structures under these low diffusion conditions results in shadowing of valleys and thus instabilities in the growing film.

In a model presented by Bales *et al.* [3.32] for films grown by sputtering, the two growth mechanisms are proposed to compete. In the initial growth phase (below 300 nm) the film was found to be dominated by surface diffusion and then later by shadowing. This was also observed by Xu *et al.* for radio frequency magnetron sputtering [3.33]. This result can also be observed in the case of this study. The result shows that at thicknesses below 350 nm the roughness distribution tends to be erratic and non-linear. This is an indication of the surface diffusion mechanism being dominant at these thickness values. As the thickness increases above 350 nm the roughness distribution becomes linear and increases considerably as the thickness increases. This now can be attributed to the dominance of the shadowing coming into effect at these higher thicknesses. The correlation between the present study and Xu *et al* [3.33] is indicative of the film growth (at the substrate) having little dependence on the deposition method.

### 3.4 COMPOSITIONAL PROPERTIES

Depth profiling is a powerful technique as it provides a means of elemental quantification throughout the film depth. The level of oxidation in the bulk can also be investigated by depth profiling, which gives insight to the material applicability as barrier diffusion coatings. It has been shown by X-ray photoelectron spectroscopy (XPS) depth profiling that a-SiN:H thin films tend to be resistant to oxidation in the bulk and oxidation occurs at the film-substrate interface [3.34]. HWCVD a-SiN:H thin films have been shown to have uniform stoichiometric composition in the bulk and depth profiling by sputtering indicated that oxygen had the tendency to be incorporated as silicon oxynitride [3.35].

Literature investigating the depth profiles of a-SiN:H by ToF-HIERD tends to be scant, despite the absolute nature of the technique. The growth process and post deposition processes, such as surface and bulk oxidation, can be investigated by ToF-HIERD [3.36]. In this work the effect of different deposition parameters, such as NH<sub>3</sub> flow rate, H<sub>2</sub> flow rate, total flow rate and pressure, on the film compositional uniformity and resistance to oxidation will be investigated.

Figure 3.10 shows the extracted concentration profiles of the deposited a-SiN:H thin films for series 1. The nitrogen content is observed to increase as the NH<sub>3</sub> flow rate is increase. These films show surface oxidation with an absence of oxidation in the bulk. This is indicative of the sample having oxidised after removal from the HWCVD chamber. At the surface it is clear that Si-O and Si-OH bonds are present since the silicon-oxygen ratio is 1, Si-O-Si bonds appear further into the surface layer as observed by the decreased silicon-oxygen ratio. Oxidation occurs

at the expense of less thermodynamically stable N-H bonds [3.37]. Since these films show no oxidation in the bulk it is expected that these films exhibit an increased presence of Si-H bonds in the bulk. This result is supported by Stannowski *et al* [3.25] where oxygen content is observed to increase as the N-H bond density increases.

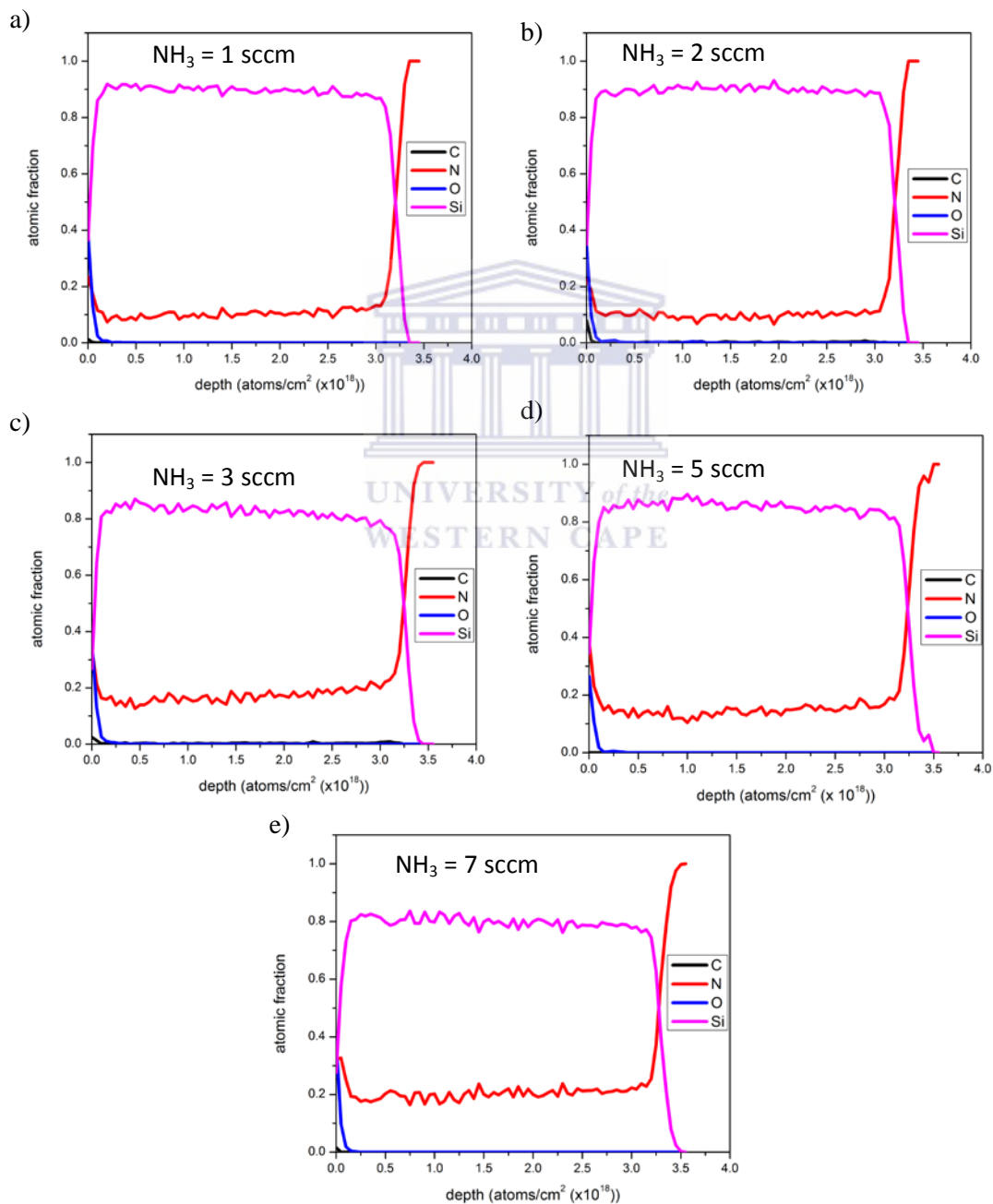


**Figure 3.10:** TOF-HIERD depth profile for samples in order of increasing  $\text{NH}_3$  flow rate.

Figure 3.11 elucidates the effect of H<sub>2</sub> flow rate on the structural uniformity of the a-SiN:H thin films prepared. This figure shows the films to be uniform throughout. The oxidation levels have increased at the surface of the films since there is an increased presence of nitrogen, which in turn indicates an increase in N-H bonds. As discussed for figure 3.10 the oxidation effects tend to be prominent in films with high levels of N-H bonds and voids present. These films show minimal oxidation in the bulk, which indicates that these films have a dense, non-porous a-SiN:H network [3.21]. At elevated nitrogen contents (above 0.2 atomic fraction) these films show nitrogen diffusion into the substrate, this could indicate a nitridation effect during or post deposition of the silicon substrate. This layer, known as a Si-Si and Si-N interlayer was also observed by Fakhri *et al* [3.38] where N was also observed to diffuse into the silicon substrate, for PECVD a-SiN:H thin films.

Literature portraying the effect of pressure on the structural uniformity of a-SiN:H remains limited. The pressure effects are pivotal in the uniformity of the films and are illustrated in figure 3.12. The figure shows that at low pressures (below 100  $\mu$ bar) the films tend to have low levels of uniformity, with the appearance of carbon at the substrate interface and in the bulk. This carbon appears in figure 3.12 a, b and e, since this carbon appears at the interface and in the bulk it is possible that chamber contamination occurred [3.39], substrates were not cleaned effectively or post deposition diffusion of C occurred. Since low levels of oxygen appear at the substrate interface for these a-SiN:H films, it is apparent that the HF dip was effectively performed to eradicate any native oxides on the substrate surface.

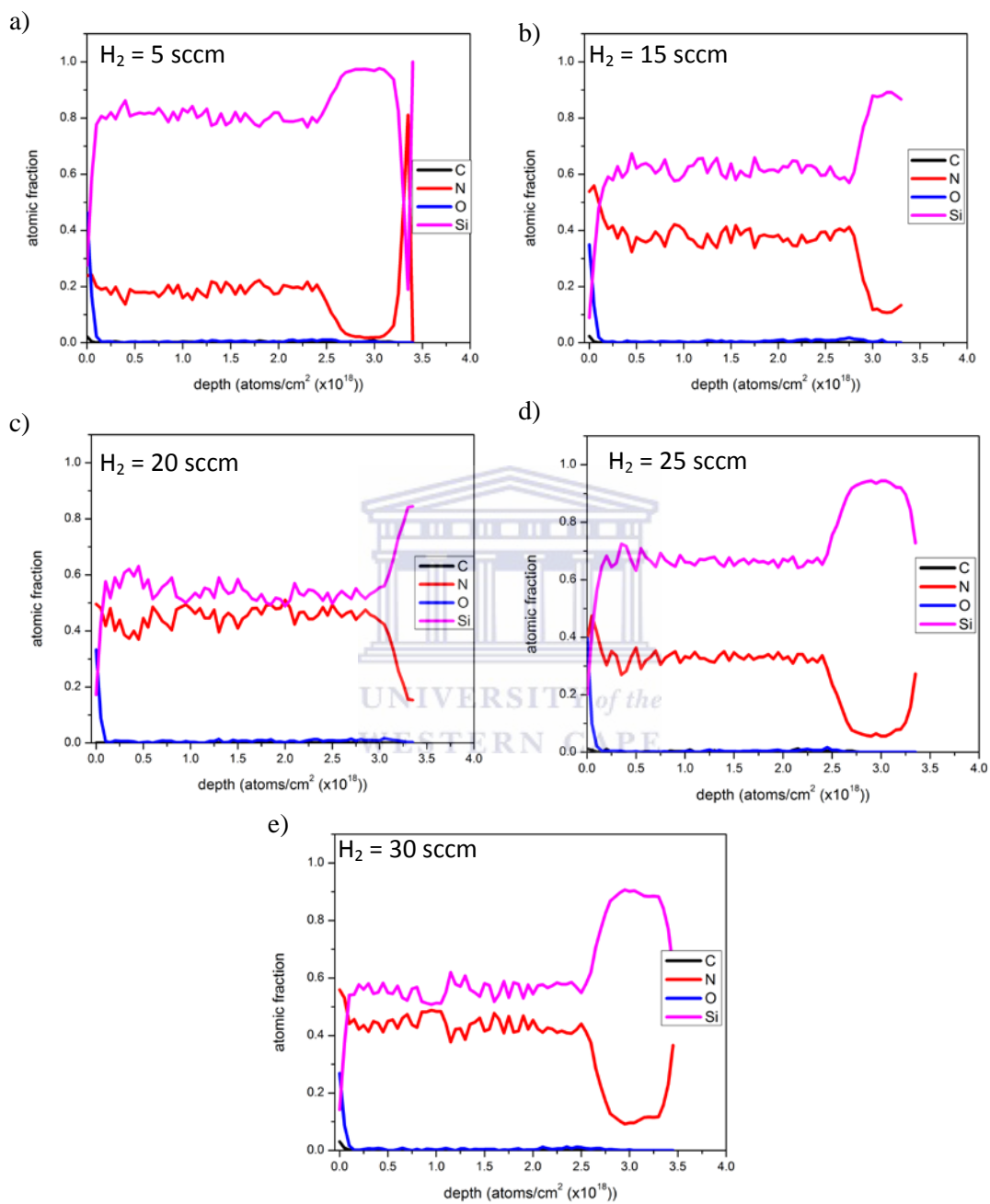


**Figure 3.11:** TOF-HIERD depth profile for samples in order of increasing  $H_2$  flow rate.

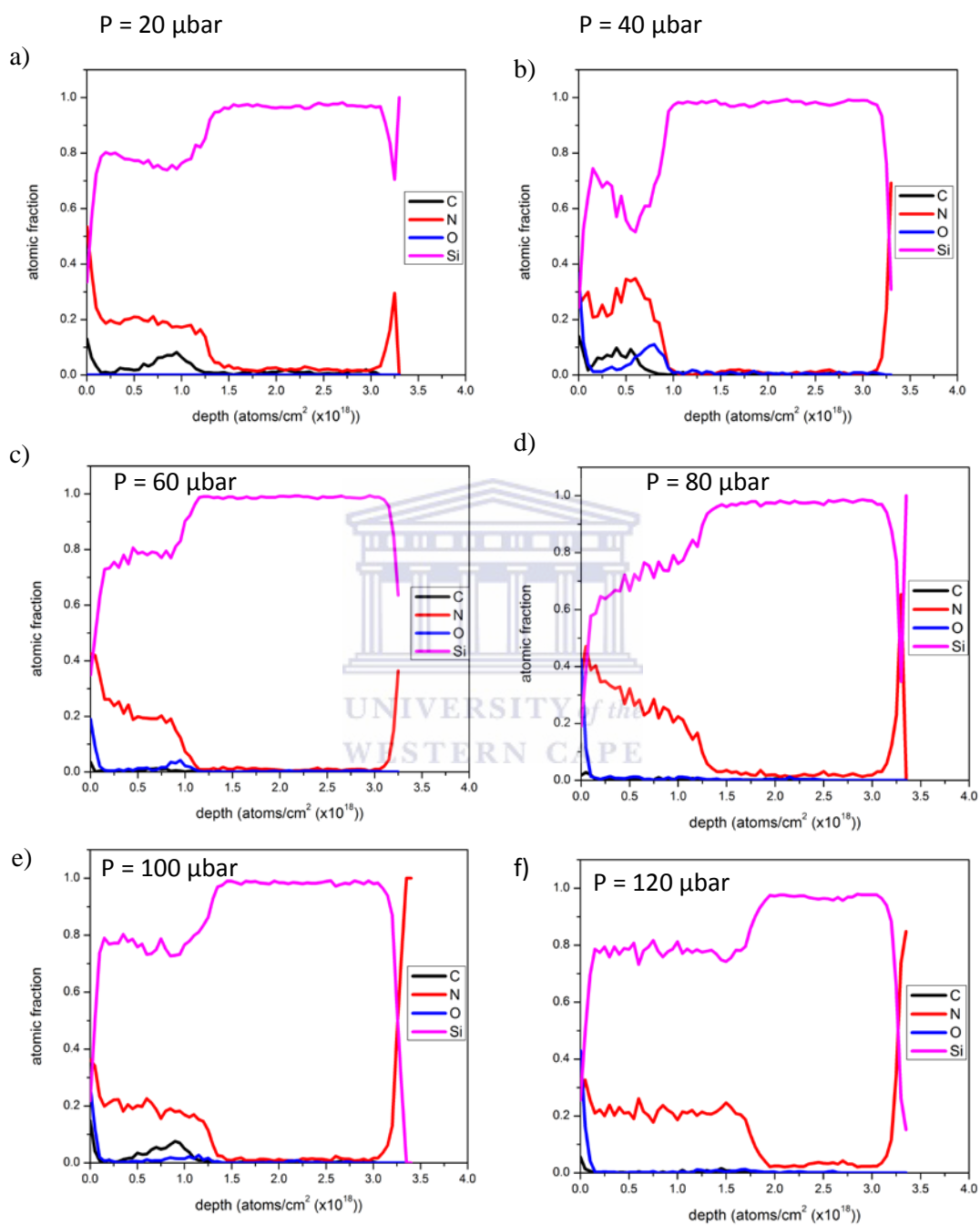
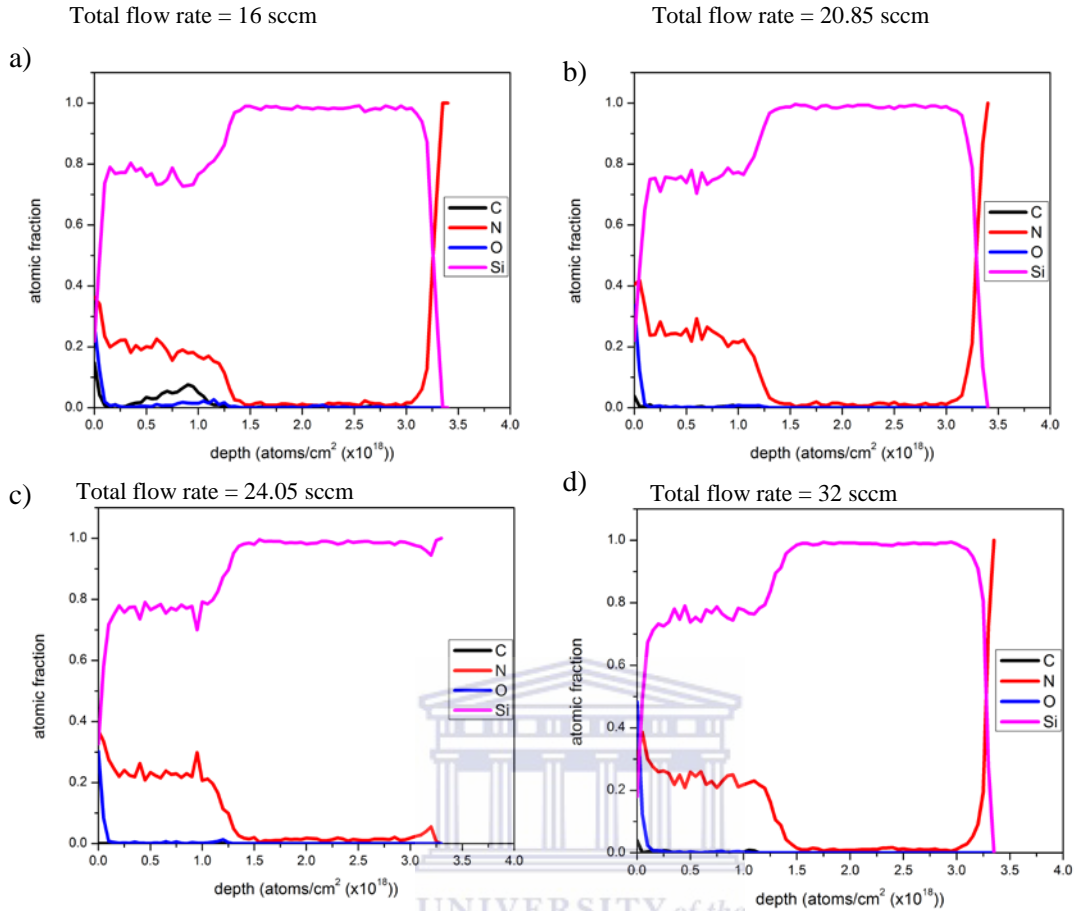


Figure 3.12: TOF-HIERD depth profile for samples in order of increasing chamber pressure



**Figure 3.13:** TOF-HIERD depth profile for samples in order of increasing total flow rate.

The effect of total flow rate on the depth profile is observed in figure 3.13. At flow rates above 16 sccm the films appear to be uniform with oxygen present only on the surface. These films exhibit low levels of O in the bulk, which means they are low in N-H bonds and dense [3.25]. It is apparent that these films do not exhibit an interlayer as for the series prepared by varying the hydrogen content, which is expected since these films have low N content.

The N/Si ratio is the main contributing factor to the tunability of a-SiN:H thin films. The N/Si determines the application of the a-SiN:H thin film, which includes, active components in thin film transistors [3.40], gate dielectrics in thin film transistors [3.41] and antireflective and

passivation coatings in solar cells [3.42 - 3.43]. The N/Si ratio was determined using the bulk depth profiles shown in figure 3.10 – 3.13, with the standard deviation being an indication of the N/Si uniformity in the bulk. For the purpose of this study, the N/Si of the a-SiN:H thin films will be investigated for the purpose of passivation and anti-reflective coatings. The effect of NH<sub>3</sub> flow rate, H<sub>2</sub> flow rate, deposition pressure and total flow rate on the N/Si ratio was investigated. The influence of NH<sub>3</sub> gas flow rate is illustrated in figure 3.14 and the N content is observed to intensify as the NH<sub>3</sub> flow rate increases. When considering variation in NH<sub>3</sub> flow rate; the result can be explained as the increased presence of ammonia results in an increased presence of nitrogen containing radicals, such as Si(NH<sub>2</sub>)<sub>4</sub>. These aminosilanes are the species responsible for the incorporation of N into the a-SiN:H thin films. Since NH<sub>3</sub> is mainly dissociated by secondary gas phase reactions from the decomposition of SiH<sub>4</sub> [3.25], the increased presence of NH<sub>3</sub> enhances these secondary gas phase reactions, which in turn enhances the aminosilanes presence and thus results in an increased N incorporation. The relationship shown in figure 3.14 was also observed by Romijin *et al* [3.29]. The figure illustrates that these a-SiN:H films are in the silicon-rich regime, where silicon is the dominant species in the amorphous matrix.

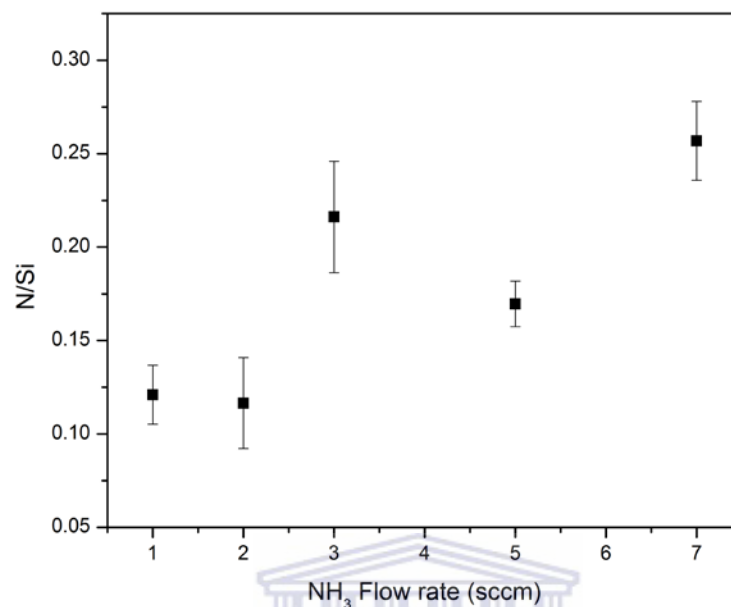


**Figure 3.14:** Effect of NH<sub>3</sub> flow rate on the nitrogen content in the deposited a-SiN:H thin films from ToF-HIERD.

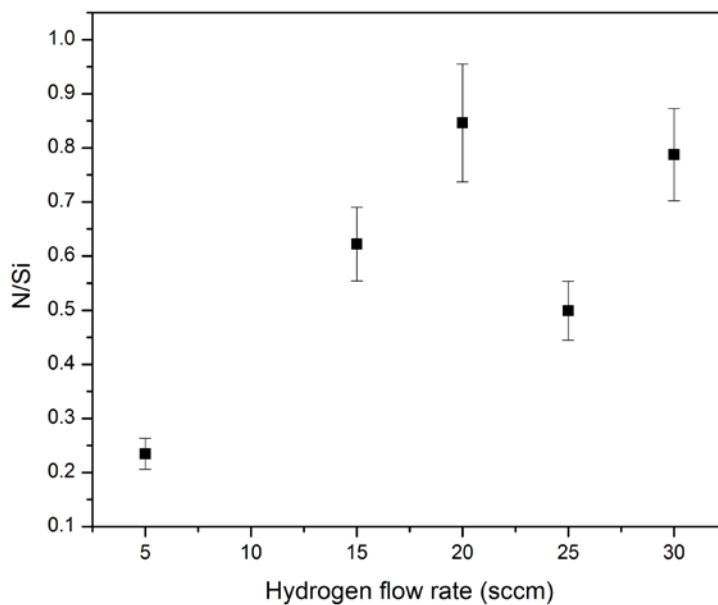


**Figure 3.15:** Effect of H<sub>2</sub> flow rate on the nitrogen content in the deposited a-SiN:H thin films from ToF-HIERD.

The H<sub>2</sub> dilution effects are observed in figure 3.15, where it can be seen that H<sub>2</sub> dilution has a positive effect on the incorporation of N into the a-SiN:H thin films. The upsurge in N integration can be explained by considering the reaction mechanism. Efficient dissociation of NH<sub>3</sub> is the foremost contributing factor in the incorporation of N into the film. As previously discussed NH<sub>3</sub> is mainly dissociated in the gas phase by atomic hydrogen. The addition of H<sub>2</sub> to the chamber has an etching effect at the filament, freeing up silicide contaminated active sites to allow for more efficient dissociation of SiH<sub>4</sub> [3.23], which in turn leads to more efficient dissociation of NH<sub>3</sub>. The results obtained in figure 3.15 are in agreement with results obtained by Mahan *et al* [3.22]

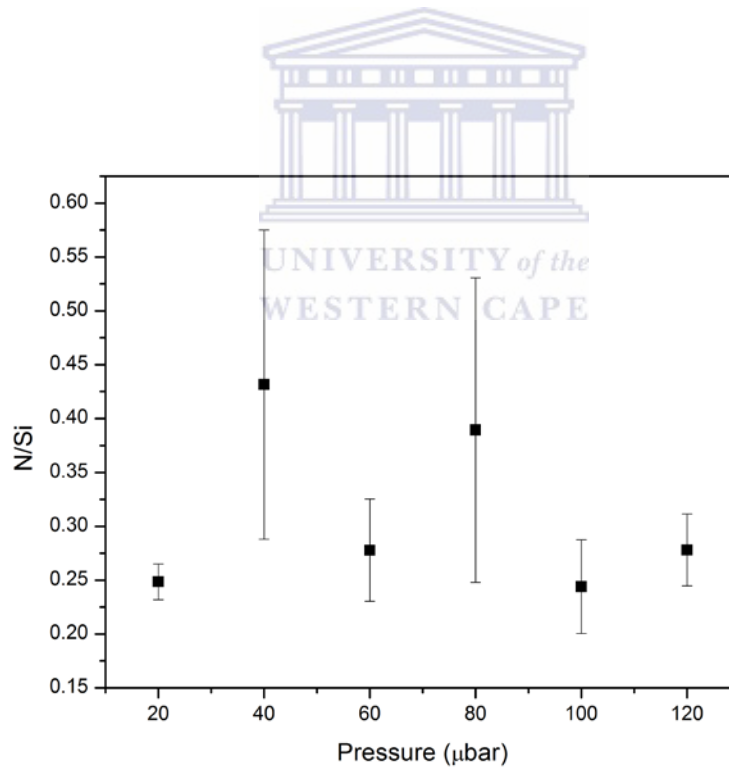


**Figure 3.16:** Effect of pressure on the nitrogen content in the deposited a-SiN:H thin films from ToF-HIERD.

The N/Si dependence on pressure is shown in figure 3.16, where there is no discernible dependence on pressure, as the values are within error of each other. At a pressure of 80 and 40  $\mu\text{bar}$  the error bars are excessively large, this can be attributed to the films being non-uniform, which can be seen in figure 3.12 b and d. In the case of this experiment, the  $\text{NH}_3/\text{SiH}_4$  flow ratio was low at 1.4. Since the gas flow rate was kept constant, the radical ratios in the chamber were constant also. In the event of an increase in pressure the rate of reaction of the desorbed radicals now surges, as the mean free path now decreases. This means that the ratio of N incorporation is minimally dependant on the pressure. However, an increase in pressure results in increased deposition rate as in figure 3.3, which is indicative of the amplified chamber reactions of the film forming species. As the film forming species are increased, so too are the secondary gas phase reactions, this results in thicker films with a consistent nitrogen incorporation. The result shown in figure 3.16 is in agreement with observations made by Stannowski *et al* [3.25]. This result however is dissimilar to what was observed by Verlaan *et al* [3.44], where the N/Si ratio increased considerably with pressure. The discrepancy can be attributed to the differences in flow ratios, as in the work performed by Verlaan *et al*, flow ratios were above 13.

Literature surveying the effect of total flow rate, to our knowledge, is non-existent in HWCVD a-SiN:H. Figure 3.17 illuminates the effect of total flow rate on the N/Si ratio, where it can be seen that the N/Si ratio increases as the total flow rate increases. The amplified N incorporation must indicate an increased dissociation of  $\text{NH}_3$  at elevated total flow rates. The increase in deposition rate observed in figure 3.4 indicates increased dissociation of  $\text{SiH}_4$ , which in turn indicates amplified  $\text{NH}_3$  dissociation and hence an increased N incorporation. At elevated total flow rate there is an increase in the chamber gas replenishment, which means that increased amounts of source gas is now present for reaction and formation of a-SiN:H film.

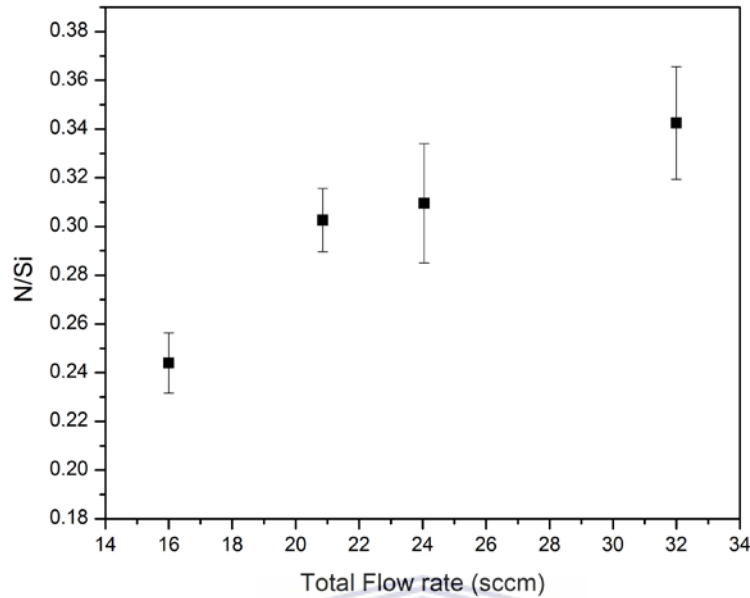


**Figure 3.17:** Effect of Total flow rate on the nitrogen content in the deposited a-SiN:H thin films from ToF-HIERD.

The verification of results across techniques becomes important to increase confidence levels in results obtained. In this section the EDS technique will be compared to the ToF-HIERD for analysis of N content in a-SiN:H thin films. EDS is a valuable technique for analysis of a-SiN:H thin films as it provides a cheap, non-destructive means of quantifying the N/Si ratio present in the film and the technique requires little to no sample preparation for measurement.

A plot of N/Si determined from EDS vs. N/Si determined by ToF-HIERD is indicated in figure 3.18, where a clear linear relation is observed between the techniques. The linearity shows that the N/Si ratios from each technique corroborate well. The circled area on the plot indicates a region of deviation, where the EDS N/Si ratio is depressed. This discrepancy was attributed to

film thickness, as this was prominent in films having low thickness values. This prompts investigation into the penetration depth of the 6 kV electron beam used for EDS analysis.

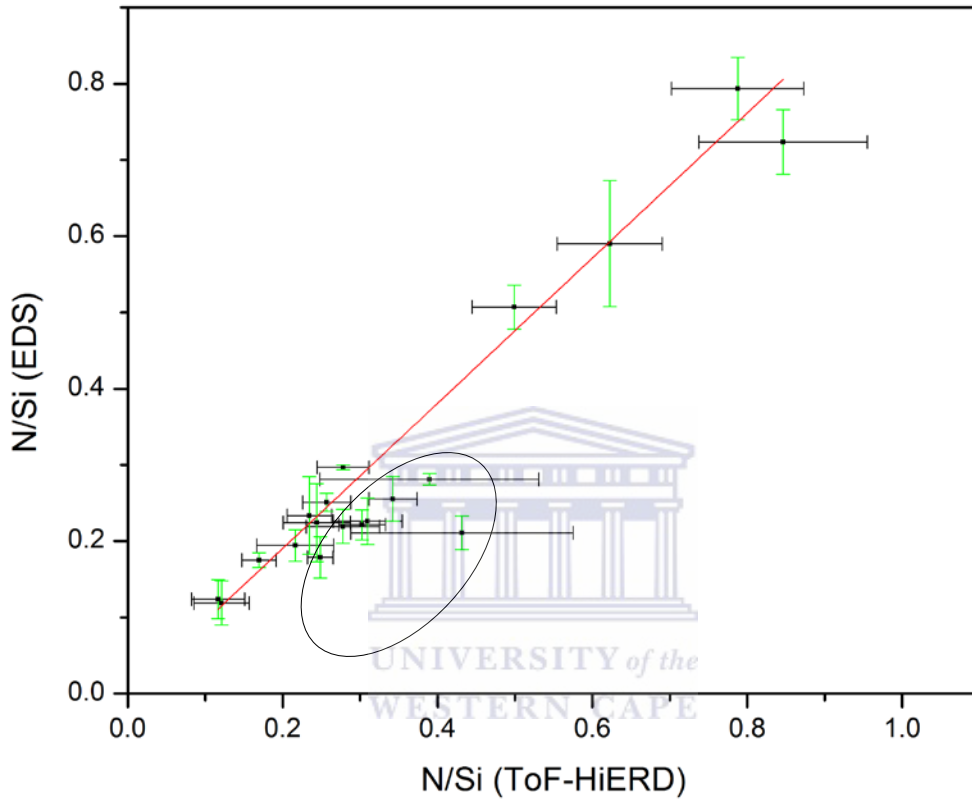


**Figure 3.18:** N/Si from EDS vs. N/Si from ToF-HiERD

The electron accelerating voltage used in the SEM where EDS was performed was 6 kV. A Monte Carlo simulation of the electron beam path in an a-SiN:H thin film with thickness 120 nm is shown in figure 3.19 [3.45]. The simulation shown in figure 3.19 indicates that the beam penetrates into the silicon substrate with total depth in the region of ~360 nm. This image clearly shows that the depressed N/Si ratios observed for EDS measurements can be attributed to the inability of the EDS technique to resolve the a-SiN:H thin film from the c-Si substrate. This

shows that EDS can be used as a cheaper, more accessible means of N/Si ratio determination, as opposed to ToF-HIERD.

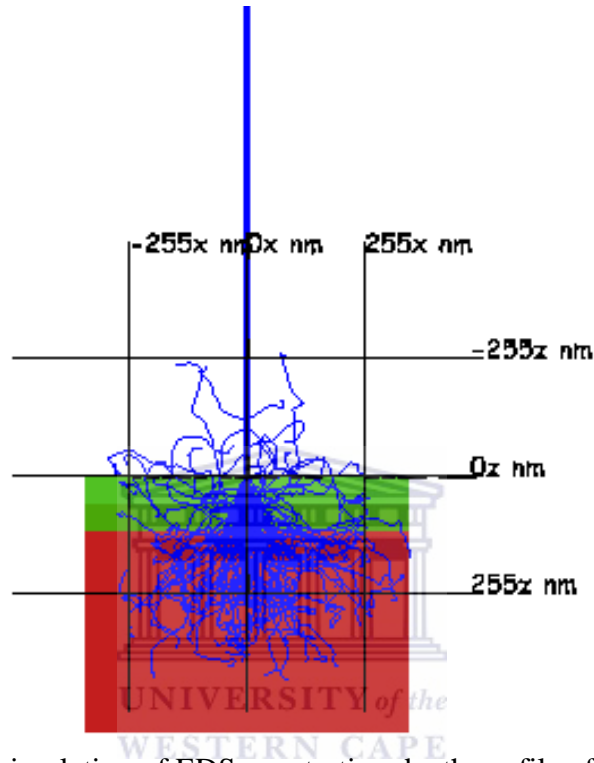


**Figure 3.19:** Monte Carlo simulation of EDS penetration depth profile of 120 nm sample from pressure series prepared at 20  $\mu$ bar [3.45].

The hydrogen content present in a-SiN:H allows for the passivation property of the material. This comes as a result of the high levels of H present in the film, reaching values greater than 20% [3.46]. Upon annealing hydrogen is released and passivation of defects is induced in silicon solar cells by the a-SiN:H layer [3.2]. In this section the effect of nitrogen incorporation on the hydrogen content of the prepared films will be investigated. Elastic recoil detection analysis (ERDA) was the technique of choice for total hydrogen quantification, since it eliminates the need for proportionality constants and is a totally independent technique.

The fitted ERDA spectra, in order of increasing N content, of the samples are illustrated in figure 3.20. It is apparent from the spectra displayed in figure 3.20 that there is no observable trend. However, the spectra indicate some loss of hydrogen at the surface and substrate, which is apparent from the lack of H at the film surface and H tailing into the substrate, respectively. Thicker films such as figure 3.20 b, c, d, e, h, p, q and r showed uniformity of H in the bulk, with H loss at the surface and interface, whereas thin films showed limited [H] uniformity with H content increasing to a maximum then decreasing in the same manner. The lack of H at the surface can be explained by the high levels of oxygen at the surface as shown in the ToF-HIERD depth profiles (figure 3.10 – 3.13). Hydrogen bonded as Si - H and N - H results in these bonds being broken for the formation of more stable SiO<sub>2</sub> bonds [3.25]. N-H bonds are associated with a more porous layer and since these films show no oxidation in the bulk, it can be assumed that these films contain H bonded mainly as Si - H [3.25]. The spectra in figure 3.20 also indicate H loss into the substrate, which stems from the passivation property of the material where H is released and passivates the underlying a-Si:H active layer dangling bonds.

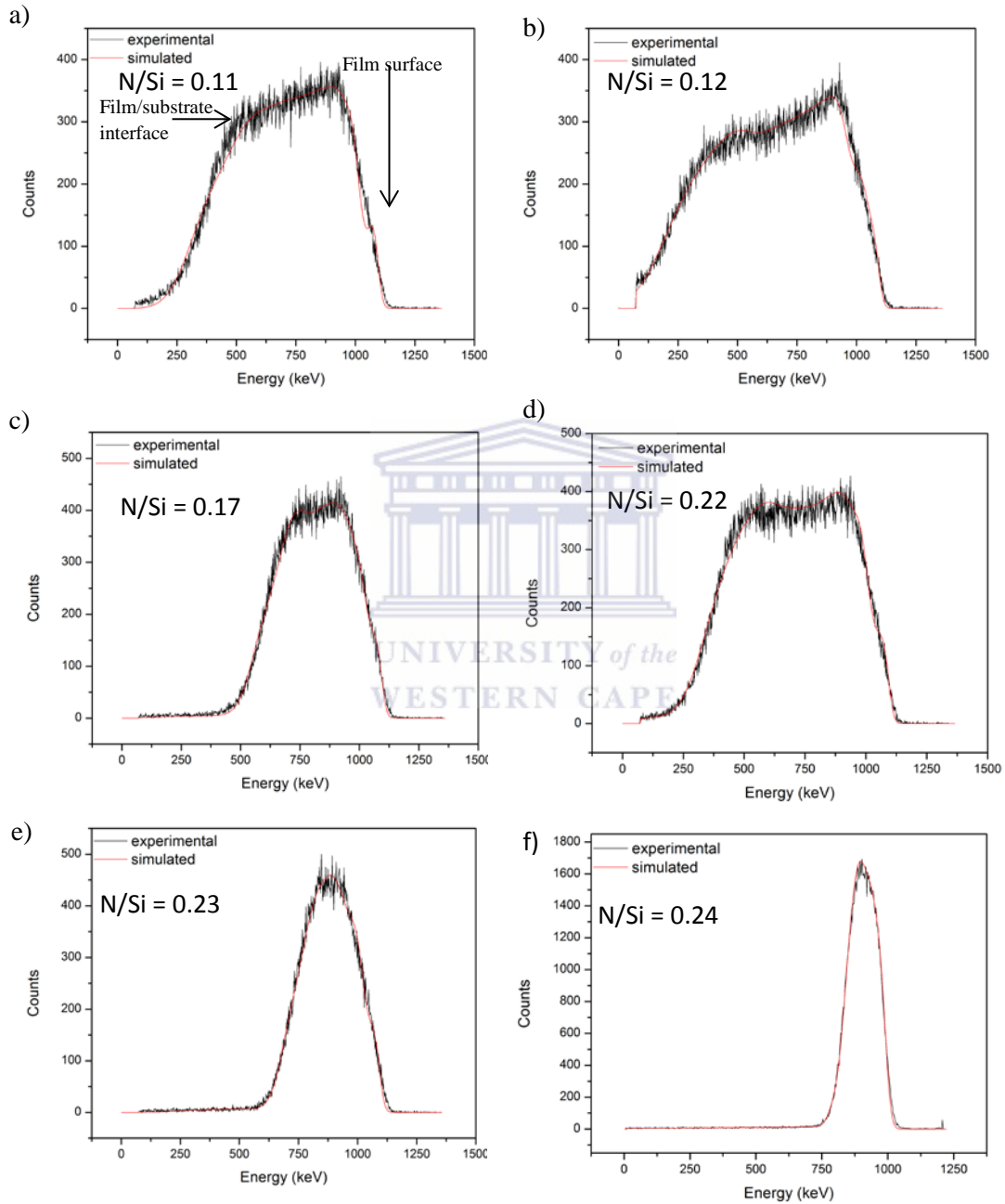


Figure 3.20: ERDA spectra of samples in order of increasing N content.

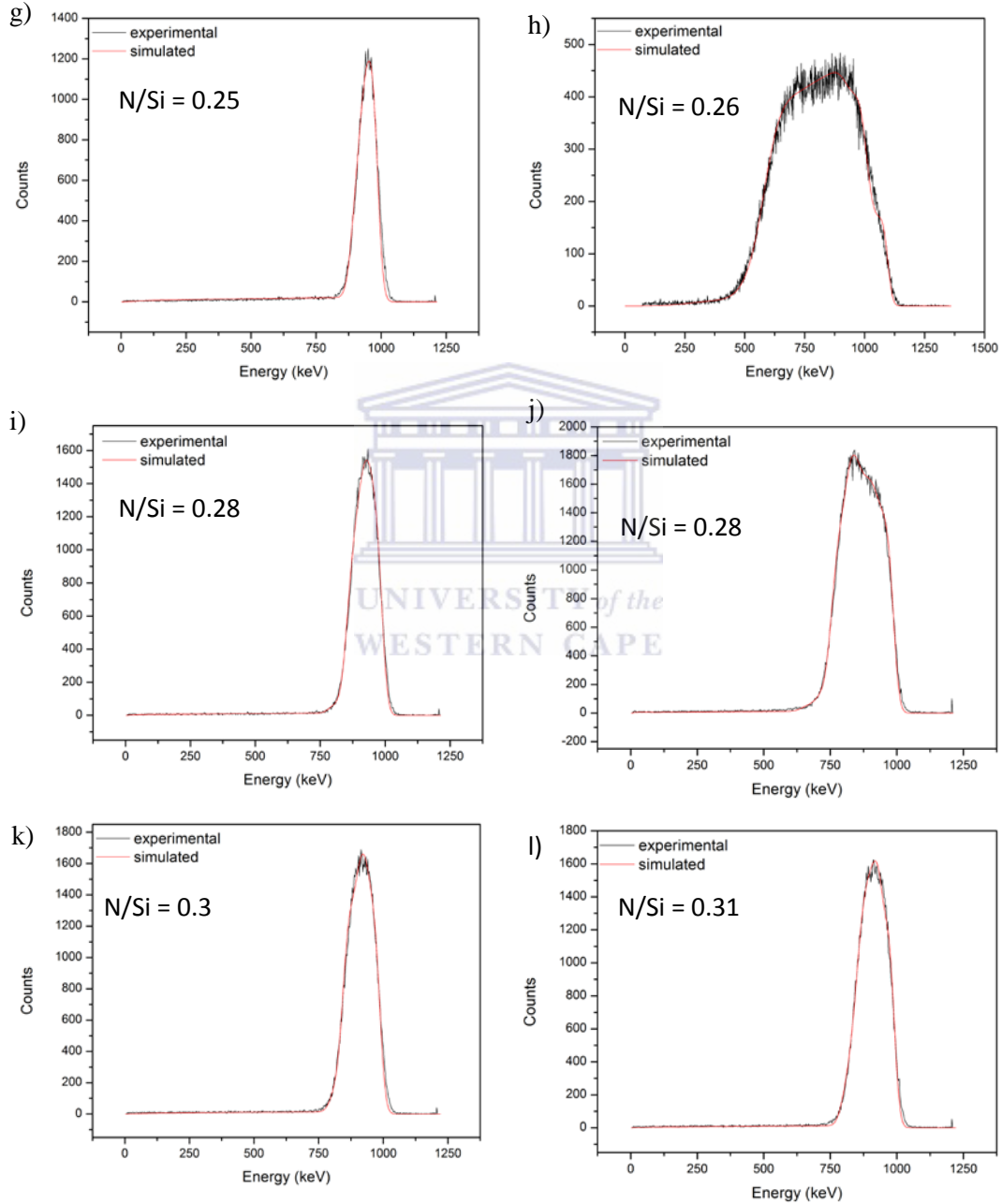


Figure 3.20: ERDA spectra of samples in order of increasing N content.

## RESULTS AND DISCUSSION

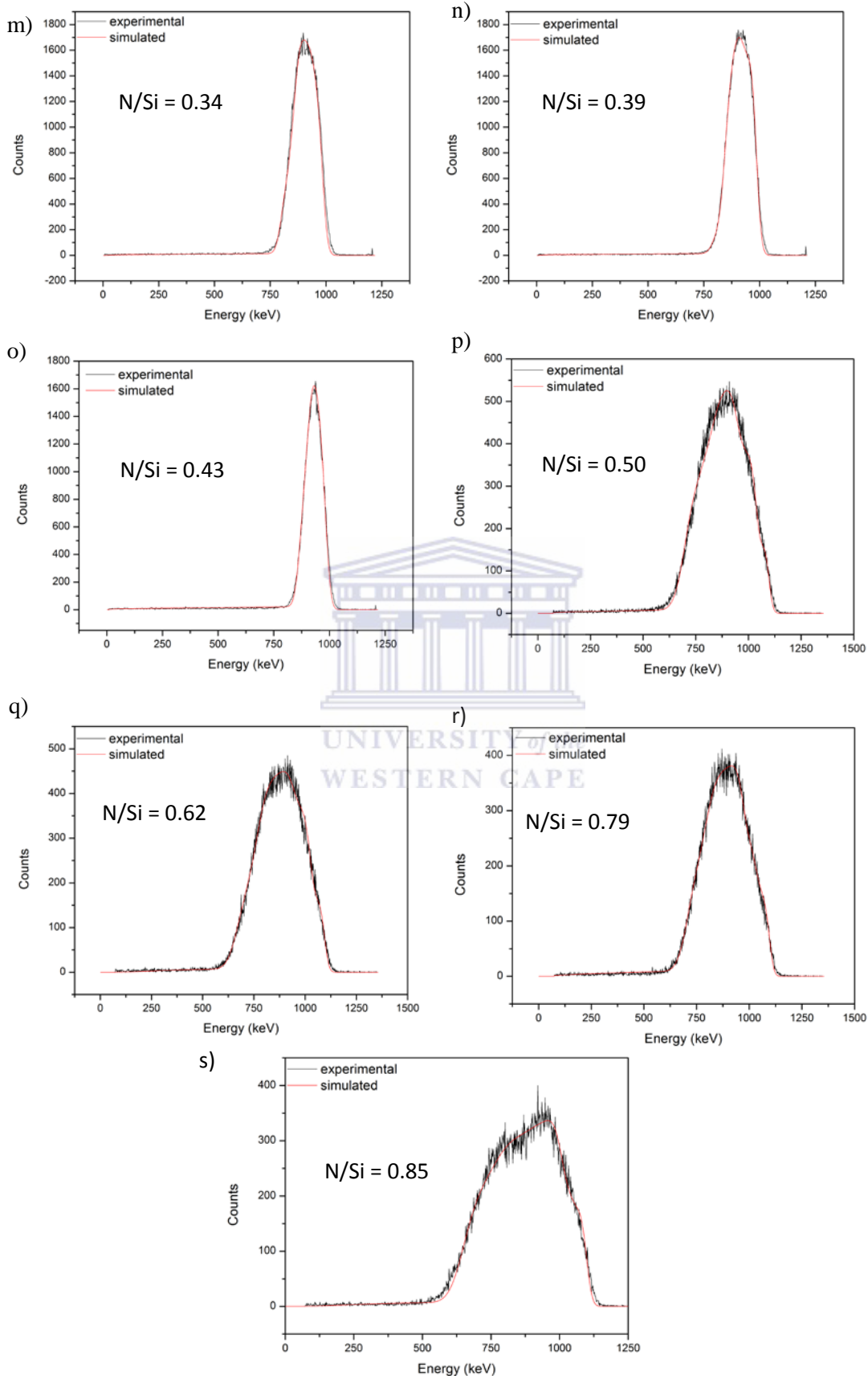
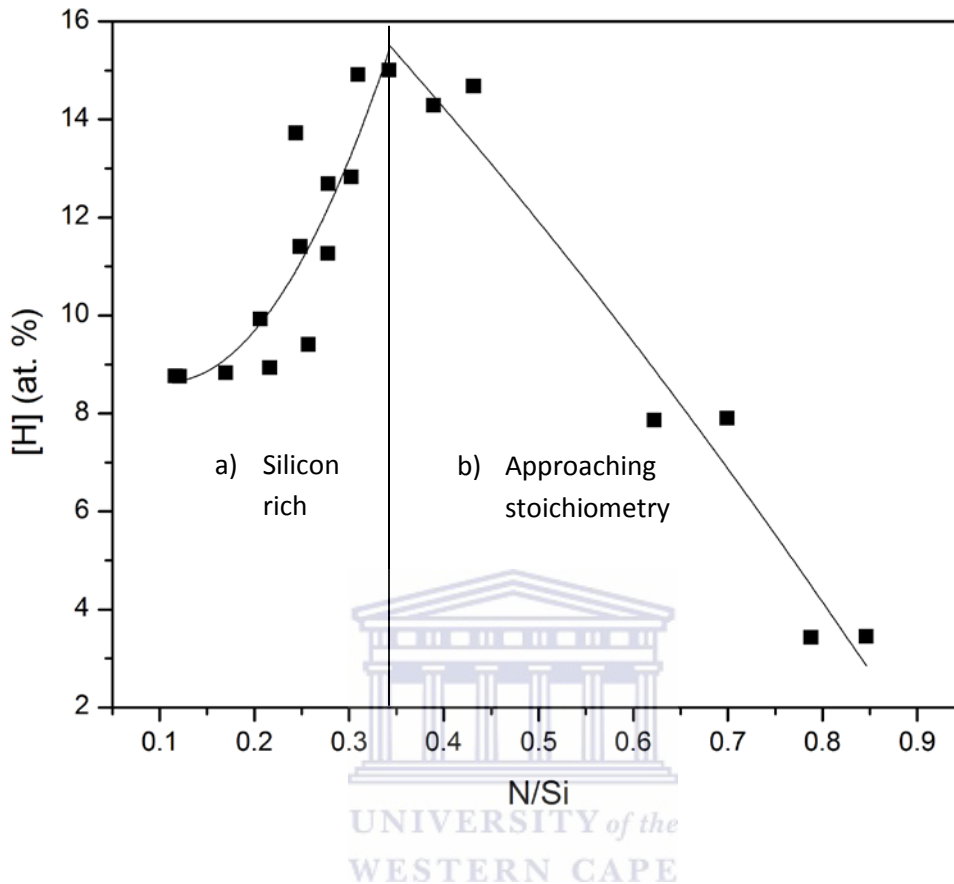


Figure 3.20: ERDA spectra of samples in order of increasing N content.



**Figure 3.21:** H content vs. N/Si ratio for all prepared samples.

The hydrogen content as a function of nitrogen incorporation can be viewed in figure 3.21. In this section new insight into the dependence of H content on the N/Si ratio will be presented. This comes as a result of the scant nature of literature investigating H contents at low nitrogen incorporation (below N/Si ~0.25).

Silicon nitride thin films with the lowest H content appear at stoichiometry, which is around 9 at.% according to Verlaan *et al* [3.44]. The graph in figure 3.21 shows that the films prepared have a suppressed H content reaching a minimum around 3 at.% for N/Si ratio of ~0.8. The

reduced H content seems to be unique to low flow rates as similar low H content films were attained by Lui *et al* [3.24] in the region with low N content.

It can thus be seen, from this graph that the H content as a function of N/Si ratio, tends to be complex can be divided into three regimes namely; a) silicon rich, b) approaching stoichiometry and c) nitrogen rich. The result shown in figure 3.21 clearly shows that for the current study we are working in regimes (a) and (b) and thus regime (c) is not indicated, but is commonly shown in literature [3.47]. In the silicon rich regime there is an increase in H content as the N content elevates, reaching a maximum at N/Si ratio of  $\sim 0.35$ . The H in the silicon rich region is mainly incorporated as SiH with a minimal amount of H being bonded to N; this can be seen from the films low oxygen presence in the bulk and will be discussed in detail with FTIR [3.25]. The region approaching stoichiometry shows a suppression of relative H content as the N incorporation increases, reaching a minimum for the film with N/Si ratio of  $\sim 0.8$ . In this regime the [H] will decrease and reach a minimum around stoichiometric N/Si [3.44]. In the N rich region the H content will increase again and the increased H content will be incorporated mainly as N-H and these films are shown to be porous and prone to oxidation, as a result of the low binding energy of the N-H bond [3.20]. The H incorporation is shown to have an inverse proportionality to the film density [3.48] and thus it can be assumed that the films that have very low H content ( $\sim 3$  at.%) are dense and suitable for permeation barrier applications.

The ease of measurement allows for FTIR to be commonly used in the analysis of bonding arrangements and quantities for a-SiN:H thin films. There is however certain controversy surrounding the proportionality constants used for quantification, as these are highly dependent on the composition of the a-SiN:H thin film [3.49]. As a result of this controversy, we have

chosen to represent trends in Si-N and total H bond quantification by means of the integrated absorbance of the fitted FTIR peaks. For the purpose of this study we will focus only on the Si-N asymmetric stretching vibration located at  $\sim 830\text{ cm}^{-1}$ , SiH stretching vibration centred at  $\sim 2100\text{ cm}^{-1}$  and the N-H stretching vibration at  $\sim 3400\text{ cm}^{-1}$  [3.50]. The deposited films show presence of Si-H wagging, N-H bending and Si-O-Si stretching modes at  $640\text{ cm}^{-1}$ ,  $1200\text{ cm}^{-1}$  and  $1100\text{ cm}^{-1}$ , respectively [3.24]. However these peaks were not used for quantification as a result of the high noise levels and errors associated with them for the measured spectra.

The FTIR spectra of a-SiN:H thin films tend to be dominated by the prominent peak around  $600\text{ cm}^{-1}$  -  $1200\text{ cm}^{-1}$ . This can be replicated by performing a Gaussian fit for components at around  $640\text{ cm}^{-1}$ ,  $750\text{ cm}^{-1}$ ,  $830\text{ cm}^{-1}$  and  $940\text{ cm}^{-1}$ . In this section we will consider the  $750\text{ cm}^{-1}$ ,  $830\text{ cm}^{-1}$  and  $940\text{ cm}^{-1}$  peaks for the purpose of quantifying SiN bonds.

The Gaussian fit of the SiN peak at low N/Si ratio (a) and elevated N/Si ratio (b) can be viewed in figure 3.22. Figure 3.22 (a) shows that the peak at  $750\text{ cm}^{-1}$ , which is as a result of isolated SiN bonds with Si as nearest and next nearest neighbour [3.51 – 3.52], wanes at elevated N/Si ratio. This disappearance is trivial, since as N incorporation increases the a-SiN:H matrix becomes more populated with N atoms and hence the probability of finding isolated SiN bonds decreases considerably. This result was also observed by Lin *et al* [3.53] for PECVD a-SiN:H. The disappearance of the  $750\text{ cm}^{-1}$  peak gives rise to a Gaussian peak centred around  $940\text{ cm}^{-1}$  (figure 3.22 b), which arises as a result of  $N_n$ -Si-H bonds that originates from the elevated N replacement of H and Si in the a-SiN:H matrix [3.52].

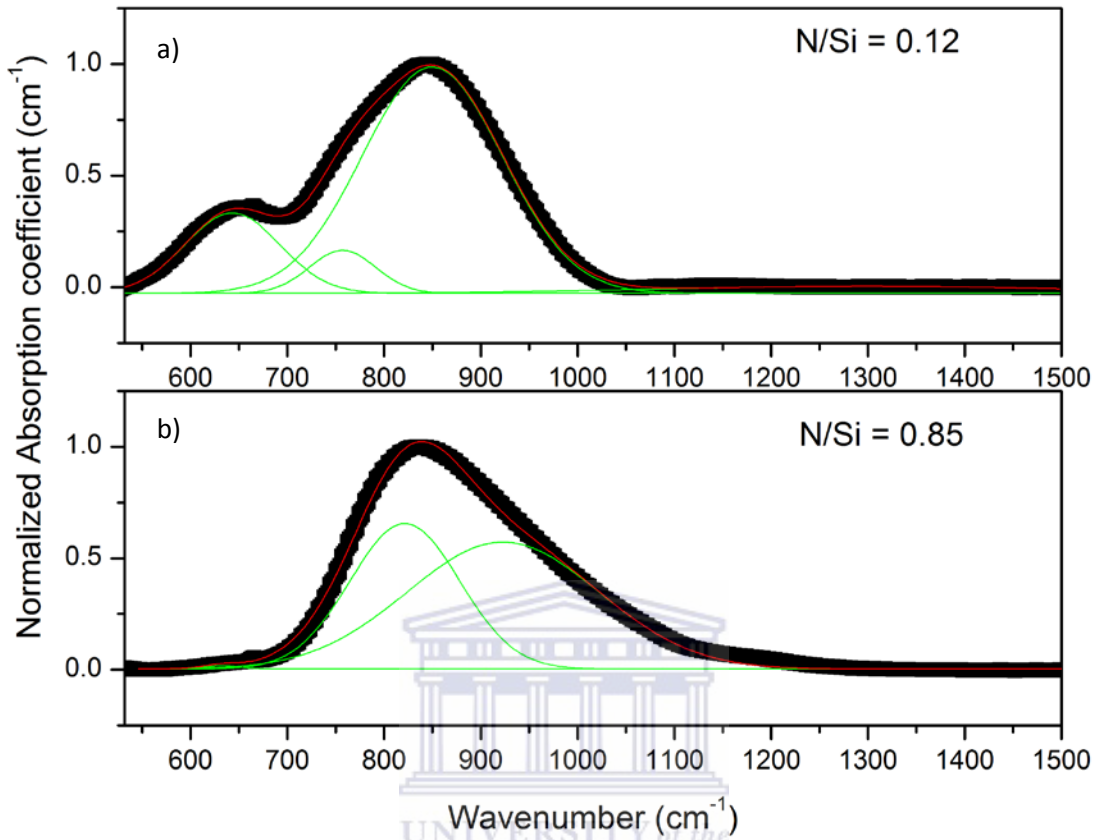


**Figure 3.22:** FTIR spectra indicating the presence of a) the  $750\text{ cm}^{-1}$  and  $830\text{ cm}^{-1}$  peak at low N/Si ratio and b) the  $830\text{ cm}^{-1}$  and  $940\text{ cm}^{-1}$  absorption peaks at elevated N/Si ratios.

The SiN integrated absorption as a function of the N/Si ratio can be viewed in figure 3.23, which again shows the multiphase behaviour observed for the [H] at.% vs. N/Si ratio, inserted in figure 3.23. A distinctive transition phase can be seen at around  $N/Si \approx 0.32$  where there is a shift from the silicon rich regime to the region approaching stoichiometry. This behaviour, to our knowledge, has not been documented as it is common for Si-N integrated absorption to be linearly dependent on N/Si ratio [3.54-3.55]. This linear behaviour is observed in the region approaching stoichiometry. The origin of this multiphase behaviour has been ascribed to the fact that, in the silicon rich regime Si-Si bonds are preferentially incorporated, hence the decrease in

the Si-N bond density. This is also confirmed by the presence of the peak around  $\sim 750\text{ cm}^{-1}$ , at low N/Si ratios, where N is bonded to Si as nearest and next nearest neighbours. The inverse relation between the H content and Si-N integrated absorption shown in figure 3.23, indicates that the incorporation of bonded N atoms comes at the expense of H in the a-SiN:H matrix.

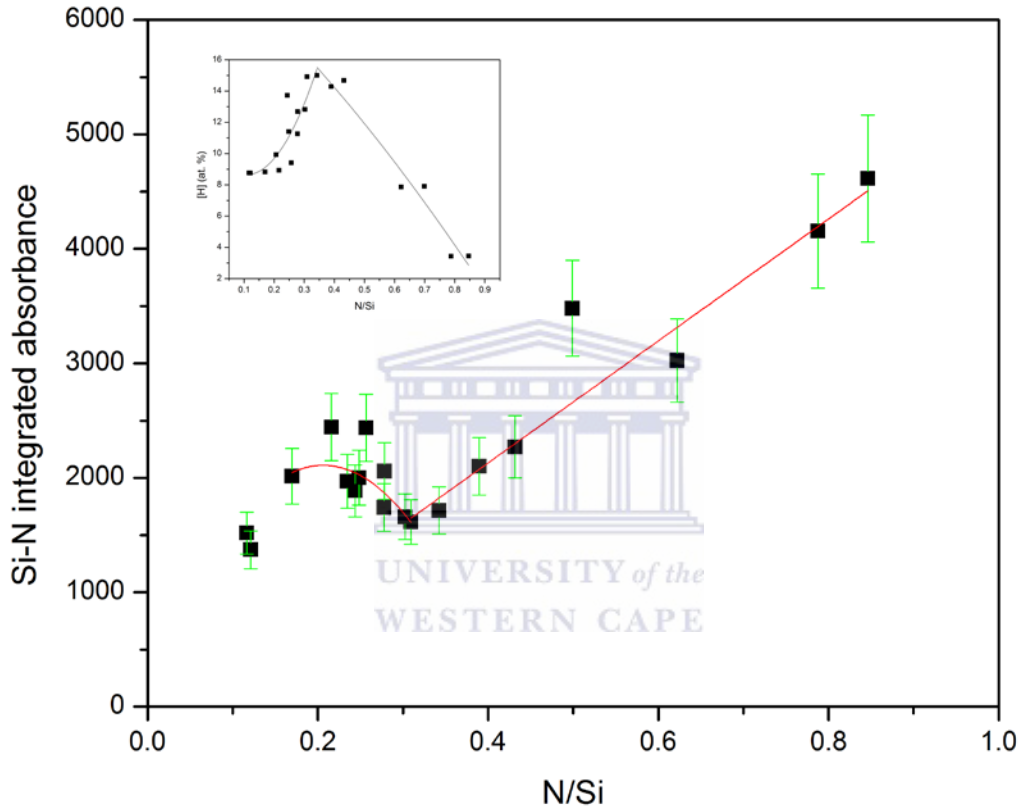


**Figure 3.23:** The dependence of Si-N integrated absorption on the N/Si ratio, with N/Si vs. %H as the insert.

### Si-H and N-H bonding

The incorporation of nitrogen into a-SiN:H thin films has significant effects on the material properties and the case of the Si-H peak position is no different. Figure 3.24 shows the effect of N incorporation on the position of the Si-H stretching absorption peak, where it can be seen that

the peak increases linearly from 2075 cm<sup>-1</sup> for low N content to around 2180 cm<sup>-1</sup> for elevated N content. The increase in wavenumber is attributed to the increased presence of N in the environment surrounding the SiH bond. The electronegativity of an N atom is greater than that of a Si atom and thus results in the blue shift in the SiH stretching peak position [3.22]. This linear relation was also seen by Mäckel and Ludermann *et al* [3.56] for PECVD a-SiN:H thin films. The linear relation in figure 3.24 can be used for determination of the N/Si ratio if the SiH peak position is known from the equation below, where  $\omega$  is the wavenumber;

$$\omega = 135.004 \left( \frac{N}{Si} \right) + 2072 \text{ cm}^{-1} \quad (3.13)$$

This relation was attained by fitting the plot of N/Si vs. SiH peak position as shown in figure 3.24, where  $\omega$  is the Si-H stretching peak position.

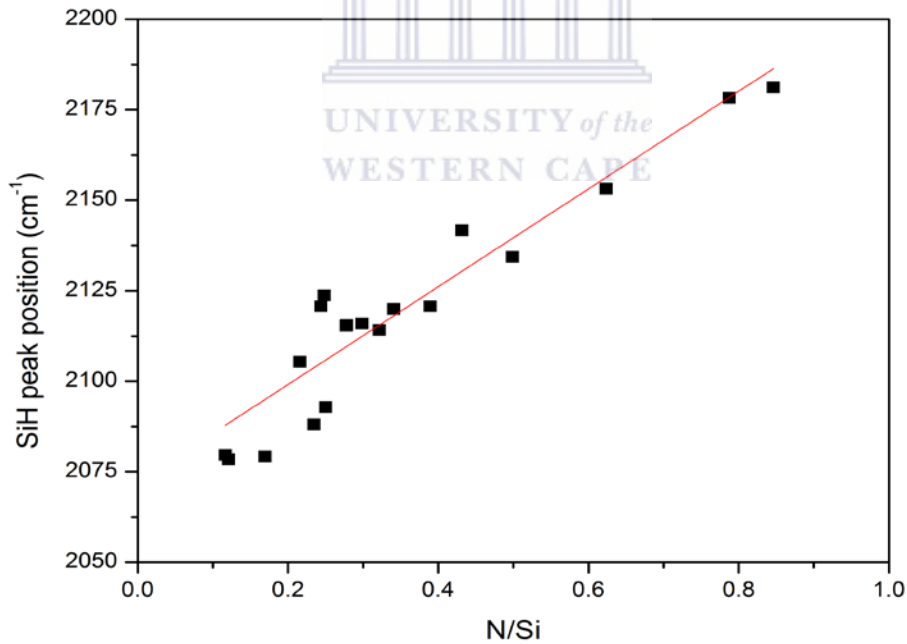


**Figure 3.24:** Graph illustrating the effect of N incorporation on the Si-H stretching peak position

The increase in wavenumber corresponds well with bonding units observed by Buserret *et al* [3.57] illustrated in table 2, where bonding unit evolution with wavenumber and increased N incorporation can be viewed. The table shows explicitly the increased N presence at high wavenumbers.

**Table 3.2:** Table illustrating bonding units, showing increased N presence [3.57]

Wavenumber (cm <sup>-1</sup> )	Attribution
2005	H-Si-Si <sub>3</sub>
2065	H <sub>2</sub> -Si-Si <sub>2</sub>
2100	H-Si-NSi <sub>2</sub>
2140	H-Si-N <sub>2</sub> Si, H <sub>2</sub> -Si-NSi
2175	H <sub>2</sub> -Si-N <sub>2</sub>
2220	H-Si-N <sub>3</sub>

The addition of the N-H and Si-H stretching integrated absorption was used as an indicator for showing the effect of N/Si ratio on the total bonded H. For the purpose of this study, only trend analysis will be performed using the integrated absorption. The effect of N incorporation can be observed in figure 3.25 where again there is no simple relation between the H content and N incorporation as observed from ERDA analysis. The trend is clearly the same as in figure 3.21, which is confirmation of the 3 phase behaviour of H incorporation into the a-SiN:H thin films. In previous work, a monotonic relationship has been observed between nitrogen content and H content [3.20, 3.58], which is contrary to that observed in this study.

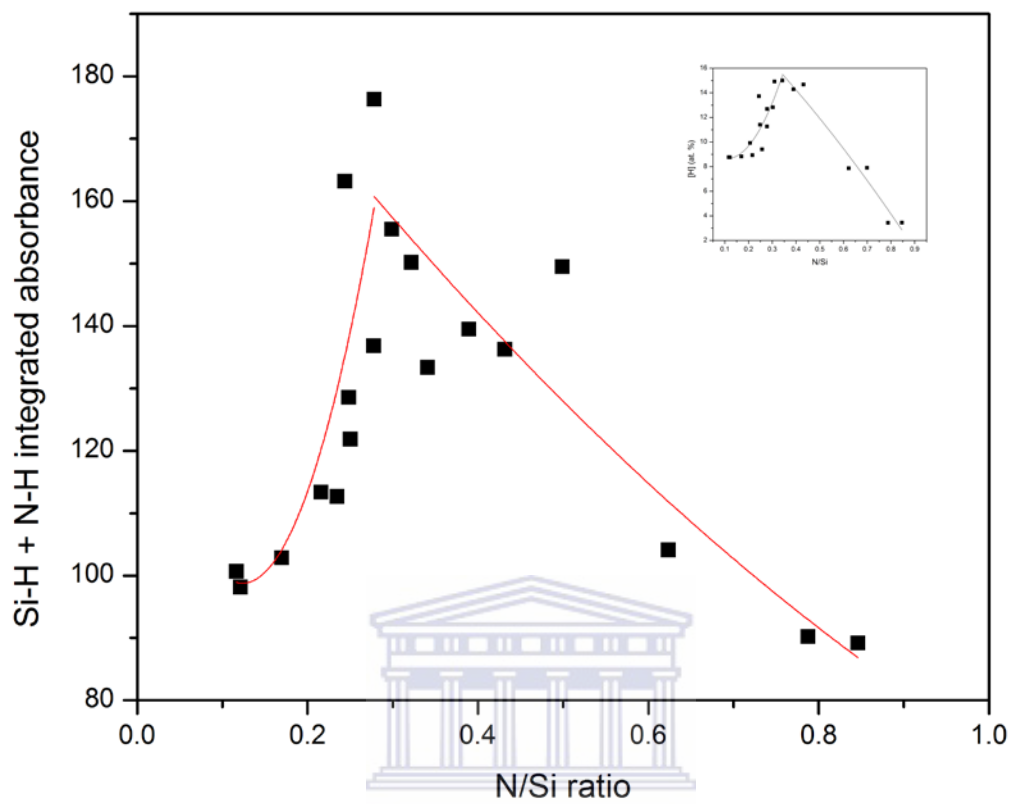


**Figure 3.25:** Total bonded SiH and NH stretching integrated absorption as a function of N/Si ratio.

### 3.5 STRUCTURAL PROPERTIES

In order to confirm the amorphous nature of the a-SiN:H, XRD was performed and conclusively indicates the deposited films are amorphous. Figure 3.26 shows a representative spectrum of the a-SiN:H thin films produced and it can be seen that there is no crystallinity present in the prepared films. The broad peaks observed around  $\sim 40^\circ$  and  $\sim 25^\circ$  in figure 3.26 are as a result of the amorphous corning 7059 substrate.

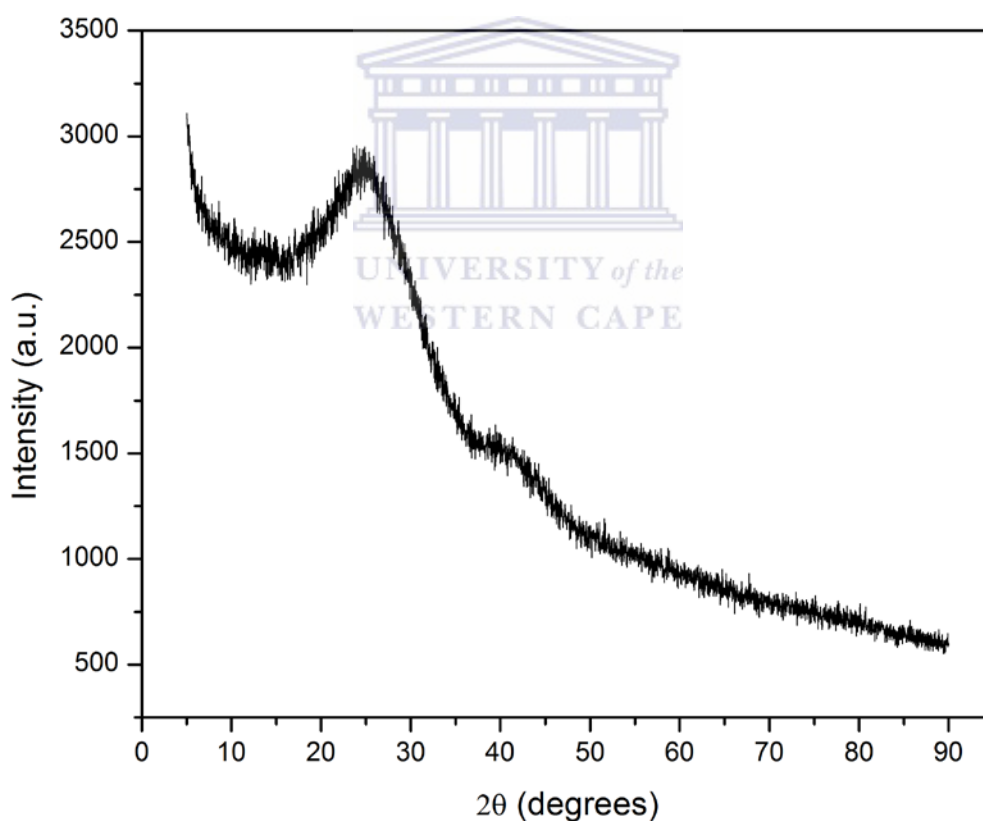


*Figure 3.26:* XRD spectrum of representative samples indicating the absence of crystallinity

### 3.6 OPTICAL PROPERTIES

The incorporation of a-SiN:H thin films in photovoltaic devices warrants the investigation into the optical properties of the material. The dual functionality of the a-SiN:H layer as passivating and antireflective coating gives it an added advantage over conventional antireflective coatings. In order to better understand a-SiN:H optically, the effect of structural and compositional changes on the optical properties must be understood. The Tauc band gap, static refractive index and refractive index dispersion and absorption coefficient dispersion as a function of N content will be investigated.

The dispersion plots shown in figure 3.27 serve as a representation of the effect of N content. The absorption coefficient as a function of photon energy is illustrated in figure 3.27a, where it can be seen that there is a dramatic decrease in absorption in the visible region as the N content increases. The decreased absorption is testament to an increased band gap resulting from the replacement of Si-Si bonds with thermodynamically more stable Si-N bonds. The result shown in figure 3.27a was also observed by Mei *et al* and showed to be consistent even after annealing [3.59].

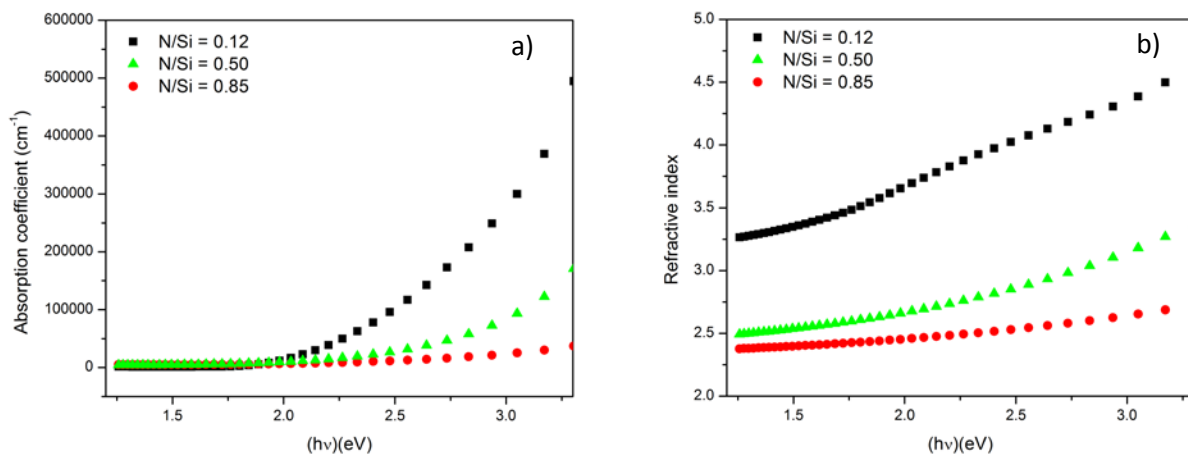


**Figure 3.27:** Effect N incorporation on the a) Absorption coefficient and b) Refractive index.

Figure 3.27b illustrates the refractive index with varying energy in the visible region for varying N content, which shows the refractive index to decrease as N content increases. The relationship between refractive index and band gap can be described by the following equation derived by Gupta *et al* [3.60] and Ravindra *et al* [3.61]:

$$\eta = 4.084 + \beta E_g \quad (3.14)$$

Where  $\eta$  is the refractive index,  $\beta$  is a constant,  $\beta = -0.62 \text{ eV}^{-1}$  and  $E_g$  is the band gap. This equation is only valid for the region  $1.1 \leq \eta \leq 4.1$ . The relationship from equation 3.14 clearly shows this inverse linear trend to be true for the a-SiN:H thin films prepared in this study, shown in figure 3.28 (a) and (b).

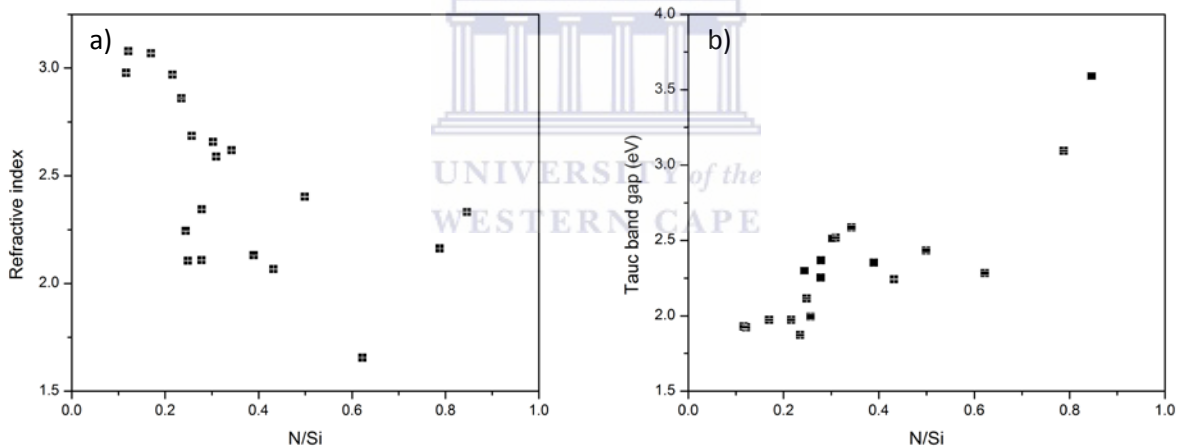


**Figure 3.28:** Effect of the N incorporation on the a) static refractive index and b) Tauc band gap.

The Tauc band gap is instrumental in the applicability of the a-SiN:H thin films as antireflective coating in photovoltaic applications. The band gap illustrated in figure 3.28 (b) shows a clear increasing trend as N content intensifies. This figure shows that there is a strong dependence of the band gap on the N content within the a-SiN:H film. This increased band gap can be attributed to the increased presence of stable SiN bonds in the matrix as these bonds have a high binding

energy the electron excitation energy also increases, which in turn results in a band gap increase [3.58]. This band gap increase was also observed by Hasegawa *et al* [3.62].

The refractive index provides invaluable information pertaining to the density of the deposited a-SiN:H thin films. Figure 3.29 shows the refractive index as a function of total H content from ERDA, where it can be seen that the refractive index is inversely related to the H content. Since density is directly proportional to refractive index [3.63] and inversely proportional to H content [3.47 – 3.48] it is expected that the refractive index and H content have an inverse relation. Thus, figure 3.29 provides confirmation that the density and H content are inversely proportional.

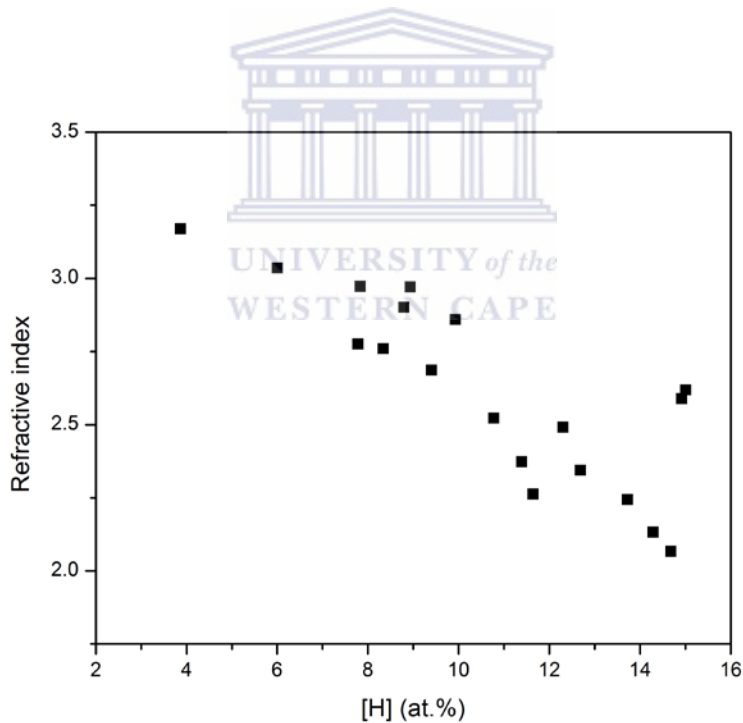


**Figure 3.29:** Static refractive index as a function of H content.

### **3.7 CONCLUSION**

Silicon rich a-SiN:H thin films were deposited by HWCVD in order to study the effect of pressure, NH<sub>3</sub>, H<sub>2</sub> and total flow rate on the film structural, optical and compositional properties. The depositions were performed at generally low processing parameters in the light of recent emphasis on financial and environmental sustainability.

The thicknesses obtained indicated that satisfactory deposition rates were attainable, despite the low processing parameters. A direct linear relation was observed between film thickness and roughness. The films were seen to be dominated by two growing regimes at the substrate surface namely; surface diffusion and shadowing.

The ToF-HIERD depth profiles indicated that the films were dense, uniform and resistant to oxygen permeation into the bulk. The N/Si ratio determined by ToF-HIERD was compared to that measured by EDS and this indicated that EDS can be used as a cheaper, more accessible alternate to ToF-HIERD for thick a-SiN:H thin films.

The total H-content determined from ERDA showed a complex, 3 regime relationship between N/Si and H content. The total bonded H, determined by FTIR confirms this three phase behaviour. A direct proportionality was observed for Si-H stretching peak position vs. N/Si, which can be used for N/Si ratio determination.

A direct proportionality was observed for the Tauc band gap vs. N/Si ratio and an inverse relationship was observed for the refractive index vs. N/Si plot. The refractive index had a minimum around  $\sim 1.5$  and the Tauc band gap peaked at around 3.6 eV. The absorption coefficient dispersion plot indicated that the films had depressed absorption in the visible region as the N content increased, which is desirable for applications as antireflective coatings.



### 3.8 REFERENCES

- [3.1] K. Coates, S. Morrison, S. Naraganan and A. Madan, *Proceedings of the 16<sup>th</sup> European Photovoltaic solar energy conference*, Glasgo, p 1297 (2000)
- [3.2] J. K. Holt, D. G. Goodwin, M. Gabor, F. Jiang, M. Stavola and H. Atwater, *Thin Solid Films*, **430**, p 37 (2003)
- [3.3] B. P. Swain, B. S. Swain and N. M. Hwang, *Applied Surface Science*, **255**, p 2557 (2008)
- [3.4] A. Ledermann, U. Weber, C. Mukherjee and B. Schroeder, *Thin Solid Films*, **395**, p 61 (2001)
- [3.5] F. Liu, S. Ward, L. Gedvilas, B. Keyes, B., To, and Q. Wang, *J. App. Phys.*, **96**, p 2973 (2004)
- [3.6] R.E.I. Schropp, C. H. M. van der Werf, V. Verlaan and J. K. Rath, H. Li, *Thin Solid Films*, **517**, p 3039 (2009)
- [3.7] V. Verlaan, A. D. Verkerk, W. M. Arnoldbik, C. H. M. van der Werf, R. Bakker, Z. S. Houweling, I. G. Romijn , D. M. Borsa, A.W. Weeber, S.L. Luxembourg, M. Zeman, H. F. W. Dekkers and R. E. I. Schropp, *Thin Solid Films*, **517**, p 3499 (2009)
- [3.8] J. E. Bourée, J. Guillet, C. Grattapain, J. Chaumont, *Thin Solid Films*, **430** p 110 (2003)
- [3.9] M. H. Brodsky, M. Cardona and J. J. Cuomo *Phys. Rev. B*, **30**, p 3556 (1977)
- [3.10] Maley N *Phys. Rev.B*, **46**, p 2078 (1992)

- [3.11] S. K. O’Leary, P. K. Johnson and P. K. Lim *J., App. Phys.*, **82**, p 3334 (1997)
- [3.12] K. Tonokura, K. Inoue, and M. Koshi, *J. Non-Cryst., Solids*, **299–302**, p 25 (2002)
- [3.13] Y Nozaki, K. Kongo, T. Miyazaki, K Kitazoe, K. Horii, H. Umemoto, A. Masuda, and H. Matsumura, *J. App. Phys.*, **88**, p 5437 (2000)
- [3.14] S. Tange, K. Inoue, K. Tonokura, M. Koshi *Thin Solid Films*, **395**, p 42 (2001)
- [3.15] H. Umemoto, K. Ohara, D. Morita, T. Morimoto, M. Yamawaki, A. Masuda and H. Matsumura *Jpn. J. Appl. Phys.* 42 (2003) pp. 5315-5321
- [3.16] B. Eustergerling, M. Hèden and Y. Shi, *American society of mass spectrometry*, **18**, p 1950 (2007)
- [3.17] H. Umemoto, T. Morimoto, M. Yamawaki, Y. Masuda, A. Masuda, and H. Matsumura *Jpn. J. Appl. Phys.*, **430**, p 24 (2003)
- [3.18] Y.J. Shi, B.D. Eustergerling, and X.M. Li, *Thin Solid Films*, **516**, p 506 (2008)
- [3.19] B. Eustergerling and Y. Shi, *ARKIVOC*, **v**, p 75 (2009)
- [3.20] V. Verlaan, R. Bakker, C.H.M. van der Werf, Z.S. Houweling, Y. Mai, J.K. Rath, and R.E.I. Schropp, *Surface coatings technology*, **201**, p 9285 (2007)
- [3.21] S. V. Deshpande, J. L. Dupuie and E. Gulari, *Appl. Phys. Lett.*, **61**, p 1420 (1992)
- [3.22] A. H. Mahan, A. C. Dillon, L. M. Gedvilas, D. L. Williamson, and J. D. Perkins *J. App. Phys.*, **94**, p 2360 (2003)
- [3.23] S.G. Ansari a, H. Umemoto, T. Morimoto, K. Yoneyama, A Izumi, A. Masuda and H Matsumura, *Thin solid films*, **501**, p 31 (2006)

- [3.24] F. Liu, S. Ward, L. Gedvilas, B. Keyes, B., To, and Q. Wang, *J. App. Phys.*, **96**, p 2973 (2004)
- [3.25] B. Stannowski, J. K. Rath and R. E. I. Schropp *J. App. Phys.*, **93**, p 2618 (2003)
- [3.26] T. Osono, A. Heya, T. Niki, M. Takano, T. Minamikawa, S. Muroi, A. Masuda, H Umemoto, and H. Matsumura *Thin solid films*, **501**, p 55 (2006)
- [3.27] L. Yu, J. Xu, S. Dong, and I. Kojima, *Thin solid films*, **516**, p 1781 (2008)
- [3.28] V. Verlaan *PhD Thesis, Utrecht university*, pp. 44 – 45 (2008)
- [3.29] I. G. Romijn, W. J. Soppe, H. C. Rieffe, W. C. Sinke, and A. W. Weeber, *15<sup>th</sup> Workshop on crystalline Silicon Solar cells & Modules: Materials and processes Vail Colorado, USA* (2005)
- [3.30] J.A. Thornton, *J. Vac. Sci. Technol.*, **A 4**, p 3059 (1986)
- [3.31] R.P.U. Karunasiri, R. Bruinsma, and J. Rudnick, *Phys. Rev. Lett.*, **62**, p 788 (1989)
- [3.32] G.S. Bales, R. Bruinsma, E.A. Eklund, R.P.U. Karunasiri, J. Rudnick, and A. Zangwill, *Science*, **249**, p 264 (1990)
- [3.33] W. Xu, B. Li, T. Fujimoto, I. Kojima, *Surface coatings and technology*, **135**, p 274 (2001)
- [3.34] Y.-S. Lai, S. W. Yung and J.-L. Wang, *Thin Solid Films*, **519**, p 2235 (2011)
- [3.35] J. L. Dupuie, E. Gulari and F. Terry, *J. Electrochem. Soc.*, **139**, p 1159 (1992)
- [3.36] H. Sato, A. Izumi, A. Masuda and H. Matsumura, *Thin solid films*, **395**, p 280 (2001)
- [3.37] C. M. M. Denissen, H. E. Smulders, F. H. P. M. Habraken and W. F. van de Weg, *Appl., Surf., Sci.* **39**, 25 (1989)
- [3.38] C. Fakih, G. B. Fakih, A. Kaafarani, M. Zoeter, R. S. Bes, and R. Berjoan, *Comp. Mat. Sci.*, **33**, p 395 (2005)

- [3.39] S. B. Patil, A. Kumbhar, P. Waghmare, V. R. Rao and R. O. Dusane, *Thin solid films*, **395**, p 270 (2001)
- [3.40] A. G. Aberle, *Sol. Energy Mater Sol. Cells*, **65**, p 239 (2001)
- [3.41] W. Soppe, H. C. Rieffe, and A. W. Weeber, *Prog. Photovolt.: Res. Appl.* **13**, p 551 (2005)
- [3.42] I.G. Romijn, W.J. Soppe, H.C. Rieffe, A.R. Burgers, and A.W. Weeber, *Proceedings of the 20th European Photovoltaic Solar Energy Conference and Exhibition, Barcelona, Spain*, p 1352 6–10 June, 2005
- [3.43] H.F.W. Dekkers, L. Carnel, and G. Beaucarne, *Appl. Phys. Lett.*, **89**, p 013508 (2006)
- [3.44] V. Verlaan, Z.S. Houweling, C. H. M. van der Werf, I.G. Romijn, A.W. Weeber, H.D. Goldbach, and R. E. I. Schropp, *Thin solid films*, **516**, p 533 (2008)
- [3.45] P. Hovington, D. Drouin and R. Gauvin, *Scanning*, **19**, p 1 (1996)
- [3.46] W. A. Lanford and M. J. Rand, *J. Appl. Phys.* **49**, p 2473 (1978)
- [3.47] R.E.I. Schropp, S. Nishizaki , Z.S. Houweling , V. Verlaan , C.H.M. van der Werf , H. Matsumura, *Solid-State Electronics*, **52**, p 427 (2008)
- [3.48] V. Verlaan, C.H.M. van der Werf, Z.S. Houweling, Y. Mai, R. Bakker, I.G. Romijn, A.W. Weeber, H.D. Goldbach, and R.E.I. Schropp, *Presented 22th EU PVSEC. Milaan, Italy*, (2007)
- [3.49] V. Verlaan, C.H.M. van dar Werf, W. M. Arnoldbik, H. D. Goldbach and R. E. I. Schropp, *Phys. Rev. B*, **73**, p195333 (2006)

- [3.50] B. Stannowski, C.H.M. van der Werf and R. E. I. Schropp, *Proc. Of the 3rd international conference on coatings on glass*, p 387 (2000)
- [3.51] G. Lucovski, J. Wang, S. S. Choa, J. E. Tyler, and W. Czubytyj, *Phys. Rev. B*, 28, p 3234 (1983)
- [3.52] S. Hasegawa, H. Anbutsu, and Y. Kurata, *Philos. Mag. B* 59, p 365 (1989)
- [3.53] K-C. Lin and S-C. Lee, *J. Appl. Phys.*, 72, p 5474 (1992)
- [3.54] S. Hasegawa, L. He, Y. Amano, and T. Inokuma, *Phys. Rev. B*, 48, p 5315 (1993)
- [3.55] A. Cuevas, F. Chen, J. Tan, H. Mäckel, S. Winderbaum and K. Roth, *Photovoltaic Energy IEEE 4th world conference*, p 1148 (2006)
- [3.56] H. Mäckel and R. Lüdermann, *J. Appl. Phys.*, 92, p 2603 (2002)
- [3.57] E. Bustarret, M. Bensouda, M. C. Habrard, J. Bruyere, S. Poulin, and S. Gujrathi *Phys. Rev. B* 38, 8171 (1988)
- [3.58] F. Giorgis, C. F. Pirri and E. Tresso, *Thin Solid Films* 307, 298 (1997)
- [3.59] J. J. Mei, H. Chen, W. Z. Shen and H. F. W. Dekkers, *Journal of Applied Physics*, **100**, p 073516 (2006)
- [3.60] V. P. Gupta and N. M. Ravindra, *Phys. Stat. Sol (b)*, **100**, p 715 (1980)
- [3.61] N. M. Ravindra and V. K. Srivastva, *Infrared Phys.* **19**, p 603 (1979)

[3.62] S. Hasegawa, M. Matuura and Y. Kurata, *Appl. Phys. Let.*, **49**, p 1272 (1986)

[3.63] N. Kitamura, K. Fukumi, J. Nishii and N. Ohno *J. Appl. Phys.*, **101**, 123533 (2007)



## **SUMMARY**

Hydrogenated amorphous silicon nitride thin films were deposited by hot wire chemical vapour deposition (HWCVD). The effect of various parameters such as the  $\text{NH}_3$  flow rate,  $\text{H}_2$  flow rate, pressure and total flow rate was investigated. The purpose of this study was to optimize the MV System HWCVD for the deposition of a-SiN:H thin films at The University of the Western Cape, under low processing parameters.

The results were discussed in chapter 3. The thickness of the films were determined by optical reflection measurements and showed to have an inverse relation to addition of  $\text{H}_2$  and  $\text{NH}_3$  gas to the chamber and a direct relation to an increase in total flow rate and pressure. The maximum deposition rate attained was in the region of  $\sim 31$  nm/min. This deposition rate is considerably high since the deposition parameters were generally kept low.

The effect of the deposition parameters on the surface morphology was also investigated by AFM and the results showed that the roughness had a strong dependence on the thickness after  $\sim 300$  nm. This illustrated the two growing regimes at the substrate namely surface diffusion and columnar growth, the latter comes in to play as films reach thicknesses above 300 nm, hence the films become rougher.

The N/Si ratio was investigated by HIERD and EDS and the results attained were compared and show to correspond well. The results of HIERD and EDS did not correspond well for films that had thickness values below 300 nm which was attributed to the inability of the EDS technique to distinguish between the substrate and the a-SiN:H thin film. The HIERD depth profiles showed the films to generally have a uniform distribution of Si and N, with little to no oxidation in the

## *SUMMARY*

---

bulk despite the HIERD measurements taking place 3-5 months post deposition. This indicated that the films were dense and not prone to oxidation.

The result attained by HIERD was supported by the H content attained by ERDA as the films had low H content; and elevated H content is associated with density degradation in a-SiN:H thin films. The H content of the deposited films had a minimum of 3 at.% at N/Si ratio of 0.85. The relationship between N/Si and H content showed interesting results which led to the insight that the N/Si ratio and H content plot has three regimes namely; silicon rich, approaching stoichiometry and nitrogen rich. A general relationship between N and H content cannot be obtained across all N content as each regime must be considered individually.

The total bonded H content was determined by FTIR and a result similar to that shown for N/Si vs [H] at.% was attained. This serves as confirmation of the three regime relationship between the N content and H incorporation in a-SiN:H thin films. A linear relationship was illustrated for the relationship between N content and Si-H stretching peak position, which enables determining the N/Si ratio from the peak position using equation 3.13.

The optical properties of the films were determined by reflectance measurements and an inverse relation was observed between the band gap and refractive index with respect to the N content. The band gap reached a maximum at around 3.6 eV and the refractive index had a minimum around 1.6. Since refractive index is directly related to the density it was expected that refractive index should have an inverse relation to H content, which was confirmed by a plot of H content vs. static refractive index.

## *SUMMARY*

---

The a-SiN:H thin films deposited showed to be of relatively good quality since the films did not oxidize deep into the bulk and the band gap attained was considerably high. It can therefore be concluded that the HWCVD system, at The University of the Western Cape may be used for attaining device quality films at low processing parameters.

In future work this low temperature deposition parameters may be further decreased and possibly applied to organic photovoltaic devices as these devices tend to be unstable at elevated temperatures.

